CORA Cork Open Research Archive
Cartlann Taighde Oscailte Chorcaí

Title	New photonic imaging systems for biomedical applications
Authors	Sen, Rajannya
Publication date	2023-06-07
Original Citation	Sen, R. 2023. New photonic imaging systems for biomedical applications. PhD Thesis, University College Cork.
Type of publication	Doctoral thesis
Rights	© 2023, Rajannya Sen. - https://creativecommons.org/licenses/by-nc-nd/4.0/
Download date	2026-11-15 13:50:14
Item downloaded from	https://hdl.handle.net/10468/14956

UCC
University College Cork, Ireland
Coláiste na hOllscoile Corcaigh

Ollscoil na hÉireann, Corcaigh

National University of Ireland, Cork



New Photonic Imaging Systems for Biomedical Applications

Thesis presented by

Rajannya Sen

for the degree of

Doctor of Philosophy

University College Cork

School of Biochemistry and Cell Biology

Head of School: Prof. Justin McCarthy

Supervisor: Prof. Dmitri B. Papkovsky,

Co-Supervisor: Dr. Stefan Andersson-Engels

2023

Table of Contents

Acknowledgements 6

List of abbreviations 7

Abstract 9

1. Chapter 1: Literature Review 11

1.1. O_2 homeostasis and tissue O_2 levels 11

1.2. Available O_2 Detection Methods 14

1.3. Quenched-Luminescence Detection of O_2 17

1.4. Phosphorescent O_2 sensing materials 18

1.4.1. Solid state sensors 21

1.4.2. Soluble O_2 probes 22

1.4.3. Micro and nanoparticle-based probes 22

1.4.4. Cell permeable O_2 probes 23

Cellular imaging of myeloma and human blood platelets. 24

Intracellular O_2 Sensing. 24

1.5. O_2 Detection Modalities 25

1.5.1. Intensity and Ratiometric Intensity based sensing 25

1.5.2. Lifetime based sensing 28

1.5.3. O_2 imaging 30

1.6. New development in FLIM hardware 37

1.7. Applications of O_2 imaging and PLIM 41

1.8. Conclusion 46

2. Chapter 2: Materials and Methods 49

2.1. Materials 49

2.2. Methods 49

2.2.1. Preparation of Sensors 49

2.2.2. Preparation, staining and treatment of ex vivo animal tissue 51

2.3. Imaging on Tpx3Cam 53

2.3.1. Design of µs PLIM macro imager 53

2.3.2. Image acquisition and data analysis 55

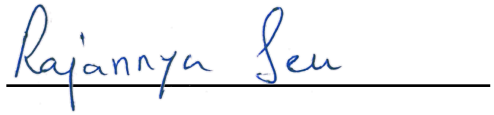
2.3.3. Statistics 56
2.4. Imaging on confocal PLIM microscope 57
2.5. Calibration of sensor materials 57
3. Chapter 3: Design and Characterisation of the new Tpx3Cam based PLIM/FLIM macro-imager 59
3.1. Design and Characterization of imager 60
3.1.1. Single photon events 61
3.1.2. Spatial resolution and centroiding methods 62
3.1.3. Instrument response 63
2.2. Conclusion 66
4. Chapter 4: Characterization of the chemical samples (oxygen sensors and probes) with the imager 67
4.1. Imaging of the different sensor materials 68
4.2. Comparison of the different sensor materials and lifetime detection platforms 75
4.3. Sensitivity of the PLIM macro-imager and stability of lifetime measurements. 79
4.4. Conclusions 80
5. Chapter 5: Mapping O_2 in biological samples with Tpx3Cam Imager 82
5.1. Imaging of ex-vivo tissue samples 83
5.1.1. Imaging of respiring cells 83
5.1.2. Imaging of mouse brain and lung tissue surface-stained with NanO2-IR probe 86
5.1.3. Deep tissue staining and imaging using NanO2-IR probe 91
5.2. In-vivo imaging of live and sacrificed animals 96
5.2.1. Optimisation of NanO2-IR probe delivery and tumour growth 97
5.2.2. In vivo and post-mortem analysis of O_2 levels in tumours 99
5.2.3. Analysis of NanO2-IR distribution in tumour tissue 101
5.3. Conclusions 103
Chapter 6: Final Discussion 105
Appendix 109
List of tables 112

List of figures 113
Thesis Outcomes 120
Peer reviewed papers: 120
Conference proceedings: 120
Bibliography 121

Declaration

This is to certify that the work I am submitting is my own and has not been submitted for another degree, either at University College Cork or elsewhere. All external references and sources are acknowledged and identified within the contents. I have read and understood the regulations of University College Cork concerning plagiarism.

Signed: Rajannya Sen



Date: 07/06/2023

Acknowledgements

I would like to convey my deepest gratitude to my supervisor, Prof. Dmitri Papkovsky, for his guidance and patience throughout my PhD. Thank you for sharing your invaluable knowledge and thoughts and allowing me to experience opportunities to meet some great people. I would also like to thank my co-supervisor, Dr. Stefan Andersson-Engels, for his constant support.

I want to thank Dr. Andrei Nomerotski, Dr. Liisa Hirvonen, and Dr. Alexander Zhdanov for providing the training and constant mentorship. To my colleagues, Sophia, Elisa, Chiara, Rafael, Liang, and Emer, thank you for the great experience in the lab.

I am extremely grateful to my family in Ireland. Thank you, Arindam, Debapriya, Ranu, Swastika, Seuli, Sambuddha, Somnath, Samir, and Archishman, for your constant love and support. I am thankful to you all for being an essential part of this journey.

Finally, I would like to thank my family. Thank you, Ma and Baba, for your love and blessings. Without your support, I would not have reached this far. Lastly, to my husband Tanmay, thank you for always being there for me, even during the toughest times.

List of abbreviations

^{19}F	……	fluorine-19
2D	……	Two dimensional
2P	……	Two-Photon
3D	……	Three dimensional
AntA	……	Antimycin A
ATP	……	Adenosine triphosphate
CCD	……	Charged Coupled Devices
CMOS	……	Complementary Metal Oxide Semiconductor
DMEM	……	Dulbecco's modified Eagle Medium
EPO	……	Erythropoietin
EPR	……	Electron Paramagnetic Resonance
ETC	……	Electron Transport Chain
FBS	……	Foetal Bovine Serum
FLIM	……	Fluorescence Lifetime IMaging
HIF-1	……	Hypoxia-Inducible Factor
HRE	……	Hypoxia Response Element
IRF	……	Instrument Response Function
LED	……	Light Emitting Diode
LiDAR	……	Light Detection and Ranging
MCP	……	Microchannel Plate
MRI	……	Magnetic Resonance Imaging
NIR	……	Near Infrared
NIRS	……	Near Infrared Spectroscopy
NP	……	Nano-particle
O_2	……	Oxygen
OEPK	……	OEP-Ketone
PCC	……	Photon Counting Chip
PET	……	Positron Emission Tomography
PFA	……	Paraformaldehyde
PHD	……	Prolyl-4-hydroxylase
PLIM	……	Phosphorescence Lifetime Imaging

PLT	……	Phosphorescence Lifetime
PMMA	……	Poly(methyl methacrylate)
PMT	……	Photomultiplier Tube
PS	……	Polystyrene
PtBP	……	Pt(II)-benzoporphyrin
PtOEP	……	Platinum Octaethylporphyrin
PtOEPK	……	Pt(II) Octaethylporphine-Ketone
PtPFPP	……	Pt(II)-tetrakis(pentafluorophenyl)porphine
PVDC	……	Poly(vinylidene chloride)
pVHL	……	Von Hippel–Lindau protein
PVS	……	Polyvinyl chloride
RLD	……	Rapid Lifetime Determination
ROI	……	Region Of Interest
ROS	……	Reactive Oxygen Species
SNR	……	Signal-to-noise ratio
SPAD	……	Single Photon Avalanche Photodiode
SPIDR	……	Speedy PIxel Detector Readout
TCSPC	……	Time-Correlated Single Photon Counting
TDC	……	Time-Digital Converter
TOA	……	Time Over Arrival
TOT	……	Time Over Threshold
TR-F	……	Time-Resolved Fluorescence
UV	……	Ultraviolet

Abstract

Oxygen (O_2) is one of the essential environmental parameters for living organisms, as it plays a vital role in their metabolism. Therefore, monitoring the distribution of O_2 and its dynamics is essential for physiological studies. Assessment of tissue oxygenation by means of phosphorescent probes and optical microscopy has been increasingly used in biological and medical research. O_2 imaging by PLIM is gaining popularity as it can provide an accurate, quantitative, and calibration-free mapping of O_2 concentration in complex biological samples and is unaffected by external factors such as probe concentration, autofluorescence, photobleaching, optical alignment, excitation intensity, and scattering.

Current PLIM platforms have limitations in image acquisition speed, sensitivity, penetration depth, accuracy, and general usability. TCSPC with raster scanning technique is frequently used in PLIM, but it is slow as it requires long pixel dwell times to measure long-lived phosphorescence. Other commonly used techniques include gated CCD and CMOS cameras, which lack single photon sensitivity and have a low frame rate. Moreover, the majority of the current PLIM systems use a microscopic format, while macroscopic systems are rarely available.

We demonstrate a new macro-imager that overcomes many of these limitations. The imager is based on the new time-stamping Tpx3Cam optical camera, which combines a novel silicon optical sensor and a Timepix3 readout chip that has the capability to record the TOA and TOT at each pixel simultaneously. For TCSPC-PLIM applications, the Tpx3Cam imager was built by integrating the camera with an image intensifier that provided single photon sensitivity, an emission filter, and a macro lens using a Cricket adapter. Sample excitation was performed with an LED controlled by a pulse generator and synchronised with the camera. A custom-designed software was used to acquire the Tpx3Cam raw data in a binary format, and a C-language code was used to post-process the data. The resulting data matrix was then fitted with a bi-exponential function to determine the lifetime values.

Planar phosphorescent O_2 sensors and a resolution plate mask were used to characterize the imager. The performance and resolution of the imager were optimized with different image processing techniques, and the spatial and temporal resolution achieved were adequate for wide-field PLIM applications.

Various commercial and non-commercial O_2-sensitive phosphorescent materials were evaluated with the new imager. The lifetime signals were recorded for 20 s and the PLIM images generated by the imager showed good uniformity and lifetime contrast between the different materials with varying temperature and oxygenation conditions. The phosphorescence lifetime values were also consistent with those measured by alternative methods.

Next, we demonstrated the application of the imager for mapping O_2 concentration in live tissue samples stained with a PtBP-based NanO2-IR probe. The tissues were stained passively or by microinjections, and PLIM was performed under resting conditions and upon inhibition of respiration. The imager allowed accurate phosphorescence lifetime measurement of the probe and generated detailed O_2 concentration maps of the tissue surface and even at depths of up to 0.5 mm inside the tissue.

Lastly, we demonstrated the Tpx3Cam imager in model *in vivo* applications to map O_2 concentration and tissue hypoxia in grafted tumours of laboratory animals. The probe delivery conditions in the animals were optimized to prevent adverse effects and enable long-term detection of the probe in the grafts. The live animals were injected with CT26 cells stained with the NanO2-IR probe to develop tumours with characteristic phosphorescence. The animals were monitored, and tumours were allowed to grow for 3, 7, 10 and 17 days. O_2 imaging of live and euthanized animals at different time points produced phosphorescence lifetime values that reflected the hypoxic state of the tissue. Confocal PLIM microscopy was also performed on the excised tissues to demonstrate the distribution of the probe in the tumour.

These results demonstrate that the new Tpx3Cam imager shows promising performance in PLIM mode with high spatial resolution. It can image objects up to several centimetres in size with flexible optical alignment (e.g., vertical or horizontal configuration). It can produce accurate lifetime values at a superior speed and sensitivity that can be converted to O_2 concentration maps. The application of the imager ranges from the characterization of solid-state O_2-sensors to O_2 imaging of sizable biological samples, including respiring cells, live post-mortem animal tissues and organs and *in vivo* imaging of tissue hypoxia in animal models. Overall, the imager can be used for quantitative wide-field PLIM in physiological *in vivo* studies in a minimally invasive manner.

1. Chapter 1: Literature Review

1.1. O_2 homeostasis and tissue O_2 levels

Molecular oxygen (O_2) plays important roles in living organisms. It helps to generate energy in the form of adenosine triphosphate (ATP). Otto Warburg received the Nobel Prize in Physiology or Medicine in 1931 for demonstrating that oxidation conversion of food into ATP is an enzymatic procedure (Warburg, 1931). O_2 acts as the terminal acceptor of the Electron Transport Chain (ETC) and performs many vital physiological functions: it acts as a substrate for many enzymes, a signalling molecule, and a source of Reactive Oxygen Species (ROS) (Brand & Nicholls, 2011; Carreau et al., 2011; Semenza, 2007, 2012). However, O_2 levels in the body are tissue-specific and tightly regulated by hemoglobins, myoglobins, red blood cells, and the vasculature (Semenza, 2010; Wilson, 2008). Deviations from normal conditions may lead to pathological states and even death of the cell or whole organism. Physiological O_2 levels result from a gentle balance between O_2 supply and demand. Therefore, maintaining normal O_2 levels and homeostasis in tissues are extremely important. The discovery of mechanisms of O_2 sensing and adaptive responses to hypoxia in mammalian cells has opened up a new field of research (Liao & Zhang, 2020; Prabhakar, 2020; Ratcliffe, 2013; Semenza, 2011).

The usual O_2 concentrations to which cells in the human body are exposed range from 20.86% in the atmosphere and upper airways to 1% at the corticomedullary junction of the kidney. The standard O_2 concentration used by biologists in tissue culture cells is 18.6% O_2 (95% air and 5% CO_2), and this condition is referred to as ***atmospheric*** normoxia. Table 1.1 shows the O_2 concentration at ***physiological*** normoxia in different human tissues. Hypoxia, on the other hand, is defined as a condition of O_2 deprivation in cells and tissues. Animal cells can sense the variation in O_2 and switch on adaptive response mechanisms to adjust to the low O_2 tensions for survival. Most types of cells possess and conserve these O_2-dependent mechanisms (J. W. Lee et al., 2004). One of these is erythropoietin (EPO), a kidney-derived glycoprotein purified in

1977 (Miyake et al., 1977) and cloned in 1985 (F. K. Lin et al., 1985), which led to the investigation of O_2-sensing technology. Despite the fact that EPO stimulates the bone marrow to make red blood cells, thereby increasing the capacity of the blood to carry O_2, and EPO levels increase when there is a shortage of O_2 in cells, the molecular mechanism by which the body recognized a lack of O_2 to control the EPO expression remained unknown. The first study of the regulation of the EPO gene under various O_2 conditions was conducted by Semenza et al. (Semenza et al., 1991). The discovery of Hypoxia Response Elements (HREs) in different cells by Semenza (G. L. Wang & Semenza, 1993), Ratcliffe (Maxwell et al., 1993), and colleagues in 1993 has expanded our understanding of this O_2-sensing system. Subsequently, (G. L. Wang et al., 1995) identified the main component and isolated the nuclear factor linked to the EPO gene and called it the hypoxia-inducible factor (HIF-1). HIF-1 is a heterodimer of the oxygen-labile subunit HIF-1α and the constitutively expressed subunit HIF-1β (G. L. Wang et al., 1995). The HIF-1 protein is influenced by O_2 levels, and it regulates the transcription of a large number of genes.

Table 1.1: O_2 concentration in various human tissues, expressed in mmHg and in percentage of O_2 in the microenvironment

Tissue type	**O_2 (%)**	**O_2 (mmHg)**	**References**
Brain	4.4±0.3	33.8±2.6	(Dings et al., 1998; Hoffman et al., 1996; Koršič et al., 2006; Meixensberger et al., 1993)
Lung	5.6	42.8	(Le et al., 2006)
Kidney	9.5±2.6	72±20	(Muller et al., 1998)
Liver	5.4±0.7	40.6±5.4	(Brooks et al., 2004; Leary et al., 2002)
Intestine	7.6±0.3	57.6±2.3	(Müller et al., 1995, 2002; Thermann et al., 1985)
Muscle	3.8±0.2	29.2±1.8	(Beerthuizen et al., 1989; Boekstegers et al., 1990; Richardson et al., 2006)

Physiological hypoxia activates the hypoxia signalling pathways governed by HIF (Figure 1.1). Under normoxic conditions, O_2-dependent prolyl-4-hydroxylases (PHDs) hydroxylate the HIF-α subunits. Von Hippel–Lindau protein (pVHL) binds to the hydroxylated HIF-α which leads to the degradation of HIF protein. Under physiological hypoxia, these activities are suppressed, and

the HIF-α subunits translocate into the nucleus to bind with HIF-1β. The HIF-α: HIF-1β transcription factor complex then binds to the HREs of its target genes, resulting in their transcriptional upregulation. Other homologs of α-unit include HIF-2α and HIF-3α which have similar characteristics to HIF-1α in dimerization with HIF-1β and DNA binding. While HIF-1α is expressed ubiquitously, the other two are expressed in a cell line/tissue-restricted manner.

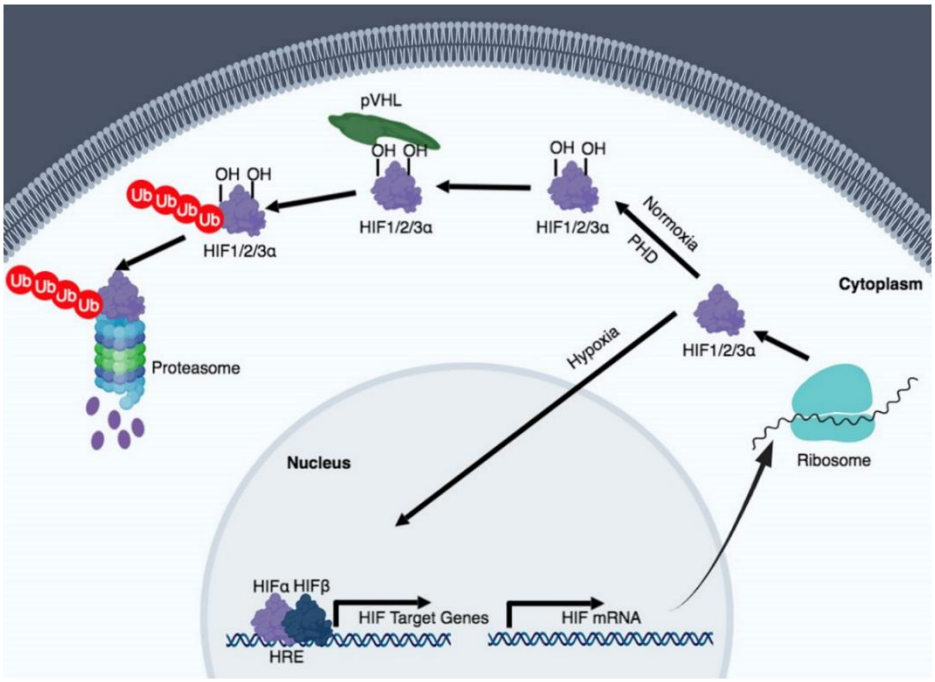


Figure 1.1: Hypoxia-inducible factor (HIF) regulation during physiological normoxia and hypoxia (J. W. Lee et al., 2019).

Since HIF signaling plays a crucial role in many human diseases, therapies have been developed that target the HIF pathway directly or indirectly. The approaches include targeting HIF mRNA expression, nuclear translocation, HIF-HRE interaction, dimerization of HIF-α and HIF-1β, etc. Apart from direct targeting of the oxygen/PHD/HIF/VHL cascade, oxygen independent pathways that activate HIF are also in use. Several inhibitors of HIF-1α were assessed for treatment of different disorders, but only a few have progressed towards clinical use (W. Chen et al., 2016; Cho et al., 2016; Jeong et al., 2014; Scheuermann et al., 2013; Weiss et al., 2013), with low selectivity, potency, and prominent side effects (Godet et al., 2022). Therefore, additional research is necessary to advance the clinical benefit. HIF/pan-PHD inhibition also has negative effects. Moreover, the diverse and overlapping signalling pathways make the HIF system very complex and difficult to design selective drugs for. Therefore, physiological

studies of cell/tissue hypoxia and related signalling events by O_2 sensing methods are very beneficial, as they can shed light on these processes and many questions which relate to them.

1.2.Available O_2 Detection Methods

Over the years, various techniques have been developed for studying O_2 levels in tissues and cells and their spatial distribution. In the 1930s, Karl Matthes first used red and infrared light transmission through the human ear to measure oxygenation (Sanklecha, 1993). Later in 1942, Glen Milliken developed an ear oximeter, which was used in pulmonary and physiology laboratories (Sanklecha, 1993). Other conventional techniques include: invasive polarographic electrodes, near infrared spectroscopy (NIRS), electron paramagnetic resonance spectroscopy (EPR), magnetic resonance imaging (MRI), positron emission tomography (PET), and other optical methods. Most of these methods either do not provide absolute O_2 concentrations or have low anatomical resolution. As a result, photoluminescence-based imaging has emerged as a useful technique for *in vivo* and intracellular O_2 measurements.

The polarographic Clark-type O_2 electrode, considered a gold standard for measuring O_2 in solutions and animal tissues (Stone et al., 1993), was described by Leland Clark (Clark Jr. et al., 1958). It uses a pair of electrodes (anode and cathode) in a buffered electrolyte solution and wrapped in an O_2-permeable insulating membrane. When an electric current of known magnitude is applied to the electrode, the silver anode gets oxidized and combines with the electrolytes to form silver chloride. The resulting electrons at the platinum cathode reduces oxygen, which interacts with water to produce hydroxide ions. The electron flow between the electrodes generates a current which is proportional to the partial pressure of oxygen dissolved in the sample. Most of the quantitative data on tissue O_2 levels were produced on the microelectrode-based Eppendorf O_2 histography system, which was also used to measure O_2 in tumours and in the brain (Brizel et al., 1996; O'Hara et al., 2004; Vaupel et al., 1991). But this invasive technique has limitations. It requires special expertise to correctly insert the electrode needle in tumour regions, but still, it disrupts the tissue. Since it usually performs point measurements, O_2 distribution throughout the tissue is not

well represented (Bartlett et al., 2008; Collingridge et al., 1997). Also, it has a low signal-to-noise ratio (SNR) at low O_2 concentrations and cannot perform repeated measurements.

NIRS is a technique that measures tissue oxygenation via the transmission and absorption of light. It was first described in 1977 (Jöbsis, 1977) to monitor the O_2 saturation state of hemoglobin, which reflects indirectly tissue oxygenation (Cheung et al., 2022; Hamaoka & McCully, 2019; Mizukoshi et al., 2022; Murkin & Arango, 2009). The technique uses the characteristic absorption wavelengths of hemoglobin and oxy-hemoglobin in the near-infrared region to make real-time measurements. The NIR light is produced by a light source, such as a LED, which passes through the tissue and interacts with multiple tissue components. Optical pigments like melanin, myoglobin, and hemoglobin partially absorbs the NIR light resulting in change of the spectrum. The difference in the spectrum between the transmitted and detected light determines the level of oxygenation in the pigments. But this technique can only record oxygenation levels in the vascular system and bound oxygen, rather than free oxygen and tissue O_2 levels.

The EPR phenomenon was discovered in 1944 (Salikhov & Zavoiskaya, 2015), and the first application of *in vivo* EPR oximetry measurement was reported in 1986 (Subczynski et al., 1986). EPR spectroscopy uses exogenous probes to measure tissue oxygenation (Klare, 2012; Mallard & Kent, 1969; Swartz, 2004). Radical probes with unpaired electrons are sensitive to tissue environments, including O_2. Changes in the EPR signal due to the interaction of the probe with O_2 are used to determine O_2 concentration. However, the paramagnetic markers show significant toxicity, which limits their use in humans. The development of low toxicity probes and dedicated instrumentation for clinical applications will increase the utility of this technique.

MRI can image tumour O_2 *in vivo*, usually upon intravenous injection of perfluorocarbon or fluorinated nitroimidazole probes. When the magnetic field from the MRI is applied, the protons in the body line up parallelly or antiparallelly to the field. The protons are then stimulated with a radiofrequency current. When the radiofrequency field is turned off, the MRI sensors detects the energy released as the protons realign with the magnetic field. The time and the energy released by the protons to realign with the field changes depending on the

environment and the chemical nature of the molecules. The perfluorocarbon are used as biomarkers to detect these changes. This method, referred to as fluorine-19 (^{19}F) oximetry, can report on absolute values of O_2 concentration (Busse et al., 1988; Mason et al., 1994; Tirotta et al., 2015). Blood oxygen level-dependent MRI (BOLD-MRI) measures the fluctuations in the amount of O_2 bound to hemoglobin in the blood, i.e., % of O_2 saturation (Baudelet & Gallez, 2002; Li et al., 2008; Ogawa et al., 1990; Stacy et al., 2016), though it does not provide absolute O_2 concentrations. Dynamic contrast-enhanced MRI (DCE-MRI) is another promising method that can measure blood flow and blood volume in tissues (Gordon et al., 2014; Nielsen et al., 2012; Taylor et al., 1999).

PET is an *in vivo* tomographic imaging technique where organic molecular markers labelled with positron-emitting radioisotopes are used to measure the extent of hypoxia in tumours. The tracers are usually injected intravenously or inhaled. When the tracer reaches the target, it decays by emitting a positron which annihilates with nearby electron to produce two gamma rays. The PET scanner with an array of photoelectric crystals detects the gamma rays and constructs an image showing the location and concentration of the tracers which is used to quantify the hypoxia. However, PET has low anatomical resolution (Fleming et al., 2015; Gambhir, 2002; Holland et al., 2009; Koch & Evans, 2003). The advantage and disadvantage of the methods are listed in Table 1.2.

Table 1.2: Summary of the different O_2 detection methods.

Method	***Advantage***	***Disadvantage***
Polarographic electrodes	Quantitative point measurement of O_2 distribution	Invasive method
NIRS	Real-time, non-invasive measurement of tissue oxygenation	Measures vascular oxygenation; does not measure tissue O_2 levels
EPR	O_2 concentration measured from changes in ERP signal	Existing paramagnetic markers are toxic; lack of dedicated instrument for clinical application
MRI	Absolute measurement of O_2 concentration	Imaging compounds are affected by temperature, dilution, pH and blood; toxicity of nitroimidazole drugs
PET	Noninvasive; high sensitivity; quantitative; assessment of entire tumour volume	Lack spatial resolution

Other optical techniques include luminescence imaging. The method uses special photoluminescent probes which are quenched by O_2 and perform real-time quantitative O_2 measurements with high spatial resolution. Quenched luminescence detection of O_2 is a useful method.

1.3. Quenched-Luminescence Detection of O_2

Luminescence is the emission of light from electronically excited states. Based on the excited states, luminescence is classified into fluorescence and phosphorescence. The phenomenon can be illustrated by a Jablonski diagram (Figure 1.2).

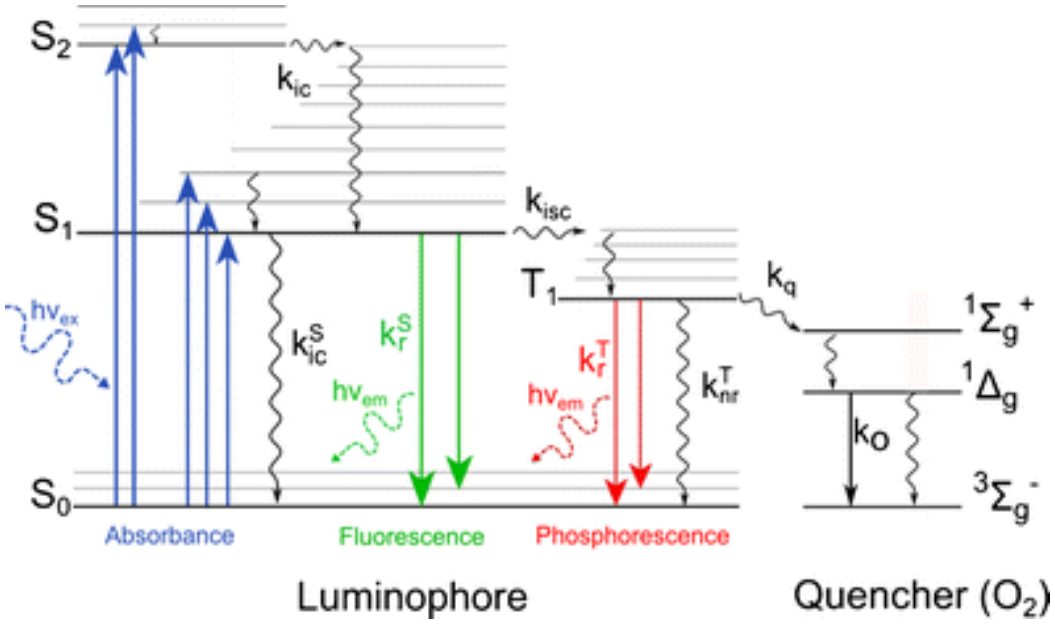


Figure 1.2: Jablonski diagram showing different photophysical processes occurring within O_2-sensitive luminescent sensors (Quaranta et al., 2012).

Fluorescence and phosphorescence intensities are affected by a variety of molecular interactions and processes that cause quenching. Being a triplet-state molecule, O_2 is one of the known collisional quenchers (Kautsky, 1939). Upon light excitation, luminophores absorb the photon and move to the excited singlet state (S_1 or S_2). Through intersystem crossing, it then quickly relaxes into the excited triplet state (T_1). Since the emission from the triplet state is slow, some excited dye molecules undergo quenching by collision with O_2, resulting in a

non-radiative return to the ground state (S_0). During collision, the paramagnetic O_2 in the ground state ($^3\Sigma_g^-$) accepts the energy from the luminophore and generates a short-lived excited state ($^1\Sigma_g^+$), followed by singlet O_2 ($^1\Delta_g$) and returns back to the ground state ($^3\Sigma_g^-$) (Quaranta et al., 2012). This reduces the phosphorescence intensity and lifetime in a manner that depends on the O_2 concentration.

Therefore, increasing O_2 concentration decreases the phosphorescence intensity and increases the phosphorescence decay rate (shorter lifetimes). The quenching of homogeneous samples by O_2 is described by the Stern-Volmer relationship (O. Stern and M. Volmer, 1919):

$$I_0/I = \tau_0/\tau = 1 + k_q\tau_0[O_2] = 1 + K_{sv}[O_2] \qquad \text{(eq. 1.1)}$$

Here, I_0 and I are the fluorescence intensity and τ_0 and τ are fluorescent lifetime in the absence and presence of O_2, respectively. k_q is the bimolecular quenching constant. The Stern-Volmer quenching constant is expressed as K_{sv}. The quantification of O_2 concentration is expressed as a function of the lifetime and Stern Volmer constant.

$$[O_2] = \frac{\frac{\tau_0}{\tau} - 1}{K_{sv}} \qquad \text{(eq. 1.2)}$$

However, the quenching of inhomogeneous samples cannot be described by the Stern-Volmer equation (eq. 1). The microheterogeneity in the system causes multiexponential decay curves, resulting in non-linear behaviour of the Stern-Volmer plot (Carraway et al., 1991). Hence, mathematical models and fits are used in this case to determine the lifetime and corresponding O_2 concentration.

1.4.Phosphorescent O_2 sensing materials

One group of phosphorescent emitters is based on luminescent transition metal complexes. These dyes have longer lifetimes (up to milliseconds) and larger Stokes shifts (>100 nm) that make them better suited for efficient separation of their signals from background fluorescence. Since molecular oxygen is recognized as a dynamic quencher of long-lived fluorescence, this phenomenon has been utilized to develop O_2 sensors. Transitional metal

complexes are well suited for O_2 sensing due to their long lifetimes, photostability, absorption in the visible range, and large Stokes shift.

Transition metal complexes typically undergo metal-ligand charge transfer upon photoexcitation, resulting in an excited triplet state. As back transitions of triplet-singlet are spin-forbidden, the triplet-state lifetimes are much longer. This allows oxygen to collide with the excited-state molecule, resulting in a high sensitivity to oxygen. Since the triplet states have less energy than singlet states, phosphorescence has a longer wavelength than fluorescence, and the large Stokes shifts facilitate the spectral separation. Some of the common O_2 sensors are based on ruthenium (II) and iridium (III) complexes and metalloporphyrins, which are strongly quenched by O_2. Structures of a few popular O_2-sensitive dyes are shown in Figure 1.3.

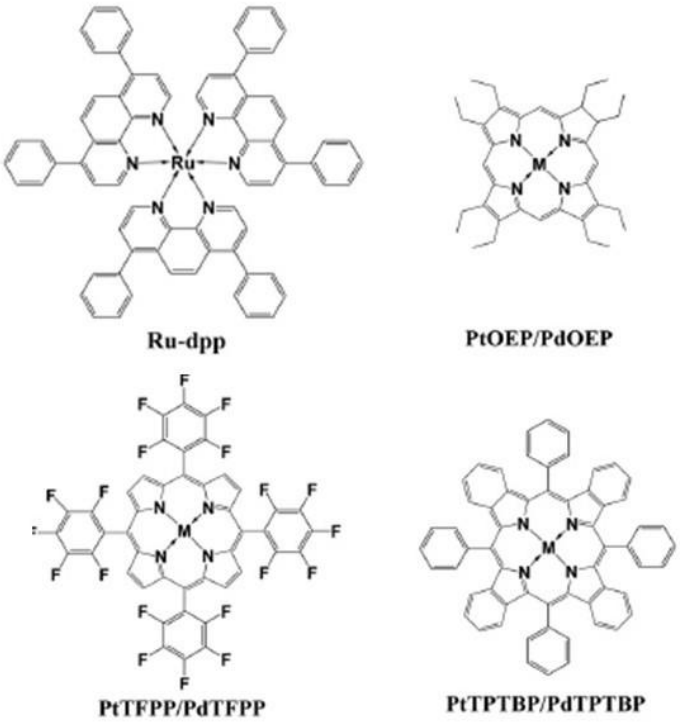


Figure 1.3: Dye structures of a few popular O_2-sensitive dyes.

The Ruthenium (II) complexes have a broad absorption band within 400–480 nm and emission at around 600 nm (Dmitriev & Papkovsky, 2012; Papkovsky et al., 2012; X. D. Wang & Wolfbeis, 2014). Their lifetimes in the low µs range make them appropriate for O_2 sensing and imaging, which can be tuned by varying the ligands and encapsulation media. Some of the commonly used

ruthenium (II) complexes include $Ru(bpy)_3$ (Wolfbeis et al., 1986), $Ru(phen)_3$ (Amao & Okura, 2003; Kuncova & Fialova, 1995; Liebsch et al., 1999), and $Ru(dpp)_3$ (X. Chen et al., 2002; Hartmann et al., 1995; McEvoy et al., 1997) but Ru (II) dyes have low solubility in hydrophobic matrices and are often adsorbed on SiO_2 or TiO_2 (Wolfbeis et al., 1986). The moderate quantum yield (usually 0.1), brightness, O_2 quenching ability, and high temperature sensitivity limit their use in O_2 detection.

On the other hand, the Ir (III) complexes are excellent triplet state emitters and widely used in organic LEDs (Longhi & De Cola, 2017). They are soluble in organic polymers, show remarkably strong luminescence with quantum yields between 0.2 and 1.0, and have long lifetimes (<2 μs) (Papkovsky et al., 2012; X. D. Wang & Wolfbeis, 2014). $Ir(ppy)_3$ is one of the complexes that can be immobilized in different polymer matrices and has the longest lifetimes (~1.5 μs) (Amao et al., 2001; Di Marco et al., 1996; Huynh et al., 2005). However, their application in solid-state O_2 sensors is limited due to their low molar absorption coefficient.

Other popular luminescent O_2 sensors are based on platinum (II) and palladium (II) complexes of porphyrins and related structures (Dunphy et al., 2002; Papkovsky, 2004; Papkovsky & O'Riordan, 2005; Rumsey et al., 1988). These dyes exhibit strong phosphorescence at room temperature and long lifetimes, which reduce strongly in the presence of O_2. While Pd (II) porphyrins have much longer lifetimes (400-1000 μs) and higher sensitivity to O_2 than their Pt (II) complexes (40-100 μs), the latter shows 2-3 times higher emission quantum yields (Amao & Okura, 2009; Eastwood & Gouterman, 1970). They have a strong absorption band in the UV (370-410 nm) and visible (500-550 nm) regions and an intense emission band (630-700 nm) in aqueous solutions.

Initially, a Pt(II) complex of octaethylporphyrin (PtOEP) (Papkovsky, 1995) was tested, but it showed poor photostability under UV light excitation (400 nm). To improve photostability, a perfluorinated meso-substituted porphyrin Pt(II)-tetrakis (pentafluorophenyl) porphine (PtPFPP) (S. K. Lee & Okura, 1997; Thomas et al., 2009) was used for continuous monitoring of O_2. The drawback of PtOEP and PtPFPP dyes was their weak absorption and excitation in the visible and longwave spectral range. This was overcome by synthesizing substituted Pt(II) and Pd(II) benzoporphyrins which had intense red excitation bands and

bright emission in the NIR region (Borisov et al., 2008; Borisov, Nuss, et al., 2009; Borisov, Papkovsky, et al., 2009) and high photostability. In comparison to PtPFPP and PtOEP, benzoporphyrins exhibit much stronger Q-band absorption and higher quantum yield. A number of Pt(II) and Pd(II) benzoporphyrin dye structures have been developed and used for O_2 sensing in various applications (Banerjee, Kelly, et al., 2016; Borisov et al., 2008; Dmitriev & Papkovsky, 2012; Dunphy et al., 2002; Kelly et al., 2018b; Lebedev et al., 2009; X. D. Wang & Wolfbeis, 2014).

O_2-sensitive materials are produced by placing these phosphorescent dyes in suitable quenching media to achieve optimal quenching properties. Polymers are widely used as the quenching media, which helps to achieve the desired sensitivity, response time, biocompatibility, and format (solid-state coatings or nanoparticle probes) of the sensor material (X. D. Wang & Wolfbeis, 2014). The O_2 sensing materials are classified into different formats, as described below.

1.4.1. Solid state sensors

In solid-state sensors the dye molecules are dispersed within the polymer and thus shielded from quenching interferences by a gas diffusion barrier. They allow repeating measurements without sample contamination and facilitate quantitative O_2 measurements even in intensity mode. The sensors are usually produced in the form of a coating or a thin film. The phosphorescent dye in polymeric matrices is immobilized as thin film coatings on the surface of solid supports like microwells, cuvettes, microscopy dishes, biochips, customized cells, and fluidic chambers (Grist et al., 2010; Molter et al., 2009). They are easy to fabricate and tune, allowing contactless measurements (Table 1.3). In contrast, fiber optic sensors are small and flexible, allowing O_2 measurements in small areas of the sample with slight penetration of biological tissues. They have high spatial resolution and stable calibration within 0–100% O_2 and can be manufactured with different dyes and polymeric matrices depending on the application. Although solid-state sensors are simple and allow accurate extracellular O_2 measurements, they are not compatible with monitoring 3D O_2 gradients and intracellular measurements in complex biological samples.

1.4.2. Soluble O_2 probes

Soluble probes, in contrast to solid-state sensors, are not bound to any solid surface and can be distributed across the aqueous sample. This sensor format allows screening applications and O_2 imaging/mapping in different biological samples ranging from cultured cells to 3D respiring micro-tissue samples (e.g. spheroids and organoids) and even whole organs and live organisms. The soluble probes are categorised into the small molecule and supramolecular probes. The small molecule probes have hydrophilic dye structures, allowing good solubility in aqueous media. The water solubility is usually achieved by introducing carboxylic and sulfonate groups in the structure. Examples include: Pd-meso-tetra [4-carboxyphenyl] porphine (PdTPCPP) (Hogan, 1999; Shonat & Kight, 2003), Ru(II) dyes (Lakowicz et al., 1997), and tetracarboxylic platinum(II)-coproporphyrin (PtCP) derivatives (Fercher et al., 2010). However, such probes still often bind to proteins, cells, or surfaces with hydrophobic regions in their structure. These issues were partially overcome by the supramolecular probe, where the dye molecules were covalently bound to a hydrophilic macromolecular carrier such as protein, to improve the O_2 sensing properties and cell permeability. The dendritic probes, based on Pt(II) porphyrin and benzoporphyrin with poly(glutamate) dendrimeric shell, are cell impermeable and highly soluble in physiological liquids. They are mostly used for extracellular intravital sensing. Some examples of the probes are given in Table 1.3.

1.4.3. Micro and nanoparticle-based probes

Here the phosphorescent dye molecules are encapsulated in a polymeric shell that protects them from the cellular environment, quenching, and photodegradation. Nanoparticle probes (NP) are fabricated by impregnation of commercial polymeric beads (e.g., polystyrene), inclusion of indicator dyes during emulsion polymerization (Chu & Lo, 2011), and precipitation of nanostructures (Borisov, Mayr, et al., 2009). They exhibit high brightness, photostability and combine the advantages of both the solid-state sensors and the soluble probes. NP probes are based on hydrophobic dyes that are otherwise toxic and not soluble in water but provide optimal photophysical properties. Pairs

of dyes that combine a reporter dye with a luminescent reference are used as NP probes for ratiometric imaging of O_2. Some of the limitations of NP probes include their significantly large size (>40 nm), composition and structural reproducibility, stability under prolonged storage, biocompatibility, and toxicity in *in vivo* applications.

1.4.4. Cell permeable O_2 probes

The cell-permeable probes allow intracellular O_2 sensing and imaging. One group of intracellular O_2 probes is produced by conjugating the phosphorescent dyes with cell-penetrating peptides that are used for intracellular or subcellular targeting. Nanoparticle based probes are also used for intracellular O_2 imaging. They usually provide intracellular staining after long hours of incubation and have significant cytotoxic effects. But, the recent development of the NP probe based on the RL100 polymer and PtTFPP dye has a minimal cytotoxic effect and allows for fast and bright intracellular staining (Fercher et al., 2011).

Table 1.3: Phosphorescent O_2 sensing materials and applications.

Format	**Sensor**	**Detection**	**Application**	**Reference**
Fiber optic sensor	PtOEP derivative in PS	Intensity-based	Sensing of O_2 in growing live cells.	(Papkovsky, 1995)
Small molecule probe	PdTPCPP	Lifetime-based	Sensing of intracellular O_2 in isolated skeletal muscle fibers.	(Hogan, 1999)
Sensor foil	PtOEP in polyester	Intensity-based	Imaging of the O_2 gradients in tissue.	(Kellner et al., 2002)
Dendritic probes	Oxyphor G2	Lifetime-based	*In vivo* O_2 sensing in tumour	(Dunphy et al., 2002)
Supramolecule probe	PdTPCPP	Intensity-based	O_2 imaging in the mouse retina.	(Shonat & Kight, 2003)
Cell permeable probe	$Ru(Ph_2phen)_3Cl_2$ immobilized in poly-electrolyte multilayers	Intensity-based	Ratiometric sensing of intracellular O_2 in mammalian cells.	(Guice et al., 2005)
Small molecule probe	$[Ru(bpy)_2(pic)]^{2+}$ conjugates	Lifetime-based	Cellular imaging of myeloma and human blood platelets.	(Neugebauer et al., 2008)
Dendritic probes	Pt and Pd complexes of porphyrins and π-extended porphyrins	Intensity-based	*In vivo* imaging of vascular O_2 in the rat brain.	(Lebedev et al., 2009)
Nanoparticle probe	PtOEP dopped polyfluorene nanoparticles	Intensity-based	O_2 imaging in cells.	(Wu et al., 2009)
Nanoparticle probe	Oxyphor G2 and reference dye in hydrogel	Intensity-based	Ratiometric imaging O_2 levels in live cancer cells.	(Koo Lee et al., 2010)
Cell permeable probe	PtCP conjugate	Lifetime-based	Sensing of intracellular O_2 in cultures of mammalian cells	(Dmitriev et al., 2010)
Cell permeable probe	PtTFPP in RL-100	Intensity/ Lifetime-based	Intracellular O_2 Sensing.	(Fercher et al., 2011)
Nanoparticle probe	$PtTF_{20}PP$ in polystyrene beads	Intensity-based	Intracellular O_2 imaging.	(X. D. Wang et al., 2011)
Polymeric film	PtBP on polyester film	Intensity-based	*In vivo* imaging of cellular O_2 metabolism in brain tissue.	(Tsytsarev et al., 2017)

1.5. O_2 Detection Modalities

1.5.1. Intensity and Ratiometric Intensity based sensing

Intensity-based measurements represent a straightforward method of quenched photoluminescence O_2 detection. The O_2-sensitive luminophores change their intensity depending on the O_2 concentration. The method involves excitation of the luminophores at an optimal wavelength and detection of the emission intensity at a single wavelength (Figure 1.4a). The luminescence is collected by detectors like photomultipliers (Wilson et al., 1987), photodiodes (Papkovsky, 1995), and charge-coupled devices (CCDs) to generate 2D O_2-maps (Grist et al., 2010; Rumsey et al., 1994). Measurement of O_2 distribution with intensity-based imaging of phosphorescence was demonstrated on intact rat livers (Rumsey et al., 1988). A CCD camera was used to collect the phosphorescence, and 2D images of O_2 distribution in the tissue was generated. A detailed description of the method is discussed in Section 1.7.

Time-resolved fluorescence (TR-F) measurements are also based on intensity detection but provide an improved signal-to-noise ratio and accurate O_2 detection (Dmitriev & Papkovsky, 2012). The luminophores are excited with short excitation pulses, and the emission intensity is measured after a short time delay (t_1), from which the lifetime and corresponding O_2 concentration are calculated (Figure 1.4b). This time delay helps to exclude interferences from autofluorescence and short-lived light scattering. Despite losing a fraction of the luminescence emission, it provides a large improvement in the signal-to-noise ratio. TR-F is generally used to measure long-lived fluorescence or phosphorescence (Hynes et al., 2006). A fluorescence plate reader was used to measure mitochondrial respiration in a 96-well plate. A phosphorescent O_2-sensitive probe, A65N-1, was added to mitochondrial stock, and the fluorescence intensity was collected at a time delay of 30 μs for a measurement window of 100 μs. The O_2 consumption rate was determined by analyzing the time profiles of the fluorescence intensity at each well. However, incomplete sealing of the

microwell plates led to lower O_2 consumption readings in comparison to polarographic system measurements (Hynes et al., 2006).

These techniques have certain disadvantages: intensity measurements are prone to photobleaching, leaching, measurement geometry, and optical interferences caused by light scattering and autofluorescence from biological samples that affect probe calibration and lead to incorrect O_2 readings. These make the measurements mostly qualitative rather than quantitative. However, intensity-based measurements have been used in many applications (Itoh et al., 1994; Koo et al., 2004; Z. Lin et al., 2009; O'Donovan et al., 2005; Rumsey et al., 1988).

To overcome these disadvantages, a ratiometric sensing method was proposed (Borisov & Klimant, 2009; Feng et al., 2012; Kondrashina et al., 2012; Park et al., 2005). This technique uses sensors containing an O_2-sensitive and an O_2-insensitive dye with different emission spectra. When the excitation source excites the sensor, the emission intensity of the O_2-sensitive dye is quenched in the presence of O_2, and the sum of the two emission spectra is detected. The O_2 concentration is determined by measuring the ratio between the two emission spectra (Figure 1.4c). Ratiometric sensors, RGB PEBBLEs, were prepared by adding a mixture of O_2 insensitive reference dye and O_2 sensitive platinum(II) meso-tetrakis-(pentafluorophenyl)porphyrinato ($PtTF_{20}PP$) complex to polystyrene beads (X. D. Wang et al., 2011). These were incorporated in epithelial normal rat kidney to measure intracellular O_2. An inverted epifluorescence microscope was used to collect the emission signals in the green and red channels of the CMOS or CCD colour camera. While the red emission was sensitive to O_2 quenching, the green emission was stable with varying O_2 concentrations. Although this method reduces the effects of the optical interferences, as both the emission spectra are affected by these factors, but they are still influenced by photobleaching and autofluorescence from the sample.

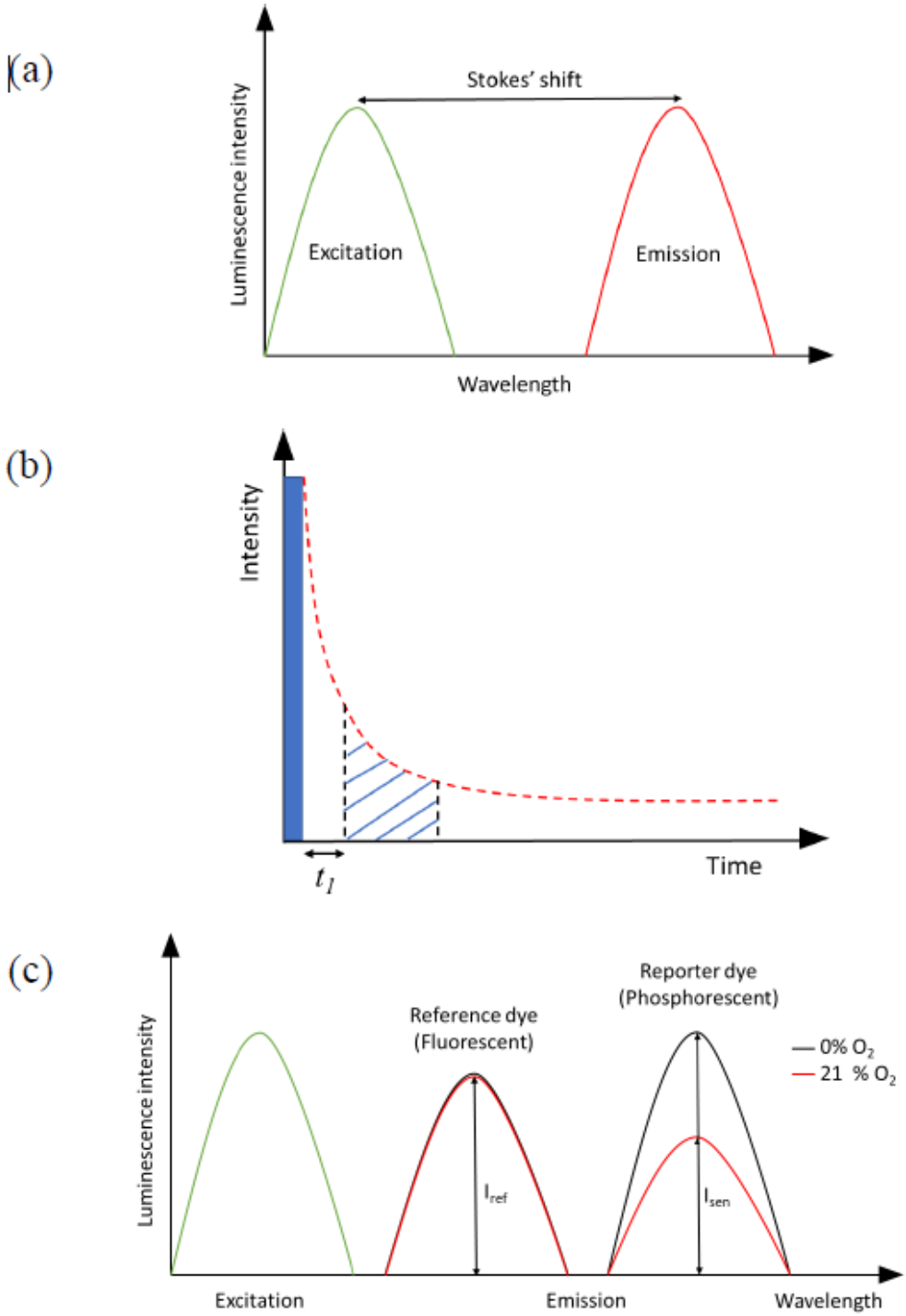


Figure 1.4: Intensity-based detection. (a) Phosphorescence intensity spectra measurement at a single wavelength with a large Stokes' shift. (b) Principle of Time-Resolved Fluorescence (TR-F) Measurement. (c) Ratiometric measurement. Excitation and emission spectra of O_2-sensitive and reference dyes at 0 and 21% O_2.

1.5.2. Lifetime based sensing

Lifetime-based measurements have advantages over intensity-based methods. As luminescent lifetime is an intrinsic property of the dye, it is independent of factors like dye concentration or the inhomogeneous distribution of the dye. Also, luminescent lifetime is less sensitive to photobleaching, measurement geometry, and instrument instabilities, which makes it a preferable technique for accurate and quantitative measurement of O_2 (Papkovsky & Dmitriev, 2013).

Lifetime measurements can be mainly classified into time domain and frequency domain techniques. Time-domain detection uses short excitation pulses to excite the sample. The time-dependent intensity is measured after the excitation, and the luminescence decay is calculated from the time at which the intensity decreases to 1/e of the intensity at t = 0 (Figure 1.5a) (Lakowicz, 2006). Time-Correlated Single Photon Counting (TCSPC) is the most advanced time-domain detection technique. The luminophores are excited with high-frequency, short excitation pulses, and the arrival times of individual photons are detected and stored in a histogram (Figure 1.5b) that constructs the lifetime decay. The O_2 calibration function is used to convert the lifetime values to O_2 concentrations (Jenkins et al., 2015). TCSPC is combined with confocal or multi-photon laser scanning to perform fluorescence or phosphorescence lifetime imaging (FLIM or PLIM) (Becker, 2012, 2018). This method was used to study real-time monitoring of oxygenation of the whole spheroid (Dmitriev et al., 2013). Cells isolated from embryonic rat brain were stained with cell-penetrating O_2 probes, NanO2 and MM2, and excited with a picosecond laser. The PLIM imaging was performed with the DCS-120 confocal scanner with a photon counting detector and TCSPC hardware. Since PLIM eliminated the influence of probe concentration, it produced a stable quantification of O_2 in the region of interest compared to wide-field PLIM.

The rapid lifetime determination method (RLD) is a mathematical technique for rapid evaluations of exponential decay lifetimes (Sharman et al., 1999). TR-F with RLD can be used to measure luminescence intensity (F_1, F_2) at two different time delays (t_1, t_2) after the excitation pulse (Figure 1.5c) (Dmitriev & Papkovsky, 2012; O'Riordan et al., 2007). The areas under the two regions of the

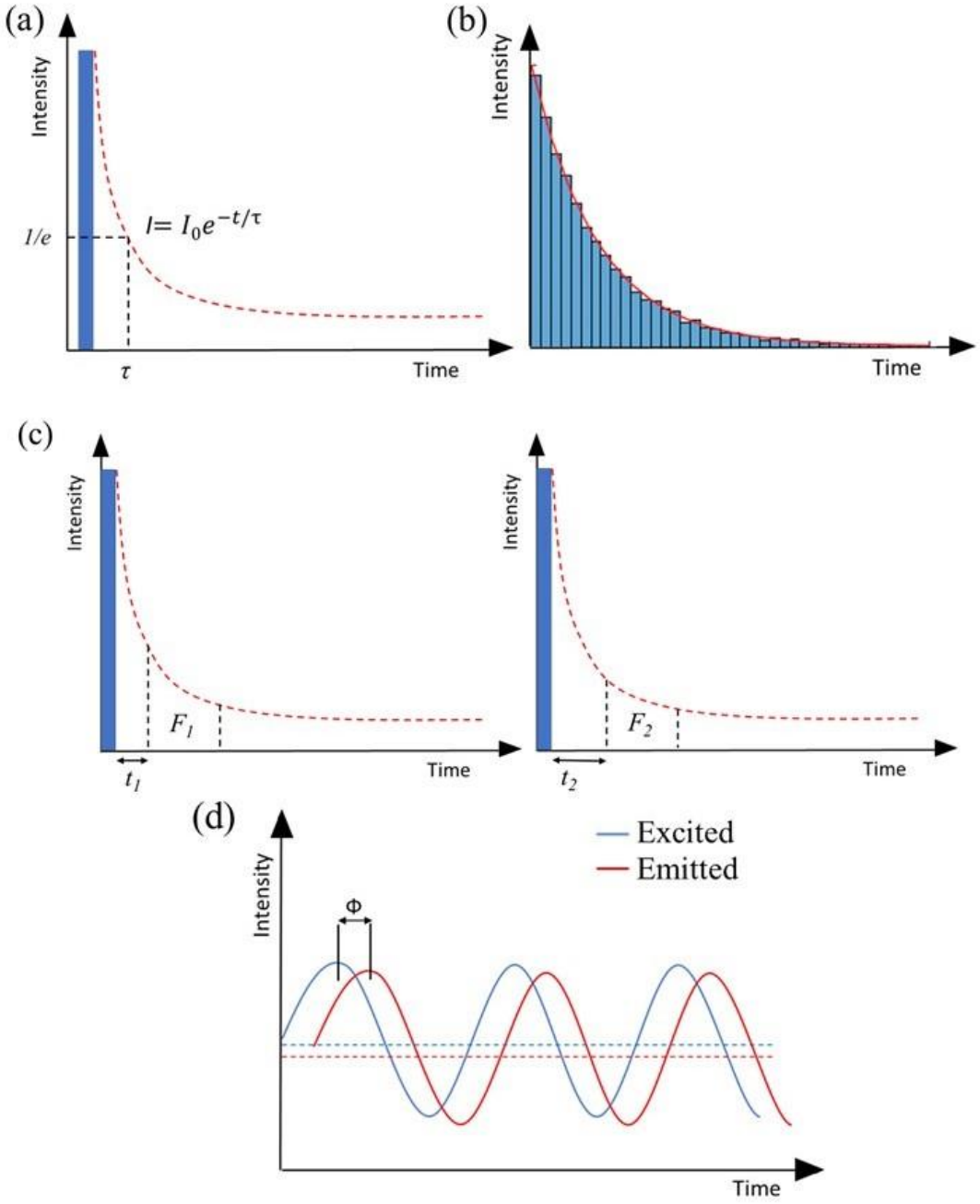


Figure 1.5: Lifetime-based detection. (a) Time-domain lifetime detection; (b) Principle of TCSPC measurements; (c) Schematic presentation of the RLD method; (d) Frequency-domain measurement.

decay are then used to calculate the lifetime and corresponding O_2 concentration using the calibration equation. This method was used to measure intracellular O_2 in live mammalian cells (O'Riordan et al., 2007). Cultured cells were mixed with an O_2-sensitive MitoXpress probe in a microwell plate and the TR-F

intensities were measured at 30 and 70 µs delay time and 100 µs gate time. Measured TR-F intensity signals were converted to lifetime values. The main drawback of the system is its limitation to a single exponential approximation of the decays.

Phase fluorimetry is a frequency domain technique where the luminophores are excited with intensity-modulated light. The phase shift of the emitted luminescent signal is used to calculate the lumisecence decay (Figure 1.5.d) (Lakowicz, 2006; Valledor et al., 2006). The heterodyne principle in combination with a single-point detector and scanning (e.g., ISS) or wide-field detection with a modulated image intensified camera (e.g., Lambert Instruments) are mostly used in commercial frequency domain systems (Jenkins et al., 2015). Phase measurements can be affected by optical interferences from complex biological samples that may lead to unstable probe calibration and incorrect O_2 reading (X. D. Wang et al., 2010). Phase fluorimetry was used on O_2-sensor microbeads to perform O_2 measurements in different microtissue culture environments using an inverted phase contrast microscope and digital CCD camera (Lesher-Pérez et al., 2017).

1.5.3. O_2 imaging

Lifetime imaging is gaining popularity in biological and medical research (Berezin & Achilefu, 2010; Korczyński & Włodarczyk, 2009; Marcu, 2012; Z. Wang et al., 2018) as it can provide quantitative, calibration-free imaging readouts and minimize measurement artefacts. The technique was pioneered by David Wilson et al. (Wilson et al., 1987) and later developed into confocal microscopy, two-photon laser microscopy, fluorescence and phosphorescence lifetime imaging microscopy (FLIM/PLIM), etc. Of these, FLIM/PLIM techniques are widely used to generate two-dimensional maps of O_2 in many different tissues, including the brain cortex (Tsytsarev et al., 2013, 2017; Wilson et al., 1991, 1993), the heart (Rumsey et al., 1994), the eye (Shonat et al., 1992; Wilson, Vinogradov, Grosul, Vaccarezza, et al., 2005) and tumours (Babilas et al., 2005; Wilson & Cerniglia, 1992). These studies provided detailed

information on the distribution of the probe in the sample microenvironment along with the probe's lifetime.

Wide-field FLIM/PLIM:

In wide-field FLIM/PLIM imaging, the whole field of view is imaged simultaneously onto a camera with either gating or frequency-domain methods. One technique relies on a gated CCD camera coupled to a photon counting image intensifier such as the microchannel plate (MCP). The gated image intensifier provides time resolution as fluorescence decay is calculated from a set of intensity frames acquired with different delays after the excitation pulse. This, however, leads to the loss of photons outside the MCP gate and is influenced by sample photobleaching or any other time-dependent effects. Some examples are discussed in Section 1.7 (Rumsey et al., 1994; Shonat et al., 1992). In the frequency domain, FLIM, on the other hand, uses a gain-modulated image intensifier and CCD detector to record the amplitude difference and phase delay between the excitation and emission signals. The phase shift obtained is related to the fluorescent lifetime of the fluorophore. This frequency domain approach was used to image O_2 distribution in the retina of the mouse eye (Wilson, Vinogradov, Grosul, Kuroki, et al., 2005). An O_2-sensitive probe, Oxyphor G2, was injected in the tail vein of an anesthetized mouse. The excitation LED light source was modulated with a square wave with 50% duty cycle, and the phosphorescence intensity images were collected from the dilated pupil with an intensified CCD camera modulated at the same frequency and delayed by different phase angles with respect to the excitation. The phosphorescence lifetime map was generated by fitting the phosphorescence intensity and calculating the phase shifts at each pixel. The Stern-Volmer relationship was then used to convert the lifetime values to O_2 concentration. Although these techniques are advantageous for real-time monitoring, they are not single-photon sensitive (Becker, 2015) and usually require high signals and are influenced by scattered light, photobleaching, and autofluorescence (Becker, 2012; Hirvonen & Suhling, 2017; Sparks et al., 2017).

Fast wide-field FLIM/PLIM with single photon sensitivity has been demonstrated with a photon counting image intensifier and a complementary

metal oxide semiconductor (CMOS) camera. The location and arrival time of the photons in each frame were extracted with software and lifetime images were obtained by fitting an exponential decay function to the arrival time histogram in each pixel (Hirvonen et al., 2014). The time resolution in this case is limited by the camera frame rate. To improve time resolution, this technique was extended by exploiting the invariant decay of the image intensifier's phosphor screen to determine the arrival time of the photons with sub-exposure time accuracy. The detection of the position of the photon by the centroiding technique along with single photon sensitivity provide excellent spatial resolution, a time resolution of 40 ns, and a framerate of 250 kHz for the image size of 80 x 128 pixels. This method is applicable for luminescence lifetime imaging within a 100 ns-100 μs timescale (Hirvonen et al., 2015; Petrášek & Suhling, 2010). This was used to image O_2-sensitive Ru compound, $Ru(dpp)_3^{2+}$, added to living HeLa cells. A pulsed diode laser was triggered from the camera to illuminate the sample once during each exposure of the decay. The emission was collected by an intensifier operating in photon counting mode and, the phosphor screen was imaged onto the CMOS camera using photographic lenses. The average lifetime was found to be 2.95 μs with a fast component of 0.04 μs from cellular autofluorescence. So, the decays were fit with double exponential function.

TCSPC-FILM/PLIM:

The classical technique for recording fluorescence lifetimes is TCSPC, in which a pulsed excitation laser is coupled with a single photon counting detector, which uses fast timing electronics to detect the emitted photons and then extract the characteristics of emission decay (Becker, 2005). A short excitation pulse is sent to the sample and timing electronics to start the timer, and a stop signal is generated when the system detects the first photon. After multiple excitation and recording events, an emission decay profile is obtained. Figure 1.6 illustrates how the histogram is formed after multiple cycles.

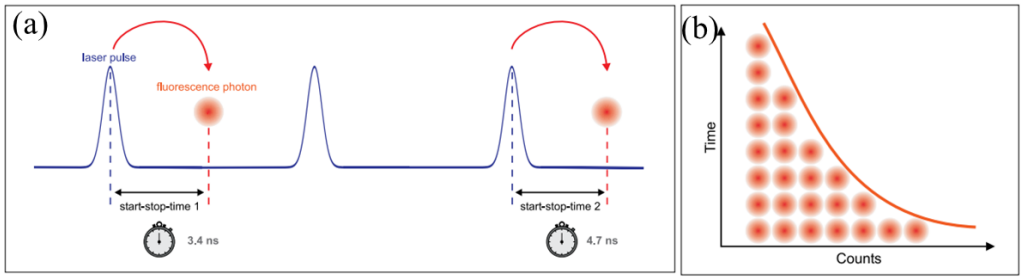


Figure 1.6: (a) Measurement and (b) histogram of start-stop times in time-resolved fluorescence measurement with TCSPC (Wahl, 2014).

The modern implementation of TCSPC is a multi-dimensional TCSPC process where the photon arrival time with respect to the laser pulse and the position of the laser spot are recorded while the detection of a photon is also recorded (Becker, 2005, 2015). So, an array of pixels, each containing a lifetime decay curve in a large number of time bins, is generated. The multidimensional TCSPC operating at a high speed with large area photon counting detectors allowed accurate lifetime detection with high sensitivity and optical sectioning capability. However, it requires fast excitation sources, high-speed detectors, and special TCSPC hardware (Quaranta et al., 2012).

The digital nature of TCSPC, based on whether a single photon is seen or not, makes it a precise and robust technique. It follows the Poisson statistics, which states that the experimental uncertainty is equal to the square root of the number of counts and that the signal-to-noise ratio increases with measurement time (Hirvonen & Suhling, 2017). The time ranges from picoseconds to microseconds, which makes fluorescence decay easy to visualize. TCSPC offers high signal-to-noise ratio and allows multi-exponential fluorescence decay fitting.

For FLIM, this TCSPC technique is combined with pixel-by-pixel scanning of the sample. For thick samples, the imaging depth and contrast can be improved by using a confocal laser scanning setup with pinhole optics, which prevents unfocused light from reaching the detector, or two-photon excitation. Laser scanning TCSPC-FLIM has advanced in recent years in its optoelectronic components, sensitivity, excitation sources, and emission range and has been implemented in clinical applications. A TCSPC module with a temporal instrument response function (IRF) of 250 ps in width is used to measure autofluorescence in dermatology to study various physiological and pathological conditions of the skin in *in vivo* and *ex vivo* samples (Seidenari et al., 2012). In

ophthalmology, a fluorescence lifetime imaging ophthalmoscopy (FLIO) system consisting of a pulsed laser source, a confocal laser scanning ophthalmoscope (cSLO), and a sensitive detector for single photon detection is used to detect retinal diseases such as Stargardt disease, age-related macular degeneration, choroideremia, diabetic retinopathy, and retinal artery occlusion (Dysli et al., 2017). Optical metabolic imaging of autofluorescence from NAD(P)H and FAD with a multiphoton fluorescence lifetime system and photomultiplier tube detector (Sharick et al., 2019) was used to study cancer. Nanosecond FLIM with short-lived fluors is actively used, e.g., in the analysis of cell autofluorescence, pH, Ca^{2+}, glucose dynamics, and other parameters (Agronskaia et al., 2004; Lakowicz, Szmacinski, Nowaczyk, Berndt, et al., 1992; H. J. Lin et al., 2003; Orte et al., 2013; Veetil et al., 2012; Zheng et al., 2018). O_2-sensitive fluorescent dye $[Ru(bipy)_3]^{2+}$ was used to measure spatial O_2 gradients at 400 nm spatial resolution. A two-photon excitation laser was used to excite the dye, and the emission was collected with a TCSPC confocal microscope with a photomultiplier tube detector (Hosny et al., 2012).

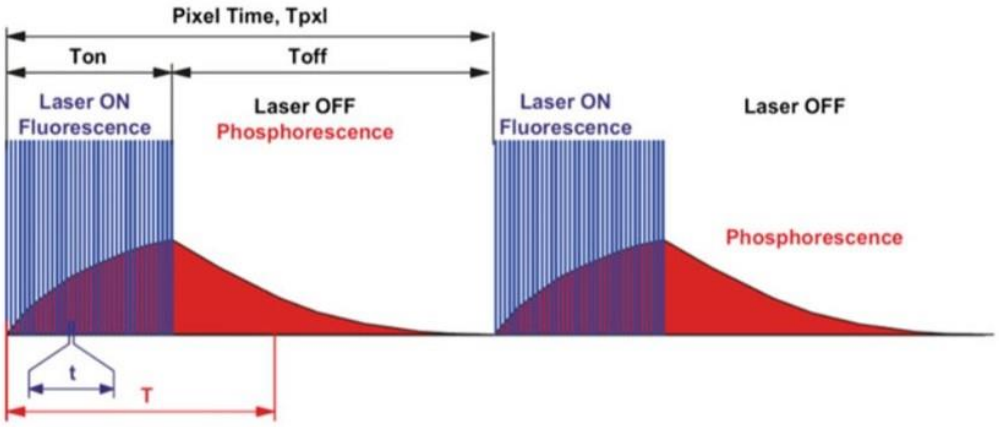


Figure 1.7: Principle of simultaneous FLIM/PLIM with TCSPC. FLIM is recorded in the "Laser ON" phases, PLIM in the "Laser OFF" phases (Chelushkin & Tunik, 2019).

PLIM is mainly applied in quenched-phosphorescence imaging of O_2 in various biological samples (Dmitriev & Papkovsky, 2012; Jenkins et al., 2015; Kalinina et al., 2018), using long-decay photoluminescent materials based on transition metal complexes and metalloporphyrins, with lifetimes in the microsecond time range.

The most established approach to PLIM is raster scanning confocal techniques with TCSPC (Chelushkin & Tunik, 2019), because of two key advantages: (i) high axial resolution due to confocal scanning; and (ii) precise lifetime measurements with TCSPC. The phosphorescence photons are collected by scanning the samples pixel by pixel. During the pixel dwell times, the phosphorescence is excited by high-frequency laser pulses. The laser is then turned off, and the phosphorescence photons are collected to build up the lifetime distribution. This process allows simultaneous detection of FLIM of fluorescent photons during the laser-on period (Becker et al., 2017), as shown in Figure 1.7.

In TCSPC, photons are registered by very fast electronics. Since fluorescence lifetimes are in the ns range, only the first photon reaching the detector after one excitation pulse is recorded. Any additional photons reaching the detector are lost due to the dead time of the electronics. This leads to the pile-up effect, where the photon statistics get skewed toward shorter arrival times (Buschmann et al., 2016). But phosphorescence lifetimes, in the µs-ms range, are longer than the detector dead time (ns-range) and are not influenced by such effect.

After-pulsing of the detectors is another important feature that occurs in a time range of hundreds of nanoseconds. Hence, this is only visible in the phosphorescent measurements as a small bump at the end of the decay. To overcome this, TCSPC PLIM generally uses hybrid-PMT detectors with low after-pulsing or gated SPAD detectors that remove these artifacts (Buschmann et al., 2016). However, the pixel-by-pixel scanning still leads to slow image acquisition times (Becker, 2012, 2018; Wei et al., 2017) for PLIM, where long pixel dwell times are required to record the long-lived phosphorescence.

So far, FLIM/PLIM has been used mainly in microscopic imaging, while macroscopic applications are less common. The DCS-120 MACRO FLIM/PLIM confocal imager offered by Becker and Hickl (Germany) (Chelushkin & Tunik, 2019) can image objects up to a size of 15 mm with high resolution, but it is still slow due to its scanning mode. On the other hand, macroscopic luminescence imaging is in demand for biomedical and life sciences, where currently intensity-based imagers are mostly used (Zarychta-Wiśniewska et al., 2017), which lack accurate and quantitative optical readout.

Several O_2-sensitive phosphorescent probes have been designed for PLIM (section 1.4). Of them, Pt(II)- and Pd(II)-porphyrins are most popular for O_2

sensing (Dunphy et al., 2002; Papkovsky, 2004; Rumsey et al., 1988). TCSPC PLIM was used to test several cell-penetrating phosphorescent conjugates of PtPFPP dye for O_2 imaging in 3D tissue models (Dmitriev et al., 2014). The PLIM imaging was performed with the DCS-120 confocal scanner. Cells stained with the O_2-sensitive probes were excited with a picosecond diode laser or a picosecond supercontinuum laser and, the emission was collected with a photon counting detector connected to the scanner and TCSPC hardware. The phosphorescence lifetimes were calculated from the monoexponential decay fits. *In vivo* O_2 imaging of hepatic tissues injected with Ir(II) complexes were also measured with the same confocal scanner and TCSPC hardware and, the emission was detected with a hybrid detector module. The decay curves were fitted with single or double exponential function for PLIM analysis (Mizukami et al., 2020).

Two-photon PLIM:

Two-photon PLIM (2P PLIM) is another popular detection technique that uses two-photon excitation and a confocal scanning microscope for O_2 imaging (Becker, 2015; Göppert-Mayer, 1931). Multi-photon microscopes use a picosecond or femtosecond Ti:Sapphire laser at an NIR wavelength for 2P excitation, which allows deeper penetration into the tissue with a low scattering coefficient. It can excite fluorescence in tissue layers up to 100 µm deep and, in some cases, even 1 mm (Diaspro et al., 2001; König, 2000). Another advantage of 2P PLIM is its two-photon excitation trapped within the focus that allows optical sectioning, depth resolution, and elimination of the out-of-focus fluorescence. This also limits the absorption and sample damage within a thin layer in and around the focal plane of the microscope, which makes it suitable for live cell and tissue imaging (Fischer et al., 2008; König, 2000; König et al., 1996). O_2 detection with 2P microscopy was possible with the development of two-photon–enhanced phosphorescent nanoprobes like PtP-C343 and Oxyphor 2P (Esipova et al., 2019; Lebedev et al., 2009; Sakadzić et al., 2010). The development of the probes and their applications are discussed in Section 1.7. 2P ratiometric measurements were performed on the spheroids stained with MM2 probes (Dmitriev et al., 2013). The samples were excited with a Ti:Sapphire laser

and the emission was collected with an upright microscope in PhotonCount detection mode. The combination of 2P imaging and MM2 probe provided deeper light penetration and better contrast.

1.6.New development in FLIM hardware

Solid-state single photon detectors were recently introduced to wide-field TCSPC-FLIM. Here, single photon avalanche photodiodes (SPADs) were integrated into compact imaging array detectors. A SPAD is a p-n junction diode that is biased above the breakdown voltage so that a single photon can generate an electron-hole pair, leading to avalanche signal multiplication. SPAD array sensors have single photon sensitivity and picosecond time resolution, and each pixel can independently perform TCSPC. While being a very promising technology due to excellent time resolution, current SPAD imagers still require improvements in SPAD photon detection efficiency, array density, and dark count rate (Gersbach et al., 2010; Hirvonen & Suhling, 2017). Large-format SPAD arrays were also used for subsurface fluorescence Light Detection and Ranging (LiDAR) technique to quantify concentration of fluorescent molecules in heavily scattering media, such as tissue, with submillimeter depth accuracy (Bruza et al., 2021).

Tpx3Cam:

A new technology with parallel photon detection in each pixel was implemented in the TimepixCam camera (Fisher-Levine & Nomerotski, 2016; Nomerotski, 2019). The camera is based on the XRI UNO X-ray camera (X-Ray Imatek S.L., Spain) with ~10 fps continuous readout rate which is limited by the USB bandwidth. The novel time-stamping optical imager is fitted with a Timepix chip (Llopart et al., 2008) and an optimized optical sensor.

The Timepix detector was originally developed from the Medipix1 system or Photon Counting Chip (PCC) developed in the 1990s. It was used to detect particles in high energy physics experiments (Mikulec, 2000; Mikulec et al., 2001). The sensor had 64x64 pixels with 170x170 μm^2 pixel area. The Medipix2 with sub-micron CMOS technology had a higher number of pixels with a smaller

pixel size (55x55 μm^2) (Bello et al., 2001; Chmeissani & Mikulec, 2001). Timepix is a developed extension of the Medipix 2.

The Timepix is a time stamping readout chip with 256x256 pixel bump bonded to the silicon sensor. Each pixel, 55x55 μm^2 in size, is connected to processing electronics that record the time of arrival of photon events that cross a preset threshold. The timecode of the detected photons is stored in 14-bit memory. Since pixel noise is about 100 electrons, the threshold value is set above 650 electrons to reduce the noise (Llopart et al., 2008). Each pixel is also connected to a 4-bit digital-to-analog converter that allows threshold adjustment using an equalization algorithm.

The silicon sensor has a thin entrance window to allow efficient transmission of photons to the sensitive volume of depleted silicon. Standard p-on-n 300 µm thick silicon wafers were used for the sensors. In addition to the thin passivation layer, an anti-reflective coating optimized for 400-500 nm photons was deposited across the sensor. This layer improved the sensitivity by decreasing the reflection to 5% in uncoated silicon and was optimized for the emission spectrum of P47 phosphor. The time resolution of the imager was 15 ns, and the quantum efficiency of the sensor was more than 90% in 400-900 nm wavelength range (Nomerotski et al., 2017).

The camera has been used in several applications, including imaging mass spectrometry, quantum imaging, and optical readout of a liquid argon time-projection chamber (Al Darwish et al., 2019; Beacham et al., 2011; Fisher-Levine et al., 2018; Procz et al., 2019). The combination of a timepix camera with a photon counting image intensifier has also been demonstrated in PLIM of 200 µm polystyrene beads stained with a long-decay fluorescent iridium complex. The setup was built on a Nikon Eclipse TE2000-U inverted microscope, and a pulsed diode laser at 485 nm was used for excitation. An image intensifier with a P47 phosphor screen and S20 photocathode with a peak quantum efficiency of 15% at 510 nm was in the image plane. Synchronized signals were sent to the camera and the laser at a repetition rate of 300 Hz, and the images were read at ~10 Hz frame rate. The instrument response was measured by overlaying a 1951 USAF resolution test chart on a fluorescent plastic slide, achieving 15 ns timing resolution and ns-scale lifetime resolution (Figure 1.8) (Hirvonen et al., 2017). The system operated in the visible range and

microscopic format, which are not optimal for biomedical applications. The main limitation of the camera was a slow readout, which allowed only 10 frames per second leading to very long image acquisition times.

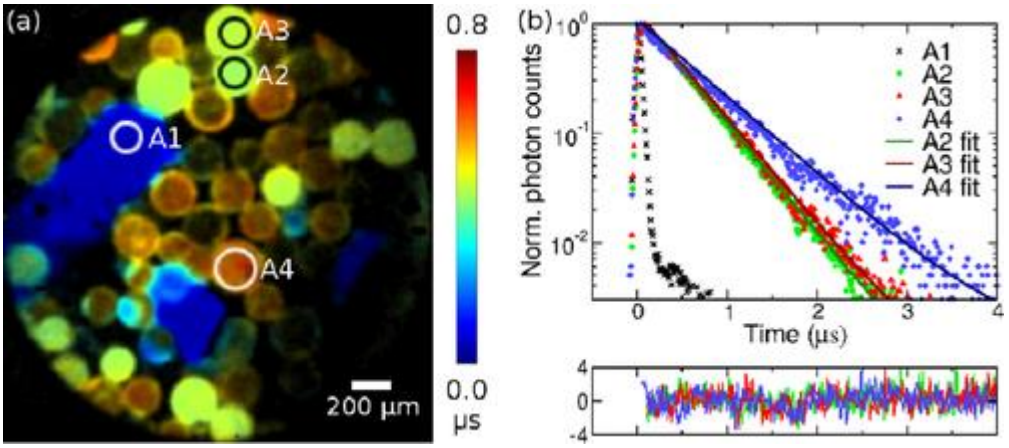


Figure 1.8: (a) PLIM of beads infused with different Ir-compounds and fluorescent plastic acquired with TimepixCam. (b) Phosphorescence decays for areas A1-A4 indicated in (a), with monoexponential fits and residuals of the fits. (Hirvonen et al., 2017)

The Timepix3 chip was a successor of the Timepix that extended the functionality by allowing detection of time-of-arrival (TOA) and time-over-threshold (TOT) at each pixel simultaneously. The chip had the same dimensions as Timepix. Recently, the next-generation camera, Tpx3Cam, has become available, based on the same silicon optical sensor as above and Timepix3 readout chip (Poikela et al., 2014). Timepix3 improves the camera's time resolution to 1.56 ns. It also has a fast readout rate of 80 Mpixel/s. The TOT and TOA of each pixel that exceed a pre-set threshold are measured and stored by the internal pixel circuitry. The pixel light detection threshold (non-intensified version) corresponds to about 600 photons, depending on the wavelength. The deadtime of individual pixels to process and store the information after they were hit is about 475 ns plus the corresponding TOT.

The camera readout is based on the SPIDR (Speedy PIxel Detector Readout) system (Visser et al., 2015) and is data-driven, so only the pixels containing the non-zero information are transferred from Timepix3 to SPIDR and read out to the outside world via a 1Gbs or 10Gbs link. The SPIDR also has an internal time-digital-converter (TDC), which is able to time-stamp incoming digital pulses with 0.26 ns precision synchronously with the Timepix3 hits. This feature

is useful to provide an external time reference and is sometimes referred to as the 'trigger' input, though it is completely independent from the Timepix3 operations. To date, Tpx3Cam has been used in applications like ion and electron imaging (Allum et al., 2021; Debrah et al., 2020; Zhao et al., 2017), photon imaging (Nomerotski, 2019; Zhukas, Millican, et al., 2021; Zhukas, Svihra, et al., 2021) and many more (D'Amen et al., 2021; Losko et al., 2021; Roberts et al., 2019).

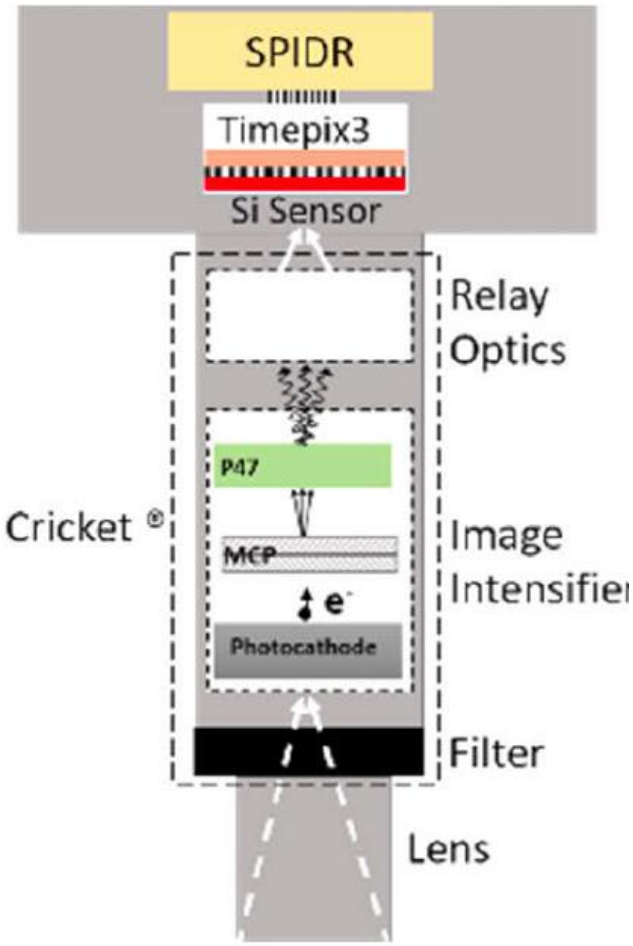


Figure 1.9: Schematic layout of the intensified Tpx3Cam camera (Sen, Hirvonen, et al., 2020).

For applications where single photon sensitivity is essential, Tpx3Cam signal was amplified with a Cricket™ (Nomerotski et al., 2023; *Photonis Cricket:*, n.d.). The system, integrated with an image intensifier, a power supply, and relay optics, projects the light flashes from the intensifier onto the optical sensor of the camera. The image intensifier is a vacuum device with a photocathode that

converts incident photons into photoelectrons. The electrons are then multiplied by an MCP and directed on to the P47 scintillating screen with a risetime of 7 ns and maximum emission at 430 nm. The screen converts these electrons into a fast flash of photons, focusing them onto the optical sensor inside Tpx3Cam and generating signals in the respective pixel front-end electronics. This is explained schematically in Figure 1.9. The camera can be further upgraded with the next-generation Timepix4 chip with 200 ps time resolution (Llopart et al., 2022).

1.7. Applications of O_2 imaging and PLIM

Quantitative monitoring of O_2 concentration and its spatial distribution is important for physiological studies with cells, tissue samples, and whole organisms, including humans (Apreleva et al., 2006; Babilas et al., 2008; Golub & Pittman, 2008; Hogan, 1999; Rumsey et al., 1988). Over the years various phosphorescent probes and phosphorescence quenching microscopy techniques have been developed for such applications

In 1987, water-soluble derivatives of porphines and fluorescein were first used for O_2-dependent phosphorescence quenching within the physiological range (Vanderkooi et al., 1987). An instrument was constructed to measure the phosphorescence lifetime. Excitation light from a xenon flash lamp was isolated with a monochromator. The emission wavelength was filtered with an emission monochromator or Schott cut-off filter and detected with the Hamamatsu photomultiplier (Wilson et al., 1987).

This methodology was restricted to *in vitro* studies of biological samples unless it was used to measure O_2 distribution in intact tissue in a noninvasive fashion (Rumsey et al., 1988). Isolated rat livers, perfused with media containing palladium coproporphyrin, were used to image phosphorescence at various perfusion rates. The phosphorescence emission was collected with a silicon-intensified target (SIT) video camera. Phosphorescence increased with the transition from a well perfused liver to anoxia. The restoration of O_2 also showed tissue reoxygenation. The spatial resolution of the video system was 70 μm per pixel, which was not sufficient to determine small differences in perfusion.

In 1992, a rather new noninvasive phosphorescence imaging method was described for measuring oxygen tension in the retina of a cat (Shonat et al.,

1992). The O_2-dependent Pd-porphyrin molecules were injected into the bloodstream and phosphorescence lifetime was measured from a series of images collected by an intensified CCD camera at different time delays after excitation with flash light. The Stern-Volmer relationship was used to convert lifetimes into O_2 concentration. But the phosphorescence images were collected for 13-20 seconds, which was rather slow, and the changes in the O_2 concentration during this period produced errors.

Similar O_2 imaging applications were also reported. Phosphorescence imaging of O_2 concentration distribution in the heart of a newborn piglet was performed by injecting a phosphorescent O_2 probe into the blood and illuminating with monochromatic light. A series of images were collected with a gated-intensified CCD camera, and 2D O_2 concentration maps were generated (Rumsey et al., 1994). The excitation light used for the experiment was at 530 nm and phosphorescence occurred at 695 nm. The method measured the O_2 distribution at the surface layer of the tissue.

The absorption bands of the phosphor, Pd-meso-tetra-(4-carboxyphenyl)-porphyrin, at wavelengths less than 540 nm, limited the O_2 measurements to the surface layer of the tissue. At these wavelengths, the absorption by the chromophores in the tissue, especially hemoglobin, myoglobin, and cytochromes, is high which limits the penetration depth of the excitation light to 1 mm or less. In contrast, the emitted phosphorescence has a maximum at 695 nm, where the absorption by the tissue chromophores is much less and it can penetrate much greater thicknesses of tissue.

Later in 1995, the synthesis of a new group of O_2-sensitive phosphors, tetra-benzoporphyrin, was reported (Vinogradov & Wilson, 1995) that showed high phosphorescence quantum yield. The absorption maximum was at 636 nm, and the phosphorescence occurred at 800 nm. The water-soluble derivative of the Pd-tetra-benzoporphyrin was used to perform non-invasive, *in vivo* mapping of O_2 distribution in the vascular system of tumour-bearing mice (Vinogradov et al., 1996). The porphyrin was injected in the tail and the tumour regions were imaged with a CCD camera. It allowed O_2 imaging through the centimeter thicknesses of the tissue. But the sensitivity of the system was low and could be improved by 10^5 times with point measurements using a light guide.

The palladium-porphyrin compound (Vanderkooi et al., 1987) was used to develop a method for intracellular O_2 measurement in intact isolated skeletal muscle using phosphorescence quenching by O_2 (Hogan, 1999). Single skeletal muscle fibers were isolated, and a Pd-porphyrin O_2 probe was injected by micropipette pressure injection. The phosphorescence quenching of the O_2-sensitive probe was imaged with an inverted microscope. Though the method produced reliable O_2 measurements, the use of the porphyrin probe may lead to problems like the consumption of O_2 by the quenching mechanism and the production of reactive O_2 species when used at high concentrations.

While O_2 measurements in static tissues were stable, the measurements in microcirculation were influenced by measurement artefacts in phosphorescence quenching microscopy. Golub and Pittman demonstrated that large excitation area and high flash rate strongly reduce O_2 in motionless tissue, but less in flowing blood due to O_2 consumption. To overcome this, they proposed a phosphorescence quenching microscopy technique with a small excitation area and low flash rate. The technique produced stable and accurate microscopic O_2 measurements in tissues and fluids (Golub & Pittman, 2008).

Real-time two-dimensional mapping of O_2 and cerebral blood flow was performed by combining PLIM with laser speckle contrast imaging (Sakadžić et al., 2008). A novel imaging instrumentation was presented, where a pulsed laser was used to excite the phosphorescence of Oxypor R2, and a thermoelectrically cooled CCD camera collected the images. It produced wide-field images of O_2 distribution and cerebral blood flow with a high signal to noise ratio but poor temporal resolution (~4 s).

Until now, the spatial and temporal resolutions of the O_2 imaging systems were comparatively low. Since 2P microscopy has a high degree of spatial confinement and a lower risk of photodamage, the combination of this technique with phosphorescence quenching allowed high-resolution imaging. This was possible with the specially designed 2P enhanced phosphorescent nanoprobe platinum porphyrin-coumarin-343 (PtP-C343) (Finikova et al., 2008). PtP-C343 belongs to a family of dendritically protected phosphorescent probes described by (Lebedev et al., 2009) where Pt porphyrin is encapsulated inside poly(arylglycine) dendrimers. This prevents the porphyrin from interacting with the measurement system. The coumarin-343 units, attached to the periphery of

the dendrimers, absorb the energy from the 2P excitation and transfer it to the porphyrin. The Pt-porphyrin undergoes intersystem crossing into its triplet state upon excitation and emits the phosphorescence, which is then quenched by O_2.

This probe was used for 2P *in vivo* imaging of mouse and rat brain (Sakadzić et al., 2010). The probe was administered by either injecting into the vasculature through the femoral artery or by pressure-injecting directly into the brain tissue. Phosphorescence was excited by gated femtosecond laser pulses and collected with a microscope. The system could resolve microvasculature structures down to the capillary level with a temporal resolution of 0.16–0.76 s per single-point O_2 measurement. However, the raster scanning of the entire vasculature stack required up to 30 min.

2P phosphorescence lifetime microscopy with the PtP-C343 probe was used by (Lecoq et al., 2011) to simultaneously measure O_2 and blood flow in rat brain with higher resolution. The probe was injected intravenously into a rat, and laser pulses were focused in the lumen of an olfactory bulb capillary. Emitted photons were collected with a photomultiplier tube, and the extracted phosphorescence lifetimes were converted into O_2 concentration using the Stern-Volmer plot. O_2 was measured with a temporal resolution of 25 µs and a lateral resolution less than 1 µm but the depth of measurement was limited to 300 µm.

Though the phosphorescence imaging techniques discussed above were noninvasive, the O_2-dependent probes were still injected into the animals. So, a new O_2 measurement technique was proposed using a planar O_2 sensor (Babilas et al., 2005). Platinum (II)–octaethyl–porphyrin was immobilized in a polystyrene matrix as a transparent film. The sensor film was attached to the cover glass and kept in direct contact with the surface of the tissue. A pulsed LED array was used to excite the sensor film, and the emission was collected with a fast gated CCD camera mounted to a microscope. The phosphorescence decay time was determined with RLD. This allowed noninvasive 2D mapping of surface O_2. Since the sensor film is applied to the tissue surface, the distance between the sensor and the site of interest requires diffusion of the O_2 molecules to the sensor. This requires more time compared to the other techniques. The fast data acquisition process provided temporal resolution in the millisecond range, which is still very low.

A new cell-penetrating phosphorescent O_2-sensitive probe, NanO2-IR, is introduced to monitor O_2 concentration in live tissues (Tsytsarev et al., 2013). It is based on polymeric nanoparticles and phosphorescent platinum (II) tetra (4-fluorophenyl) tetrabenzoporphyrin (PtBP) dye. The probe is excitable at 615 nm and emits at 760 nm. It has high brightness, photostability, and optimal response over the physiological range of O_2. The probe was topically applied to the exposed cortex. After staining for 30 min, the cortex was washed, and sealed with silicone oil and cover glass for imaging. The phosphorescence lifetime was collected with a simple CCD camera-based imaging system. The probe provided a great signal-to-noise ratio and short image acquisition times for *in vivo* applications.

Though PtP-C343 was successfully applied in 2P phosphorescence lifetime microscopy of O_2 measurements, its complex multichromophoric structures led to a few problems. Efficient energy transfer requires a small distance between the chromophores. This caused various intramolecular triplet state quenching pathways, which degraded the probe's emissivity and imaging performance. Also, the emission band of the probe at 650-700 nm limited the depth of imaging to 300 µm. Recently a new 2P O_2 probe, Oxyphor 2P, was proposed with a high 2P absorption cross-section and high phosphorescence quantum yield (Esipova et al., 2019).

Oxyphor 2P is an antenna free probe that uses platinum tetraarylphthalimidoporphyrins (PtTAPIP) as a single chromophore. The carbonyl groups of PtTAPIP are locked in a plane with the porphyrin, which ensures a high degree of conjugation and stabilization. The 2P absorption maximum of Oxyphor 2P is shifted to 960 nm. The second absorption peak is at 1140 nm which may be useful for multiplexed excitation of Oxyphor 2P. The brightness of the sensor exceeds PtP-C343 by ~ 60-fold. Also, since the emission of Oxyphor 2P is at 758 nm, this increases the depth of imaging in tissue to 600 µm. It has been used to measure O_2 changes in arteries and veins in the cerebral cortex of the brain in breathing and sedated mice. Although this sensor allows faster imaging, 2P lifetime imaging is limited by its grid-like pattern instead of pixel-to-pixel imaging. So, the combination of the probe with multifocal two photon lifetime imaging, where different focal planes within the sample are imaged simultaneously with a gated intensifier and a CCD camera, will increase

the image acquisition speed without decreasing the temporal resolution. The multifocal points can be generated by using a cascade of beam splitters, or beam splitter connected with multiple mirrors.

Several other phosphorescent probes, including cell-permeable or impermeable, small molecule, supramolecular dendrimers, nano- or micro-particulate structures, as well as planar solid-state O_2 sensors have been synthesized over years for phosphorescence O_2 sensing (Dmitriev et al., 2014; Papkovsky & Dmitriev, 2018; Tsytsarev et al., 2017; X. D. Wang & Wolfbeis, 2014). Various phosphorescence quenching microscopy techniques have also been developed for accurate and quantitative measurement of O_2 concentrations in biomedical applications (Devor et al., 2012; Dmitriev & Papkovsky, 2018; Papkovsky & Dmitriev, 2013; X. D. Wang & Wolfbeis, 2014). A summary of O_2 imaging applications has been listed in Table 1.4.

1.8. Conclusion

This chapter outlines the importance of measurements of tissue O_2 and the available phosphorescent O_2 sensitive materials and detection modalities used for O_2 mapping. PLIM is a minimally invasive technique that allows accurate and quantitative O_2 mapping. But the current PLIM systems have limitations with respect to the penetration depth, speed, and sensitivity of the imaging, image acquisition time, etc. While in TCSPC PLIM microscopy is mostly slow due to raster scanning, camera-based imaging systems are comparatively faster but based on intensity detection. As a result, the O_2 measurements are influenced by factors like photobleaching, optical interferences, and measurement geometry. Moreover, most of the imaging systems are microscopic, and macroscopic systems are still rare. Therefore, there is a need for the development of new macroscopic PLIM imaging techniques for accurate and quantitative O_2 readout.

The new Tpx3Cam based on the silicon sensor and the new generation Timepix3 chip performs time resolved imaging. It is single photon sensitive and can detect the TOA and TOT at each pixel simultaneously with a time resolution of 1.6 ns and read out rate of 80 megapixels per second. The camera when

Table 1.4: Summary of O_2 imaging applications

Aim	**Probe**	**Excitation**	**Detection**	**Reference**
Measurement of O_2 concentration.	Derivatives of porphines and fluorescein	Xenon lamp	Hamamatsu photomultiplier	(Vanderkooi et al., 1987)
Measuring O_2 Distribution in Perfused Tissue	Pd-coproporphyrin	Xenon arc lamp	Silicon intensified target (SIT) video camera	(Rumsey et al., 1988)
O_2 distribution in retina	Pd-porphyrin	Xenon lamp	Microscope with intensified CCD	(Shonat et al., 1992)
O_2 distribution in heart	Pd-meso-tetra-(4-carboxyphenyl)-porphyrin	Xenon lamp	Microscope with intensified CCD	(Rumsey et al., 1994)
Non-invasive *in vivo* O_2 imaging	Pd-tetra-benzoporphyrin	Flash lamp	Intensified CCD camera	(Vinogradov et al., 1996)
O_2 in skeletal muscle fiber	Pd-porphyrin	Flash lamp	PMT	(Hogan, 1999)
O_2 in retina of mouse eye	Oxyphor G2	LED	CCD	(Wilson, Vinogradov, Grosul, Kuroki, et al., 2005)
O_2 imaging with planar sensor	Pt-OEP	LED array	CCD	(Babilas et al., 2005)
Realtime mapping of O_2	Oxypor R2	Laser	CCD	(Sakadžić et al., 2008)
O_2 in cerebral vasculature and tissue	PtP-C343	Ti:Sapphire laser	PMT	(Sakadzić et al., 2010)
Simultaneous 2P imaging of O_2 and blood flow	PtP-C343	Ti:Sapphire laser	PMT	(Lecoq et al., 2011)
In vivo imaging of brain	PtBP	Laser	CCD	(Tsytsarev et al., 2013)
Planar implantable sensor for O_2 imaging	PtBP	Laser	CCD	(Tsytsarev et al., 2017)
Deep tissue O_2 imaging	Oxyphor 2P	Laser	PMT	(Esipova et al., 2019)

coupled to a photon counting image intensifier and inverted microscope produced PLIM of polystyrene beads in microscopic format.

The aim of this thesis is to construct a new fast optical imager based on the Tpx3Cam for PLIM applications. The first objective was to integrate the camera with an image intensifier and other optical components and demonstrate its operation in macroscopic wide-filed PLIM mode. The performance and resolution of the imager was optimised with different image processing techniques. The next goal was to apply the imager to characterize different phosphorescent O_2 sensitive materials. For this, various commercial and non-commercial phosphorescent solid-state materials were imaged with the new imager and the accuracy of the lifetime measurements were analysed and compared with alternative O_2 measurement and imaging systems. The next objective was to apply the imager for O_2 mapping in various *ex vivo* tissue models. For this, live tissue samples isolated from animals were stained with O_2 sensitive probe and imaged to demonstrate the performance of the imager. Lastly, the aim was to determine the suitability of the imager for *in vivo* research with live animals and human disease models. To demonstrate its performance, the imager was used in a minimally invasive technique to map tissue oxygenation in developing grafted tumours.

2. Chapter 2: Materials and Methods

2.1. Materials

Polystyrene (PS), poly(methyl methacrylate) (PMMA), polyvinyl chloride (PVC) and poly(vinylidene chloride) (PVDC) polymers were purchased from Sigma-Aldrich, hydrogel D4 was from Degussa. Dulbecco's modified Eagle medium (DMEM), foetal bovine serum (FBS), paraformaldehyde (PFA), low melting point agarose, and all other chemicals were from Millipore-Sigma (Burlington, MA, USA). DMEM and McCoy's 5A media, antimycin A (AntA, complex III inhibitor), NaN3 (complex IV inhibitor) were from Millipore-Sigma (Burlington, MA). CellTiter-Glo ATP Assay kit was from Promega (Madison, WI). Plasticware was from Sarstedt (Ireland) and Greiner Bio One (Frickenhausen). Pt(II)-benzoporphyrin (PtBP) and Pt(II)octaethylporphine-ketone (PtOEPK) dyes were kindly provided by Agilent Inc (Cork, Ireland). The commercial O_2 sensors were from Mocon (Optech® Platinum stickers) (*MOCON*, n.d.) and Pyroscience (*Pyroscience*, n.d.). Platinum octaethylporphyrin (PtOEP) and OEP-ketone (OEPK) dyes were from Frontier Scientific. PtOEP-SB dye was synthesized at the Institute of Biomedical Chemistry, Moscow, according to the published method (Erzina et al., 2019; Zhdanov et al., 2022).

2.2. Methods

2.2.1. Preparation of Sensors

The solid-state phosphorescent sensor coatings were prepared from the corresponding liquid 'cocktails' containing 0.25 mg/ml of PtBP (unless otherwise stated) and 5% w/w of the corresponding polymer dissolved in tetrahydrofuran (THF). A P10 Gilson pipette was used to spot 1 µl aliquots of these cocktails onto pieces of 70 µm polyester film (Mylar®, Du Pont) or PVDF membrane, pore size 0.45 µm (Millipore), and allowed to dry overnight in

ambient air. Thus, 2-3 mm spots and patterns of the different phosphorescent materials were produced. The LDPE and PLA based PtBP sensors (Kelly et al., 2020) and PtOEPK-PS sensors spotted on microporous PVDF membrane and filter paper (Papkovsky et al., 2002; Smiddy et al., 2002) were prepared similarly as described. To produce a decreasing concentration of PtBP, standard cocktails were diluted with a 5% solution of pure polymer in THF and spotted in a similar manner. The sensor coatings were also applied on Mylar polyester films (Du Pont), which were mainly used for characterization. Sensors based on PtOEP, PtOEP/OEPK and PtOEP-SB were prepared similarly as described (Sen et al., 2022).

The PtBP based nanoparticle O_2 probe, NanO2-IR, was synthesized as described in (Fercher et al., 2011; Tsytsarev et al., 2013). Its working concentration (1 mg/mL) was prepared by diluting the stock of NanO2-IR (10 mg/mL in H_2O) with DMEM or McCoy's 5A media supplemented with 10 mM glucose, 2 mM L-glutamine and 10 mM HEPES (pH = 7.2), immediately prior to use.

McCoy's 5A media supplemented with 10% foetal bovine albumin (FBS), 2 mM L-glutamine, 100 U/ml penicillin/100 g/ml streptomycin (P/S), and 10 mM HEPES (pH 7.2) were used to maintain HCT116 cells. HEK293a cells were maintained in DMEM supplemented with 10% FBS, P/S and 10 mM HEPES (complete McCoy and DMEM), both in humidified 5% CO_2 / 95% air, at 37^{o}C.

Probe toxicity testing was performed by seeding cells on standard 96-well plates pre-coated with collagen IV at 2.5×10^4 cells/well, grown for 24 h, then exposed to NanO2-IR at 1 mg/ml in complete DMEM for different time periods. Following that, the total cellular ATP levels were measured using the CellTiter-Glo® Kit, white 96-well plates (Greiner Bio One) and Victor 2 reader (PerkinElmer) under luminometry settings (Zhdanov et al., 2012).

HCT116 cells were trypsinized, washed with DMEM, counted, and then placed into 0.5 ml qPCR tubes at a density of 0 to $5x10^6$ cells per tube for the oxygenation studies. The cells were then gently centrifuged at 200 g to precipitate them to the bottom of the tubes. The old media was aspirated, and fresh complete DMEM with 1 mg/ml NanO2-IR was added to each tube. The cells were then re-suspended and precipitated as before. Tubes containing cells were imaged after 30 min of incubation at 37^{o}C.

2.2.2. Preparation, staining and treatment of *ex vivo* animal tissue

All animal procedures were performed under authorizations issued by the Health Products Regulatory Authority (HPRA, Ireland), in accordance with the European Communities Council Directive (2010/63/EU) and approved by the Animal Experimentation Ethics Committee of the University College Cork. Fresh tissue samples were isolated from four-week-old female mice (Envigo, UK).

On the day of the experiment, mice were euthanized by decapitation and immediately dissected to extract their whole brain, lungs, fragments of small intestine and colon (large intestine), tail and front paws. These samples (8 - 10 mm in size) were immediately submerged in DMEM media equilibrated at 37°C. The excised tissues samples were cleaned in PBS and placed back into 2 ml DMEM at 37^{o}C. Then the brain tissue was dissected into cortical tissue slices (10x10 mm, 1 mm thick). After excision, the entire preparation procedure took <15 minutes.

For surface staining, the brain, lung, and cortical tissue slices were placed in mini-dishes, with 2 ml of DMEM containing 1 mg/ml NanO2-IR, and incubated for 30 min at 37^{o}C. The serosal surface side of the intestines (1 mg/ml probe, 15 min) was stained using the similar protocol. For intraluminal intestine staining, the excess of DMEM was wiped away with filter paper and then, 1 µl of DMEM containing 1 mg/ml of NanO2-IR was injected into the lumen with a Hamilton syringe, and the samples were incubated in Petri dishes for 15 min - 4 h. For the intra-tissue injection, pieces of mouse tail or paws were pre-incubated for 30 min at 37^{o}C, then injected with 5 µl aliquots of DMEM containing 1 mg/ml NanO2-IR using a Hamilton syringe and imaged after 15 min incubation.

For the imaging, samples were placed on a clean and dry Petri dish and any liquid was removed with a filter paper. Except for intra-tissue injection, each staining method was repeated three times on three different sets of samples on different days. All the experiments were completed within 2 h from excision of tissue samples.

After the imaging, stained tissue samples were transferred to Petri dishes with DMEM containing 10 µM AntA and 0.1% NaN_3 and incubated for 15 min at 37ºC to inhibit cell respiration and then imaged again. These imaging experiments were carried out within one hour from the start of staining.

2.2.3. Induction of tumours stained with phosphorescent probe in mice

Murine colorectal carcinoma CT26 cells (the American Collections of Cell Cultures) were maintained in high glucose DMEM supplemented with 10% FBS, 2 mM L-glutamine, 100 U/ml penicillin /100 µg/ml streptomycin, and 10 mM HEPES, pH 7.2 (complete DMEM), in a humidified atmosphere of 95% air and 5% CO_2 at 37°C.

For staining, $8x10^5$ cells were sown into the wells of a 6-well plate (Sarstedt, Ireland) and allowed to grow for 24 hours in complete DMEM. Cells were then washed with serum-free DMEM and incubated for 18–20 hours with various concentrations of NanO2-IR in serum-free DMEM. Cells were then washed sequentially with serum-free DMEM, complete DMEM and PBS, trypsinised, transferred into serum-free DMEM and prepared for injection in animals.

Total ATP levels in CT26 cells were measured as a viability reporter using the CellTiter-Glo® assay kit (Promega), according to the manufacturer's instructions. In short, the cells were first incubated with different concentrations of NanO2-IR (in 100 µl of FBS-free DMEM) for 18 h in a CO_2 incubator and then lysed with 100 µl of CellTiterGlo® reagent. After intensive shaking for 2 min at 37°C, the samples (200 µl) were incubated for 4 min, transferred into wells of white 96-well plates (Greiner Bio One) and analysed on a Victor 2 plate reader under standard luminescence settings.

All animal procedures were carried out in accordance with the HPRA national ethical standards and were authorized under project number AE19130/I285. Throughout the experiment, the health of every mouse was checked daily. Mice were humanely euthanized by cervical dislocation after tumours reached the size of 1.5×1.5 cm in diameter.

Mice were kept in a conventional animal unit at constant room temperature (22˚C) with natural day/night light cycle. Standard laboratory food and water were provided ad libitum. The mice were given an adjustment time of at least

seven days prior to the experiments. The experiments were performed on 6-8 weeks old, healthy, female Balb/C (CT26 models, Envigo, UK) mice that weighed between 16-22 g. For routine tumour induction, 200 µl of serum-free culture media containing a minimum tumourigenic dosage of cells ($1x10^5$ non-stained CT26 cells or a mixture of $1x10^5$ non-stained and $1x10^5$ stained with NanO2-IR cells, unless otherwise stated) was injected into the right flank. Tumours were allowed to grow and were monitored daily. The formula used to measure and calculate tumour volume is $V = (L \times W^2)/2$, where L is the tumour's longest diameter (length), and W is the longest diameter (width) perpendicular to diameter L.

For the measurement of NanO2-IR distribution in tissue, tumours were removed after post-mortem animal imaging and fixed in 4% paraformaldehyde in PBS for 30 min at room temperature. The samples were then washed in PBS, embedded in low melting point agarose (4% in PBS), and sectioned on a Leica VT1000s vibratome (Leica Biosystems, Wetzlar, Germany) to produce slices that were about ~500 µm thick. The phosphorescence lifetime signals were recorded in air-saturated conditions, and after chemical deoxygenation with the addition of 5 mg/ml Na_2SO_3 and 5 mg/ml K_2HPO_4.

2.3. Imaging on Tpx3Cam

2.3.1. Design of µs PLIM macro imager

The Tpx3Cam camera (Amsterdam Scientific Instruments) was coupled via a C-mount connector to the Cricket adaptor (Photonis) which housed an image intensifier with a fast decay P47 phosphor (Photonis) and a 25 mm 760±50 nm or 648±50 nm emission filter (Edmund Optics). The other side of the Cricket adaptor was connected to the Navitar NMV-50M11" 50 mm lens by another C-mount connector. A super-bright 5 mm LED with a central wavelength of 627 nm (12,000 mcd, 8° angle, Parts Express) or 390 nm LED (40 mW, 5 mm, Parts Express) was used to excite the sample. The optical and electronic components of the setup are shown in Figure 2.1.



Figure 2.1: Components used to build the new wide-field Tpx3Cam imager. (a) Tpx3Cam coupled to Cricket, filter and lens; (b) Cricket adapter; (c) Lens; (d) C-mount and ring connectors, (d) LED; Imager setup covered in black box; Electronic connections of pulse generators, oscilloscope and power supply; (d) PC for collection of raw data.

The Photonis PP0360EF intensifier has an S25 photocathode with an 18 mm diameter, 8% quantum efficiency at 780 nm, and a 40 kHz total dark count rate at room temperature. The intensifier was connected to a standard power supply (Thundar, 72-10495) with one channel providing the power and the other regulating the intensifier gain. Synchronized pulses were sent to the camera and the LED with two channels of a fast pulse generator (Tenma, TGP110). As illustrated in Figure 2.2, the synchronization pulse was preceding the LED pulse by 10 μs. The Tpx3Cam imager was primarily used in the upright orientation. The samples were placed on a Thorlabs stage, which allowed for X, Y, and Z axis movement and focusing. For the best focus, the distance to the object was about 8 cm. The system was protected from ambient light by a 525x375x300 mm black box (Thorlabs, XE25C9/M), which reduced the unwanted background noise. The imager can be rotated to image samples either from the top or from the side.

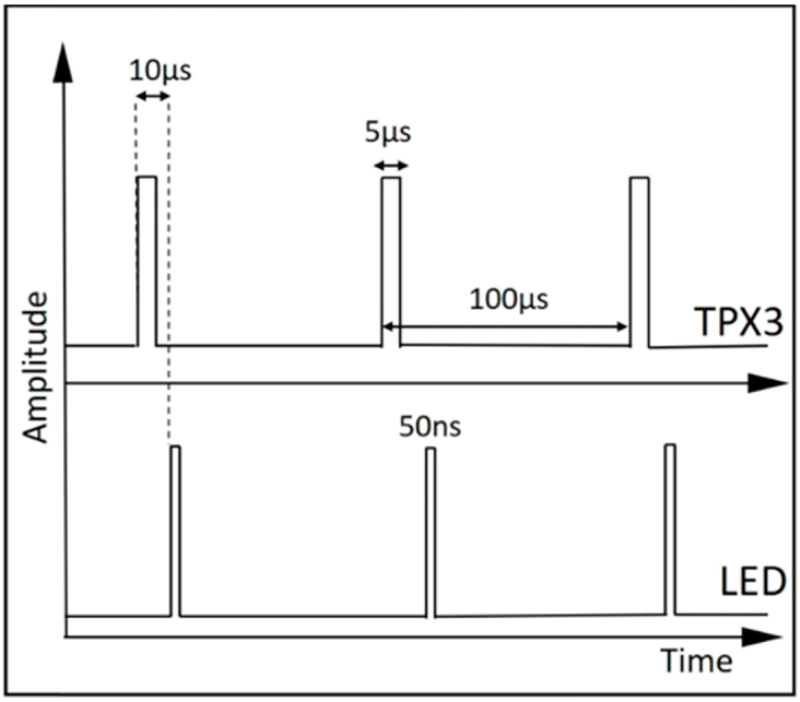


Figure 2.2: Pulsing scheme of the imager. The LED is pulsed every 100 µs with 50 ns duration of the pulse. Tpx3Cam is provided with a synchronous pulse 10 µs before the LED, which is time-stamped and included into the data stream. The camera records the photon hits for 100 µs until the next LED pulse (Sen, Hirvonen, et al., 2020).

2.3.2. Image acquisition and data analysis

The operational parameters, focusing, and alignment were adjusted online using the SophyTM software provided by Amsterdam Scientific Instruments. The Tpx3Cam raw data was collected in binary format, and post-processed using a custom-designed software. The post-processing algorithm time-orders the hit pixels and trigger signals, and provides output in ASCII format listing the parameters for each hit pixel: excitation trigger time, pixel X and Y coordinates, TOA (time of arrival = pixel time since start of experiment), TOT (time over threshold = amplitude), and (TOA - trigger time) = pixel time since the beginning of the current excitation period.

A dedicated program written in C-language by Liisa M. Hirvonen (https://github.com/lmhirvonen/timepix3cam) was used to analyse the post-processed data. All hit pixels were added to the final image to create sum images. Clusters of hit pixels between 3 and 15 pixels in size were found for each excitation period in centroided images, and the centroid pixel of each cluster was

calculated from the TOT using centre-of-mass centroiding (unless otherwise stated). This centroided position was noted for each cluster in the centroided image. All photons were then placed into an XYt data cube, and the data was written into an .ics image file to generate the lifetime images. Tri2 software was used to fit the phosphorescence decay in each individual pixel of the image using a two-exponential function $I(t) = A_1\exp(-t/\tau_1) + A_2\exp(-t/\tau_2)$. The average lifetime $\tau = (\alpha_1\tau_1^2+\alpha_2\tau_2^2)/(\alpha_1\tau_1+\alpha_2\tau_2)$ obtained from this fit was encoded in a pseudocolor scale (blue for short lifetimes and red for long lifetimes) to generate phosphorescence lifetime image. A phosphorescence intensity image was obtained by summing all photons together. Software like ImageJ, Adobe Photoshop, and Illustrator were used to assemble the figures together.

2.3.3. Statistics

For the statistical analysis of the sensor images, mean values ± standard deviation (S.D.) for the selected regions of interest (ROIs) were calculated. Line profiles were also plotted and analyzed. ImageJ (Schneider et al., 2012) software was used to analyse the imaging data for cell and tissue samples. The R (v3.6.3) and Rstudio (v1.2.5033) software were used to perform a statistical analysis of lifetime values obtained from whole PLIM images and derived O_2 values. According to the calibration equation for NanO2-IR, lifetime values between 19-45 µs were examined (see Results). The tools ggplot2 and patchwork were used to produce the figures. Based on experimental treatment, measurements were aggregated, and the Mann-Whitney U test was used to assess statistical differences (W- and p-values were produced). Differences in the modes (Δ-mode, µs) was deemed the most acceptable metric to represent differences between treatments due to the non-normal nature of the data and their unimodal distribution in all groups. The distribution of the data set was shown using: 1) the box plot, which shows the median and interquartile range for each batch of observations; 2) the violin plot, which shows the relative density of all observations in a data set and its wideness; and 3) the semi-transparent density plot that shows the total relative density of all observations of the same type; 4) BoxPlotR was used to generate 'boxes-and-whiskers' graphs of the intensity and lifetime variability (http://shiny.chemgrid.org/boxplotr/). Variability of the

intensity signals and lifetime values was assessed using the common average deviation equation, *AveDev=1/n Σx-(x/v)*. For that, all data points along three typical lines in the brain samples were normalized to the average values, which were set as 1 a.u. For *in vivo* imaging of the O_2 levels in grafted tumours, repeated measures ANOVA test was performed on the lifetime values recorded on the different days of the experiments.

2.4. Imaging on confocal PLIM microscope

The solid-state sensor film and the NanO2-IR probe were examined on the confocal FLIM/PLIM microscope system (Becker&Hickl, Germany), based on an upright Axio Examiner Z1 microscope with a 5x air objective and stage with motorized Z-axis control. The DCS-120 confocal scanner (B&H), a picosecond 405 nm laser (B&H) and an R10467U-40 photon counting detector (Hamamatsu Photonics) were used to detect the emission. MicroToolBox software (Carl Zeiss) was used to control the microscope, and SPCImage software (B&H) - for image acquisition and processing (Dmitriev et al., 2013).

The sensor film was imaged at 21 kPa O_2 and room temperature. The live cells were imaged at 37°C for using a 20x/1.0 W-Plan Apochromat dipping objective and the tissue slices were imaged at 22°C using a 5x/0.25 FLUAR objective. The lifetime values were calculated from the PLIM data using SPCImage software, version 8.4 (B&H). Microsoft Excel was used to export numerical figures for lifetime distribution histograms and PLIM colour images.

2.5. Calibration of sensor materials

A sensor film or liquid NanO2-IR probe in DMEM was placed in a 20 mL transparent polystyrene vial, which was sequentially flushed with O_2-N_2 gas mixtures of known composition produced by a precision gas mixer (Champagne, Switzerland), while being submerged in a water bath set at 37 °C (Julabo, Germany). The O_2 concentration was gradually increased from 0% to 21% O_2 (equivalent to 0-210 μM dissolved O_2). A portable reader Optech® (Mocon) (*MOCON*, n.d.) was used to measure sensor lifetime signal. Lifetime readings

were obtained at least five times to ensure stable and reliable lifetime results after 20-min equilibration of O_2 concentration and temperature in the sample. Lifetime values were plotted and analyzed at various O_2 concentrations.

3. Chapter 3: Design and Characterisation of the new Tpx3Cam based PLIM/FLIM macro-imager

FLIM based probes and detection modes are actively used in applications like biomedicine, material science, chemistry, cell biology, etc (Becker, 2012; Korczyński & Włodarczyk, 2009; Marcu, 2012). Being independent of the fluorophore concentration, photobleaching, fluctuations in excitation intensity, detector sensitivity, optical properties of the sample and measurement geometry, it has internal referencing capabilities and allows quantitative, accurate and calibration-free measurements of key biochemical and environmental parameters, such as pH, Ca^{2+}, glucose dynamics, etc (Agronskaia et al., 2004; Lakowicz, Szmacinski, Nowaczyk, & Johnson, 1992; Orte et al., 2013; Veetil et al., 2012; Zheng et al., 2018). While FLIM measures nanosecond lifetimes of short-lived fluorophores, PLIM (Chelushkin & Tunik, 2019) measures longer lifetimes in the µs-ms range.

PLIM based detection is particularly advantageous for quenched-phosphorescent sensing and imaging of O_2 in various chemical and biological samples. With the development of the novel phosphorescence-based materials and applications, interest in PLIM has risen significantly in recent years (Banerjee et al., 2015; Banerjee, Arzhakova, et al., 2016; Papkovsky, 2004; Tsytsarev et al., 2017). It is frequently used in biology to assess oxygenation and O_2 consumption in living tissue samples (Dmitriev & Papkovsky, 2012; Fercher et al., 2011; Jenkins et al., 2015; Zhdanov et al., 2017). Traditional detection techniques like confocal Time Correlated Single Photon Counting (TCSPC) and wide-field PLIM using fast gated CCD/CMOS cameras are either slow due to long pixel dwell times or are less accurate and sensitive (Becker, 2012, 2018; Hirvonen et al., 2014, 2015; Hirvonen & Suhling, 2017; Petrášek & Suhling, 2010; Phillips & Christensen, 1985; Sparks et al., 2017; Wei et al., 2017). Moreover, PLIM is rarely used for macroscopic applications. Macroscopic luminescence imaging is in demand in biomedical and life sciences, where intensity-based imagers currently dominate (Zarychta-Wiśniewska et al., 2017), but they lack accuracy and quantitative optical readout.

Therefore, in this chapter we construct and investigate the properties of a new fast optical imager Tpx3Cam for macroscopic widefield PLIM applications. It was characterized using a planar phosphorescent O_2 sensor and a resolution plate mask. Several acquisition and image processing algorithms were also evaluated to optimize system resolution and performance.

3.1. Design and Characterization of imager

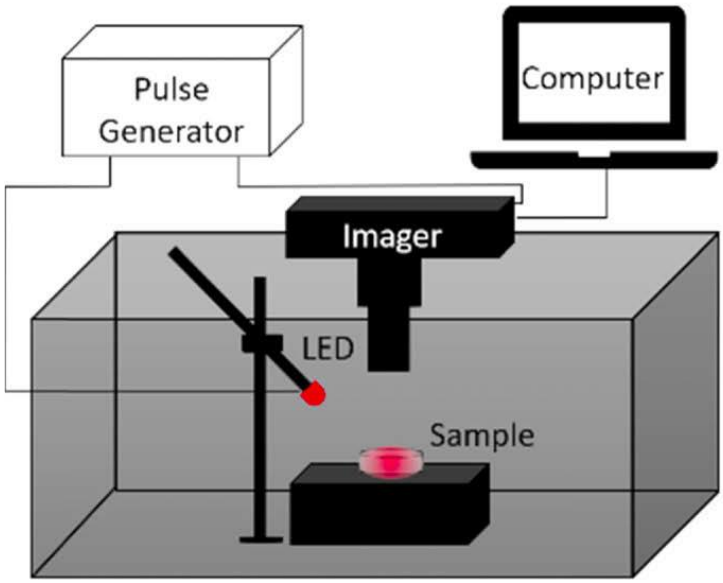


Figure 3.1: Experimental setup of the PLIM macro-imager based on Tpx3Cam (Sen, Hirvonen, et al., 2020).

The experimental set-up of the Tpx3Cam imager is shown in Figure 3.1. The Cricket is a plug-and-play electro-optical adapter that holds and aligns the important optoelectronic components of the PLIM system, improving the quality of intensified images and allowing flexibility so that it may be rotated 360 degrees and adjusted geometrically for analysis of different samples. The spatial resolution of the camera was determined with a USAF resolution test target (Thorlabs) (Figure 3.2a). A planar phosphorescent O_2-sensor, which comprised of a 15 μm thick solid-state coating comprising 1% w/w of PtBP dye (Luxcel Biosciences) in RL-100 polymer (Degussa), deposited on an 80 μm thick polyester film (Mylar, DuPont) by spin-coating method (Tsytsarev et al., 2017), was used to characterize the imager.

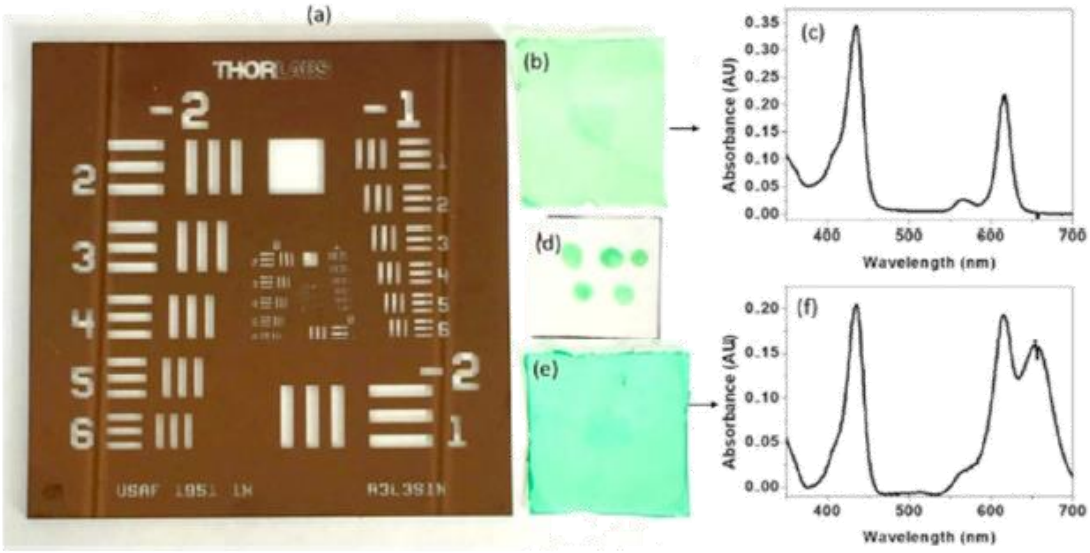


Figure 3.2: Samples used to characterize the imager: (a) USAF resolution test target; (b) Planar PtBP-RL100 based O_2 sensor film and (c) its absorption spectrum; (d) PtBP-RL100 sensor spots on PVDF membrane, (e) Sensor film with PtBP and aza-Bodipy dyes in RL100, and (f) its absorption spectrum. Spectra were measured on an 8453UV-Visible spectrophotometer (Agilent). Adapted from (Sen, Hirvonen, et al., 2020).

The photograph and UV-Vis absorption spectrum of the sensor are shown in Figure 3.2b, c. 7-10 mm sized sensor dots (Figure 3.2d) were produced by spotting the same sensor cocktail on a microporous PVDF membrane (Millipore). The instrument response function was measured using another planar sensor containing PtBP and an additional aza-Bodipy dye (4,4-difluoro-1,3,5,7-tetraphenyl-4-bora-3a,4a, 8-triaza-s-indacene) with excitation maximum at 650 nm (Figure 3.2e, f) and fluorescence at around 672 nm (Jokic et al., 2012; Lu et al., 2014).

3.1.1. Single photon events

Figure 3.3 shows the images of single photon events observed with the Tpx3Cam. They were approximately round, with a typical diameter of ~3 pixels. As expected, the pixels have higher TOT in the center of the event (Figure 3.3a). Figure 3.3b shows the time stamps for photons arriving at random times, where the events are clearly distinguished by their arrival time. However, the events themselves have a time distribution, where the center of the photon event with the highest flux has the earliest time stamp, and the time stamps of the surrounding pixels are delayed (Figure 3.3c-e). This effect, known as “timewalk”

effect, is due to the lower flux in the surrounding pixels as the corresponding pulses have a slower rise time and, therefore, cross the threshold slightly later (Tsigaridas et al., 2019; Zhao et al., 2017). As each cluster represents a single photon which has only one arrival time, we have tested the effect of centroiding on the spatial and temporal resolution.

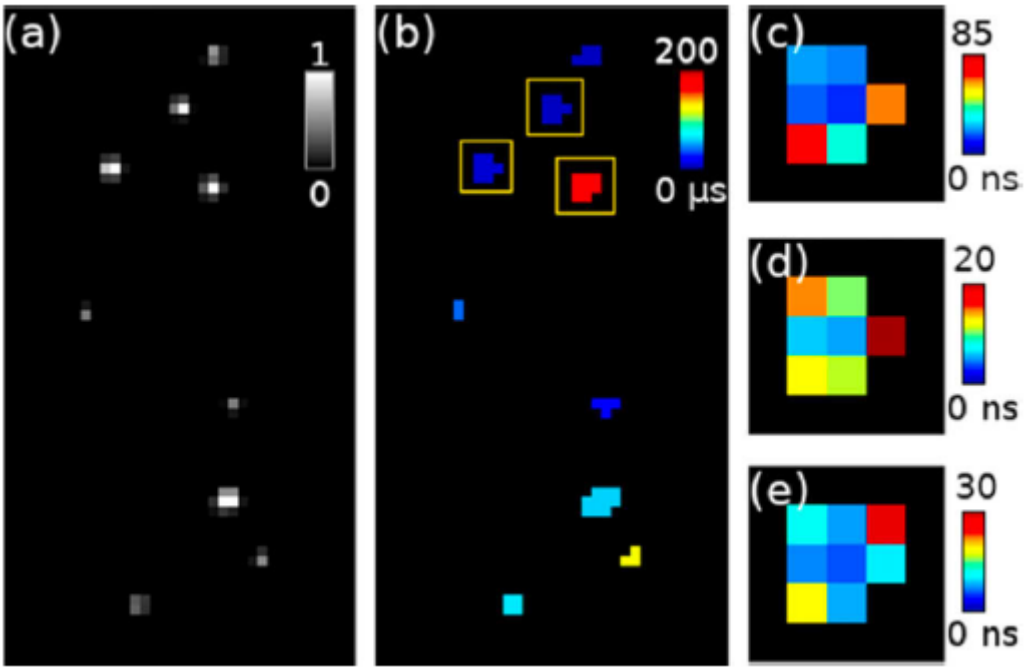


Figure 3.3: Single photon events detected with the Tpx3Cam setup. (a) TOT, i.e., intensity, (b) arrival time, (c-e) Re-scaled arrival time for individual photon events showing the "timewalk" effect (Sen, Hirvonen, et al., 2020).

3.1.2. Spatial resolution and centroiding methods

To measure the spatial resolution of the PLIM system, the 1951 USAF resolution test target (Figure 3.2a) was placed on top of the planar O_2 sensor foil (Figure 3.2b) and imaged with Tpx3Cam. The 627 nm LED was set at 8 V power and 500 ns pulse width to excite the sample (Figure 3.4a). Data was collected for 60 seconds with the 760 ± 50 nm filter. A total of 612,072 "frames" (excitation periods) with 131 million triggered pixels were acquired at a pixel readout rate of 2.2 MHz. In this data, 26 million photon events were found in the size range of 3-15 pixels, with 2.4 million undersize (<3 pixels) and 1.9 million oversize (>15 pixels) events discarded. This corresponds to accepted photon event count rate of ~0.43 MHz.

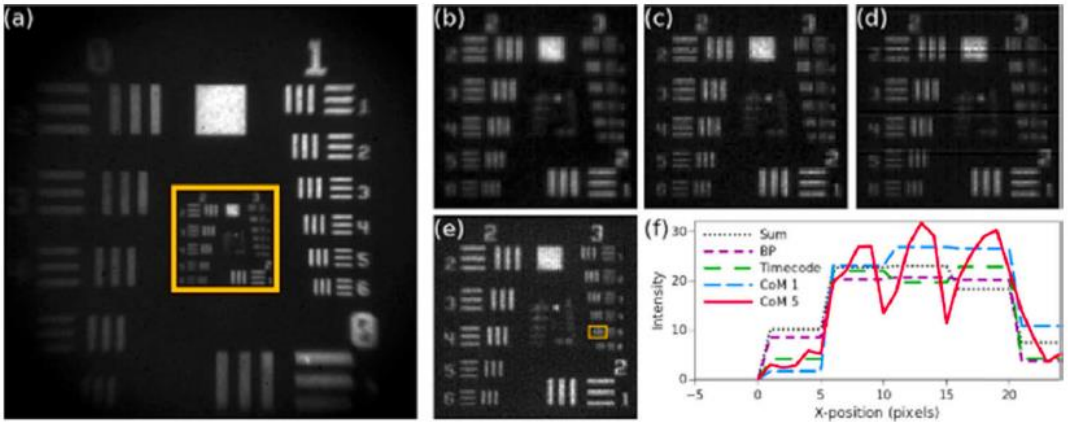


Figure 3.4: Images of 1951 USAF resolution test target overlaid on top of a phosphorescent O_2 sensor foil. (a) Sum image showing the PLIM imager field of view. (b-e) images of the area indicated in (a) centroided with different methods: (b) sum, (c) brightest pixel (BP), (d) earliest timecode, (e) center-of-mass with 1/5-pixel accuracy (CoM 5). (f) Cross-sections of the bars in the area indicated in (e), where the sub-pixel centroiding can still resolve lines with ~40 µm spacing, that cannot be resolved with the other centroiding methods (Sen, Hirvonen, et al., 2020).

The data was processed with different centroiding methods to compare their effect on the spatial resolution. Figure 3.4a shows the whole 17.7 x 17.7 mm field of view (FoV) of the PLIM macro imager system. A noticeable gradient in the intensity is due to the non-uniformity of the illumination system made of a single LED. Figure 3.4b-e show the central area of the FoV processed with different centroiding methods. As expected, the sum image (Figure 3.4b), where all hit pixels are summed for the final image, shows worst resolution, since the photon events cover a large area and smear the image. Brightest pixel centroiding (Figure 3.4c) and timecode centroiding (Figure 3.4d), where the photon event center is assigned to the pixel with highest TOT or the earliest timecode, respectively, provided some improvement of resolution. Best resolution was achieved with sub-pixel centroiding (Figure 3.4e). Here each pixel is divided into sub-pixels (5x5 sub-pixels) and the photon coordinates are found by centre-of-mass calculation using the TOT information. Figure 3.4f shows cross-sections of bars indicated in Figure 3.4e, where the bars are easily resolved with the sub-pixel centroiding method but cannot be resolved in the other images. This centroiding technique provided a resolving power of 12.7 lp/mm with line width 39.4 µm.

3.1.3. Instrument response

To measure the instrument response function (IRF), the sensing film, which contained a short-lived aza-Bodipy dye, was imaged with the Tpx3Cam imager. This dye is excitable with the same red LED (Figure 3.2f) as used for all measurements here showing fluorescence at 650 nm with lifetime in the low ns range (Jokic et al., 2012). The LED bias voltage was set to 4 V and the pulse duration to 50 ns, a minimum providing stable lifetime signal in Tpx3Cam.

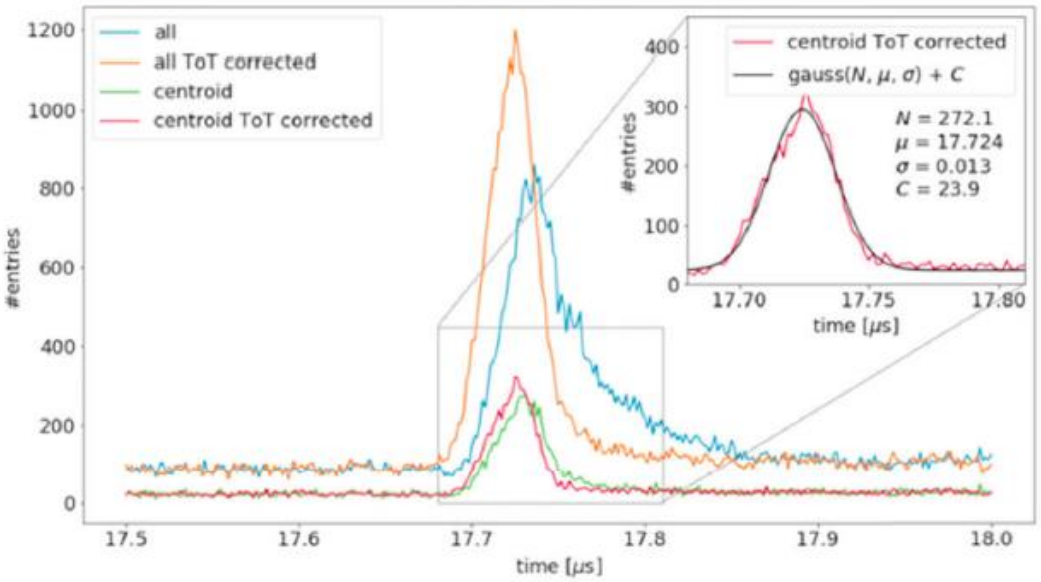


Figure 3.5: Instrument Response Function (IRF) position in the measurement time interval is shown for all hit pixels and for the centroided pixels. In both cases the distributions are shown before and after the TOT correction. Gaussian fit of the centroided and TOT corrected distribution corresponds to the IRF FWHM of 30.6 ns. Background was described with a constant in the fit (Sen, Hirvonen, et al., 2020).

Figure 3.5 shows several distributions of the photon arrival time with respect to the synchronous pulse received by the camera. Variation of this time provides information about the IRF. The time distributions for all hit pixels and for the centroided pixels are shown before and after the TOT correction. For the most inclusive measurement, all hit pixels were included, whereas for the centroided data only the earliest timecode for each photon hit was included, which explains different population of the histograms. The Gaussian fit of the centroided, TOT corrected distribution has FWHM of 30.6 ns. The background was accounted for as a constant in the fit.

As expected, the centroiding significantly improves the temporal resolution of the Tpx3Cam imager by effectively selecting pixels with higher TOT which

substantially reduces the timewalk effect. To account for the timewalk and to further improve the time resolution we apply the TOT correction by shifting the pixel TOA by an amount determined through a special calibration procedure (Tsigaridas et al., 2019).

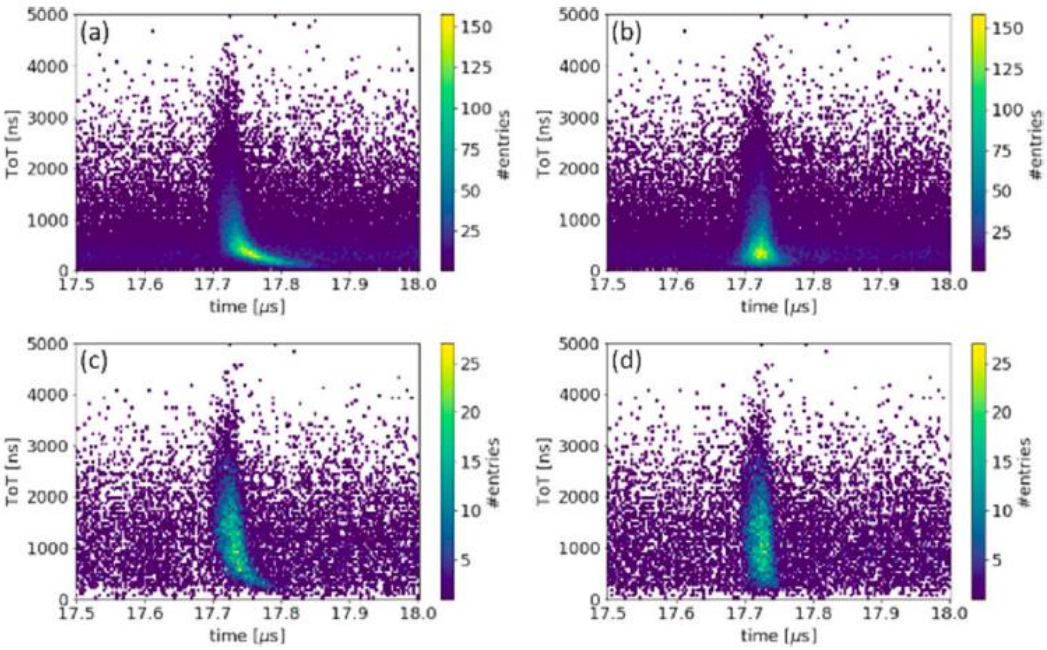


Figure 3.6: Two-dimensional distributions of time, in microseconds, versus TOT, in nanoseconds, for four cases: (a) all hit pixels; (b) all hit pixels with TOT correction applied; (c) centroided pixels; (d) centroided pixels with TOT correction applied (Sen, Hirvonen, et al., 2020).

Figure 3.6 further illustrates the effects of centroiding and TOT correction on the achievable timing resolution, by presenting the two-dimensional distributions of measured time versus TOT for four cases: (a) all hit pixels; (b) all hit pixels with TOT correction applied; (c) centroided pixels; (d) centroided pixels with TOT correction applied. The non-centroided distribution is most affected by the timewalk as it contains many pixels with small signal. After the TOT correction the distributions are vertically oriented minimizing the time spread.

Note that time resolution for this setup is determined by the timing properties of the LED flash, which has a finite rise time and considerable 50 ns duration and, thus, cannot be considered instantaneous. The FWHM resolution, 30.6 ns, achieved in the measurements is, therefore, limited by the LED and can be improved with more sophisticated illumination schemes. The time resolution for single photons measured in the experiments employing pairs of simultaneously

produced entangled photons was measured to be better than FWHM 5.0 ns (Ianzano et al., 2018).

3.2. Conclusion

The spatial resolution of the Tpx3Cam imager was assessed and optimised using different algorithms of centroiding of photon hit events. The centroiding and TOT corrections significantly improved the temporal resolution of the Tpx3Cam imager. Despite not exploiting fully the Tpx3Cam time resolution which is limited by the properties of the LED flash, the current IRF is adequate for PLIM applications with decay times in excess of 100 ns and will not limit the precision of lifetime measurements in this study. System performance can be further improved and extended by replacing the LED with a fast laser source, which can also enable the nanosecond FLIM mode.

Overall, the new system promises good performance in PLIM mode, and is much faster than the other similar devices available in the market. It can image objects upto several centimeters in size with high spatial resolution and flexible optical alignment (e.g., vertical or horizontal configuration). In its present form, the imager is well-suited for various applications based on wide-field PLIM.

4. Chapter 4: Characterization of the chemical samples (oxygen sensors and probes) with the imager

O_2 sensors based on luminescent quenching are used in many applications in different forms and variations (Liebsch et al., 2000; Papkovsky, 2004; Schäferling, 2012). They are popular due to their stable, robust, disposable and easy-to-use design which is not susceptible to electrical interferences (X. D. Wang & Wolfbeis, 2014). Luminescent sensors are therefore regarded as an alternative option to destructive O_2 sensing techniques (Quaranta et al., 2012) as they can measure O_2 in a non-invasive and contactless method.

A significant group of O_2 sensors includes thin film solid-state coatings prepared on various substrates, such as membranes, dots, adhesive stickers, fibreoptic micro-sensors, and coated vessels (Banerjee, Arzhakova, et al., 2016; Kelly et al., 2014; Toncelli et al., 2014; Tsytsarev et al., 2017). The heterogeneity of such materials is a serious problem as it can result in sensor-to-sensor and batch-to-batch variability, unfavourable O_2 quenching behaviour, and poor analytical performance (Degraff & Demas, 2007). The non-uniform colouring of a sensor can also be used to visually identify sensor macro-heterogeneity. Micro-heterogeneity may result from the heterogeneity of the polymeric matrix, mixed polymer phases formed at the coating-support interface, mechanical stress imposed on the material during sensor production, local aggregation of dye molecules (Banerjee, Arzhakova, et al., 2016; Kneas et al., 2000). On the other hand, heterogeneity of the sensor environment and gradients of temperature might lead to inhomogeneous sensing properties. In this case, the sensor can be used to map O_2 concentration in biological and chemical samples (Dmitriev et al., 2013; Okkelman et al., 2016).

In this chapter we further investigate the fast macroscopic wide-field PLIM imager and show how it can be used to characterize various O_2 sensors. For that, we imaged a panel of different handmade, commercial and non-commercial phosphorescent solid-state materials designed for the lifetime-based sensing of

O_2. The performance and accuracy of the PLIM and lifetime measurements were analysed and compared with alternative O_2 measurement and imaging systems.

4.1.Imaging of the different sensor materials

First, arrays of phosphorescent coatings prepared in the different polymers (Figure 4.1a) were prepared by spotting the corresponding sensor cocktails on transparent mylar films and drying. These spotted sensors were imaged under ambient air conditions (22 °C, 20.86 % O_2) at LED power 4 V, pulse width 50 ns and integration time 20 s (627 nm LED, 760±50 nm filter). Corresponding intensity and lifetime images are shown in Figure 4.2a, b respectively. The intensity images (Figure 4.2a) show a large signal variability in each spot, and does not allow reliable distinction between the various polymer-based phosphorescent materials (e.g., high vs moderate vs low O_2 quenching). PLIM images, in contrast, show high colour contrast between the different materials and reveal good uniformity of lifetime values across each individual spot (Figure 4.2b). The comparison of the contrast and uniformity of the lifetime and intensity signals within the imaged spots is shown in the line-profile plots in Figure 4.3a, b respectively. Emission decays for the ROIs marked in Figure 4.2b and their double-exponential fits are shown in Figure 4.3c, which reflect the poly-exponential nature of the decay and low scattering of the photons closely packed around the fit. The PVDC sensors showed the longest lifetime (55.2 ± 1.2 μs), followed by PVC (41.7 ± 0.3 μs), PMMA (41.2 ± 0.3 μs), Hydrogel (20.5 ± 0.3 μs), and polystyrene (15.2 ± 0.2 μs). These results are well in line with O_2 permeability values for these polymers (Ann & Kelly, 2017; X. D. Wang & Wolfbeis, 2014), which in turn determine the efficiency of quenching of PtBP molecules by O_2 (Borisov, 2018; X. D. Wang & Wolfbeis, 2014).

Next, changes in phosphorescence characteristics of the sensor materials under varying macro-environment and its effects on the PLIM images were studied. Temperature is known to have a strong effect on the dynamic quenching by O_2 (Grewer & Brauer, 1993), and when the samples were heated to 40 °C on a temperature-controlled stage, PLIM showed decreases in phosphorescence lifetime, which can be verified by the colour changes in Figure 4.2c. While Hydrogel showed the largest change in the lifetime (~9 μs), PVDC sensor

showed the smallest change (~0.5 µs). Changing temperature also affected the sensor intensity signals, in a similar manner as lifetimes, as shown in Figure 4.4.

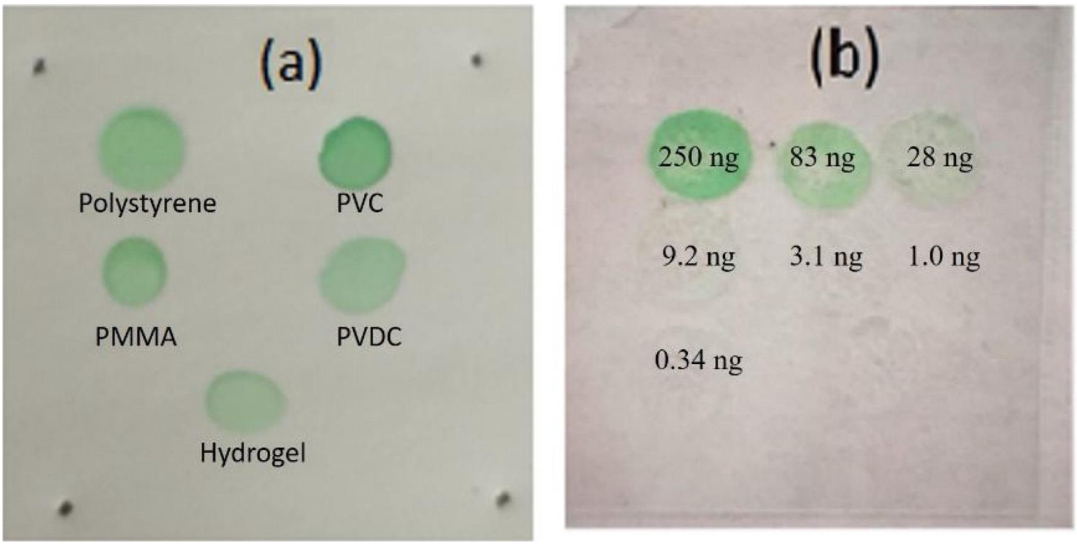


Figure 4.1: Exemplary photographs of arrays of the phosphorescent coatings with 250 ng of PtBP dye in the different polymers (a) and with decreasing PtBP concentration in one polymer (seven serial 1:3 dilutions) (b), spotted on planar solid support. Spot size is 2-3 mm across (Sen, Zhdanov, Hirvonen, et al., 2020b).

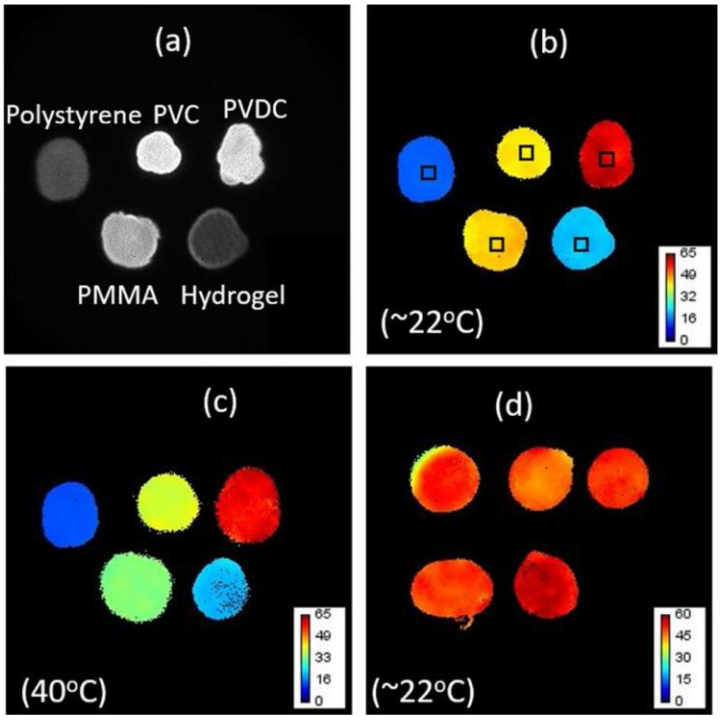


Figure 4.2: Images of the different phosphorescent coatings spotted on polyester film. (a) Grey scale intensity images; (b) PLIM images at room temperature; (c) PLIM images of the sensors obtained at 40 °C; (d) PLIM images of the sensors obtained under zero O_2 condition at room temperature (Sen, Zhdanov, Hirvonen, et al., 2020b). *Images were acquired for 20 seconds with LED at 4V with pulse width of 50 ns.*

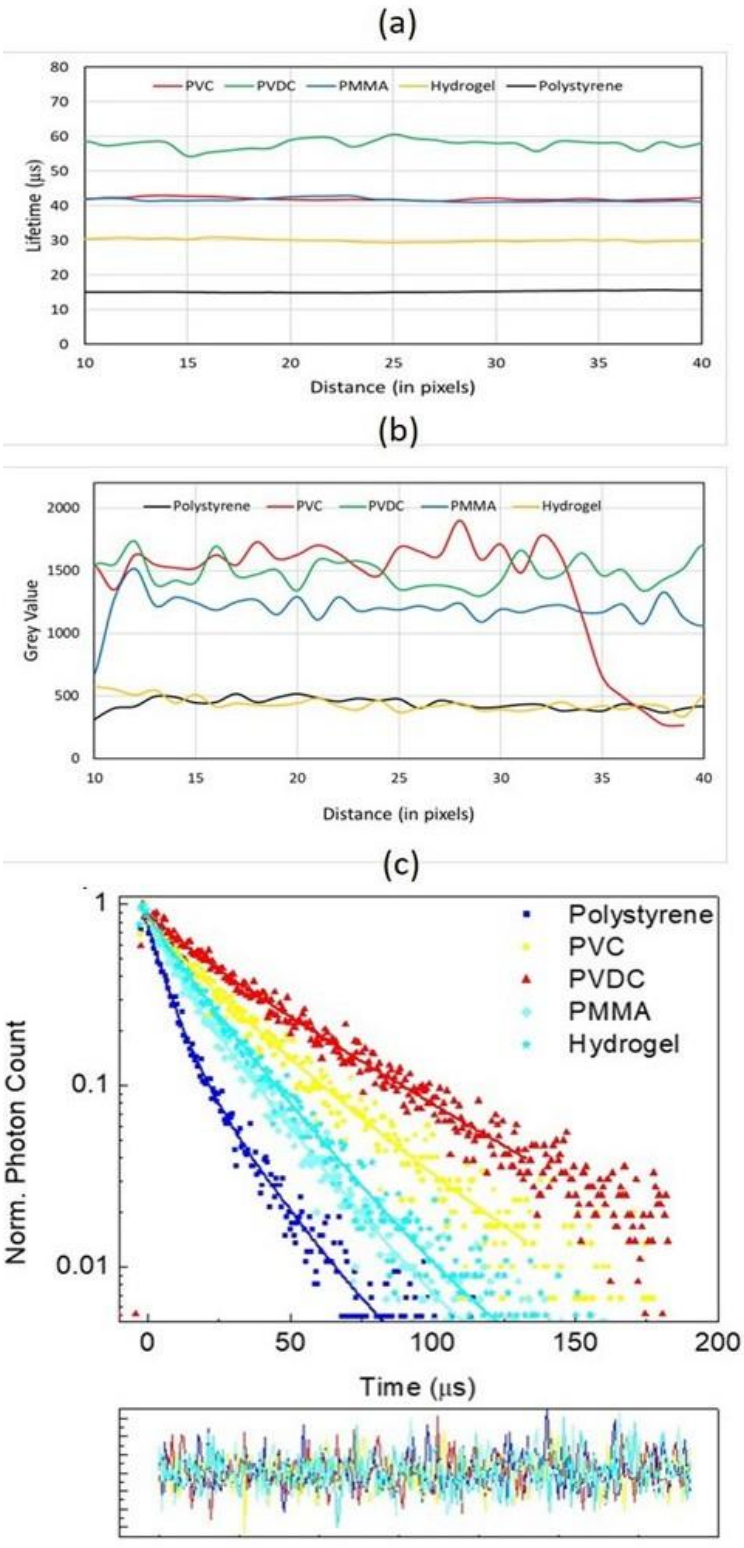


Figure 4.3: Graphs representing (a) line profile across the sensor spots for the PLIM images shown in Figure 4.2b; (b) line profile across the sensor spots for the intensity images shown in Figure 4.2a; (c) Phosphorescence decays with bi-exponential fits for the different ROIs marked in Figure 4.2b (Sen, Zhdanov, Hirvonen, et al., 2020b).

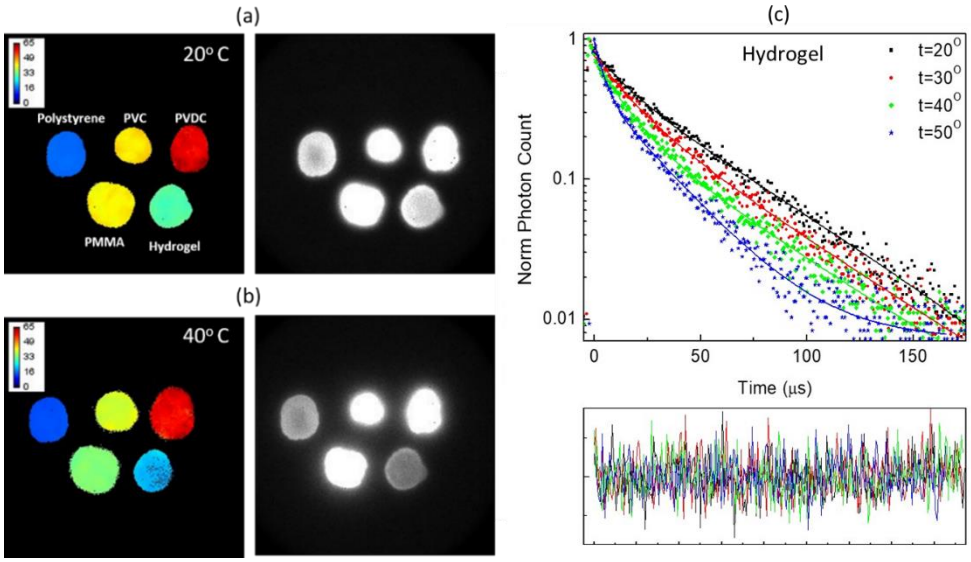


Figure 4.4: Images of the polymeric phosphorescent coatings on polyester support taken on the Tpx3Cam imager at 20°C (a) and at 40°C (b) and presented in lifetime (left) and Intensity (right) scale; (c) Normalised phosphorescence decays for the Hydrogel sensor at different temperatures (Sen, Zhdanov, Hirvonen, et al., 2020b).

The sensitivity of the different sensor materials to O_2 was assessed by calculating and comparing their 'apparent' Stern-Volmer constants K_{sv}^{app} by rearranging eq (1.2):

$$K_{sv}^{app} = (\tau_o/\tau - 1)/20.86 \qquad \text{eq (4.1)}$$

Here τ_o and τ are lifetime values at zero and 20.86 kPa (ambient air) O_2 (Lakowicz, 2006; X. D. Wang & Wolfbeis, 2014). In this case, the higher the K_{sv}^{app}, the higher is the sensitivity of the sensor, and vice versa. The values are listed in Table 4.1, where the polystyrene sensor shows the highest sensitivity, while the PVDC sensor - the lowest, the difference in sensitivity being approximately 100-fold. Also, O_2 quenching and sensor sensitivity increases at higher temperature (40 °C) (seen as lower K_{sv}^{app} values).

Table 4.1: Comparison of the K_{sv}^{app} values for the different sensor materials and temperatures.

PtBP in	LT (22 °C) µs	K_{sv} (22 °C) kPa^{-1}	LT (40 °C) µs	K_{sv} (40 °C) kPa^{-1}
Polystyrene	15.2 ± 0.2	0.114	13.3 ± 0.1	0.137
PVC	41.7 ± 0.3	0.004	37.8 ± 0.4	0.009
PVDC	57.5 ± 1.4	0.001	57.0 ± 1.4	0.001
PMMA	41.2 ± 0.3	0.009	33.1 ± 0.4	0.023
Hydrogel	29.4 ± 0.5	0.043	17.5 ± 6.3	0.097

Note that complete multi-point O_2 calibrations are necessary for the identification of "true" K_{sv} values and accurate comparison of sensor sensitivity. Unfortunately, this was not possible with our lab's current PLIM imaging and O_2 calibration setups (separated in space). As a result, the above simplified approach was employed which is frequently used by researchers (X. D. Wang & Wolfbeis, 2014).

The sensor film was also soaked in deoxygenating solution (phosphate-sulfite buffer) and imaged. In this deoxygenated state (Figure 4.2d), the lifetime signals of all the sensors approached ~50 μs, which corresponds to the unquenched lifetime of PtBP (Hutter et al., 2014). The dramatic lifetime contrast between the sensors observed in the oxygenated state (Figure 4.2b) almost disappeared. Small differences between the spots are due to PtBP quenching by the polymer itself.

Several other commercial and non-commercial sensors based on PtBP dye were also imaged under normal conditions, using the similar LED power and integration time as before. Figure 4.5a shows photographic images of the different sensors, while Figure 4.5b shows their PLIM images. The PVDF membrane (12.9±0.9 μs), bead sensor (13.3±0.4 μs) and the sensor from Pyroscience (13.5±0.6 μs) all showed similar lifetime values and variability (S.D.), whereas higher lifetime values were noted for the Optech® sensor (15.4±0.4 μs) and for the membrane sheet (19.9±0.07 μs). The extruded LDPE and PLA sensor pellets and films based on the PtBP phosphor (Figure 4.5c) were also analysed, under the same optical settings. The PLIM images of the sensors are shown in Figure 4.5d. The PLA pellet and film in Figure 4.5d cannot be differentiated due to thresholding limits. The lifetime values for the PLA sensors (36.5±0.4 μs) was significantly higher than for the LDPE sensors (13.7±0.1 μs), in agreement with the reported data (Kelly et al., 2020).

The PtOEPK-PS based O_2 sensors (Papkovsky et al., 1995), which are spectrally compatible with the Tpx3Cam imager set-up, were also imaged. Their photographic and PLIM images are shown in Figure 4.5e, f, respectively. The two different sensor types (spots on filter paper and PVDF membrane support) produced similar mean lifetimes and standard deviation of 15.8±0.2 μs and

15.4±0.15 µs respectively. These results are also consistent with other reported data (Papkovsky et al., 2002; Smiddy et al., 2002).

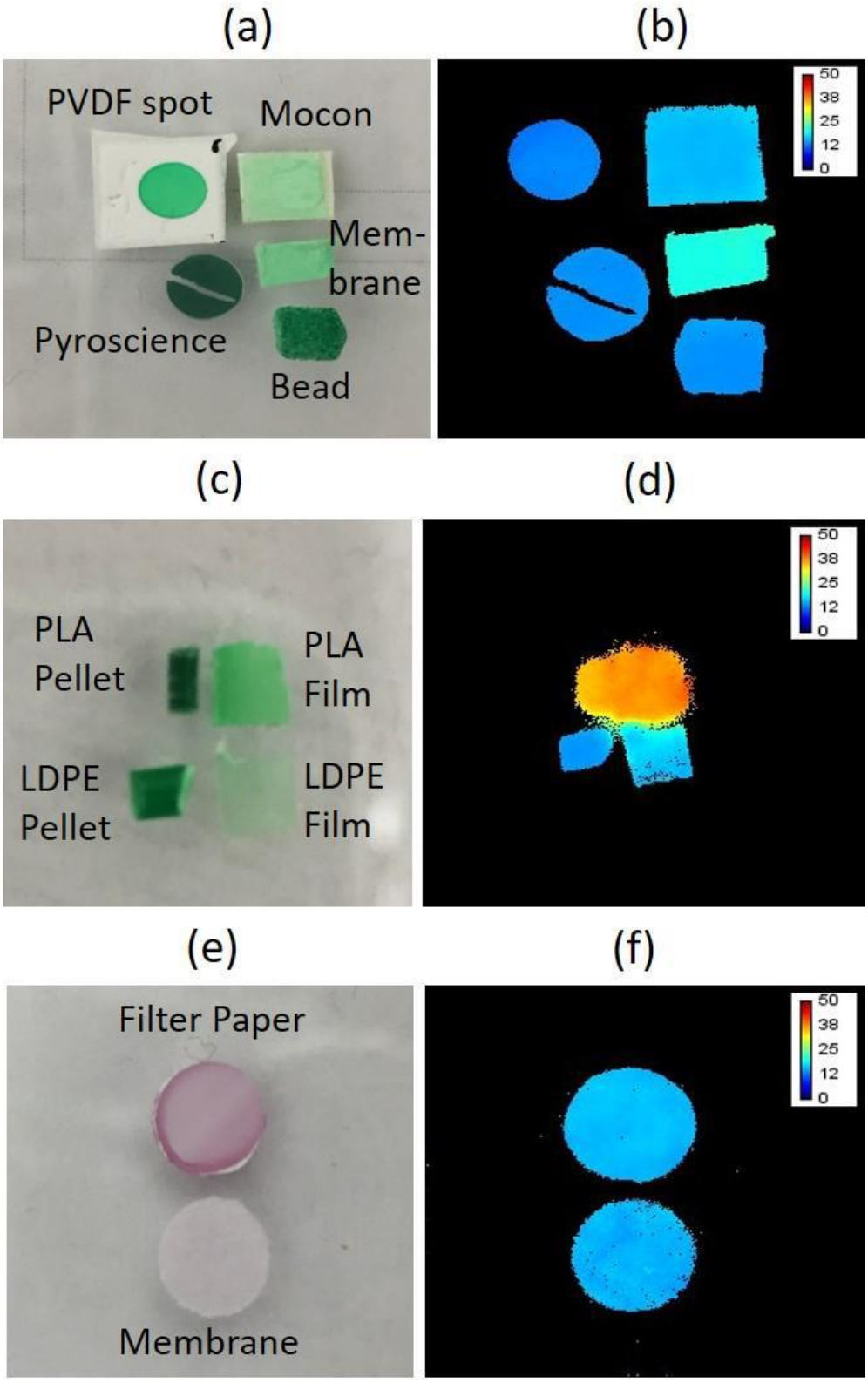


Figure 4.5: Sets of commercial and custom-made O_2 sensors imaged with the Tpx3Cam imager. (a) Photograph and (b) PLIM image of the PtBP based sensors in various forms; (c) Photograph

and (d) PLIM image of LDPE-PLA based PtBP sensors and (e) Photograph and (f) PLIM image of the two PtOPEK based sensors (Sen, Zhdanov, Hirvonen, et al., 2020a).

PtOEP, PtOEP/OEPK and PtOEP-SB sensors were also measured with the Tpx3Cam imager. The 627 nm LED and 760±50 nm filter was replaced with 390 nm LED and 648±50 nm bandpass emission filter. The prepared sensors were submerged in PBS and lifetime signals were recorded for air-saturated conditions and after chemical deoxygenation by the addition of 5 mg/ml Na_2SO_3 and 5 mg/ml K_2HPO_4. The width and amplitude of the LED pulse was optimised and lifetime images were acquired at LED power 4 V, pulse width 500 ns and integration time 20 s. The parameters for decay fitting were also optimised. Initially, all the photons in the decay were fitted with a biexponential function, but this produced an uneven distribution of the residual and very high counts at the start of the decay (photons enclosed in the dotted box in Figure 4.6b). These high initial signals, which affected the lifetime measurements (long exposure time), were attributed to background emission of sensor support materials (Mylar film, cuvette, Petri dish, etc.). To reduce these effects, fitting parameters were optimised by shifting the start point of the fit to 25 μs. This produced more even distributions of the residual and stable PLT values. All the sensors imaged on the Tpx3Cam imager produced two distinct lifetime components - τ_1 (short) and τ_2 (long), which increased their values in deoxygenated state. Since only the value of the τ_2 component was close to the reported lifetime values [16], in this study τ_2 was considered as true lifetime value of the sensor dye. The cumulative distribution histograms for all the sensors in oxygenated and deoxygenated state, are shown in Figure 4.6c, d, e and corresponding PLT values are reported in Table 4.3.

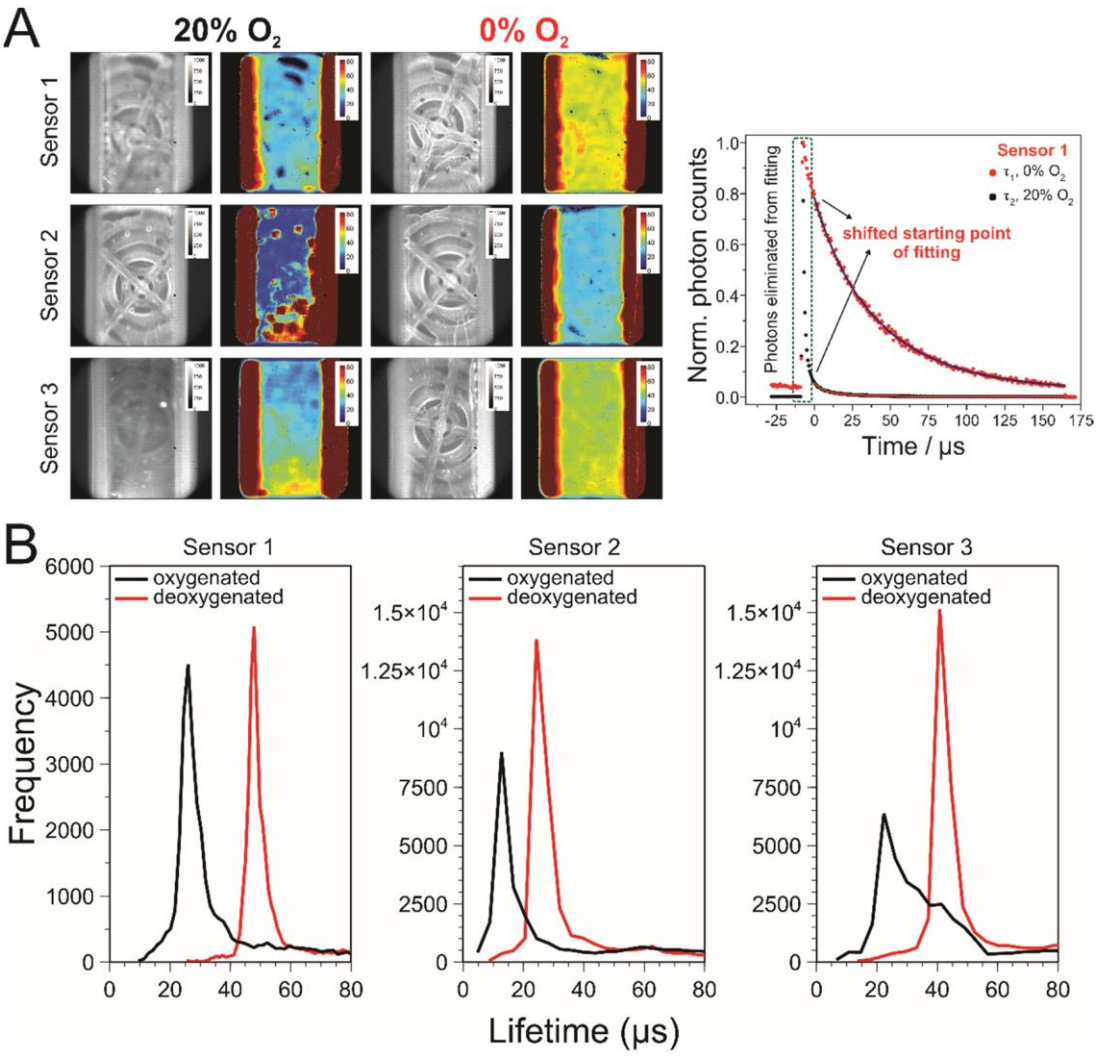


Figure 4.6: The PLT data for Sensors 1–3 generated on the Tpx3cam imager under oxygenated and deoxygenated conditions. (a) shows the intensity and PLIM images of sensor 1–3 in their oxygenated and deoxygenated state. (b) shows the decay fittings for sensor 1 in its oxygenated and deoxygenated state. c, d and e represent the cumulative distribution histograms for sensors 1–3 in oxygenated (21% O_2) and deoxygenated (~0% O_2) conditions* (Sen et al., 2022). **Sensor 1: PtOEP, Sensor 2: PtOEP + OEPK, Sensor 3: PtOEP-SB*

4.2. Comparison of the different sensor materials and lifetime detection platforms

Reference measurements were also carried out with identical samples on a confocal TCSPC-PLIM microscope under high magnification (5x air objective), to evaluate the precision of lifetime measurements on the Tpx3Cam imager and compare the results. The corresponding confocal PLIM images are shown in Figure 4.7.

Comparison was also made between the commercial sensors from PyroScience and Mocon (both are based on PtBP dye (Kelly et al., 2018a)) and our hand-made sensor materials. Table 4.2 shows mean lifetime values and standard deviations for the various sensors measured on the two platforms. Note that lifetimes were determined at room temperature and 21% O_2, using the best signal acquisition parameters for each detection platform. The signal acquisition time was 20 s (all pixels were recorded simultaneously) for the Tpx3cam imager, while the confocal PLIM microscope's signal acquisition time was 219.2 µs/pixel (recorded one at a time with a total acquisition of 60 s).

Table 4.2: Comparison of phosphorescence lifetime measurements on the Tpx3Cam imager and confocal PLIM microscope.

Sensor 21°C	Tpx3Cam lifetime (µs)	Confocal lifetime (µs)
Polystyrene	15.2 ± 0.16	20 ± 5.9
PVC	41.7 ± 0.26	40 ± 11.7
PVDC	55.2 ± 1.2	50 ± 5.9
PMMA	41.2 ± 0.27	40 ± 11.7
Hydrogel	20.5 ± 0.25	20 ± 5.9
Optech (Mocon)	15.4 ± 0.11	17.6 ± 13.2
Pyroscience	13.5 ± 0.07	15.8 ± 4.4

According to Table 4.2, commercial sensors from Mocon and PyroScience have lowest variability (S.D. = 0.11 µs and 0.07 µs, Relative Standard Deviation (RSD) = 0.71% and 0.52%, respectively), followed by the home-made PVC and PMMA sensors (S.D. of 0.26 µs and 0.27 µs, and RSD 0.62% and 0.65%, respectively). The home-made PVDC sensor shows the highest variability (S.D.=1.2 µs, RSD=2.17%).

Overall, lifetime measurements were consistent on both the platforms. Greater variability was seen in the lifetime values measured on the confocal microscope. We attribute this to the high micro-heterogeneity of the sensors (not visible on the macroscopic imager), harder Z focusing of the confocal system onto the

sensor coating, and pixel-by-pixel scanning. It should be noted that the two sets of imaging data were conducted on different days and without active control of the sensor environment. As a result, changes in ambient temperature and barometric pressure may have influenced the recorded lifetime signals from the sensors.

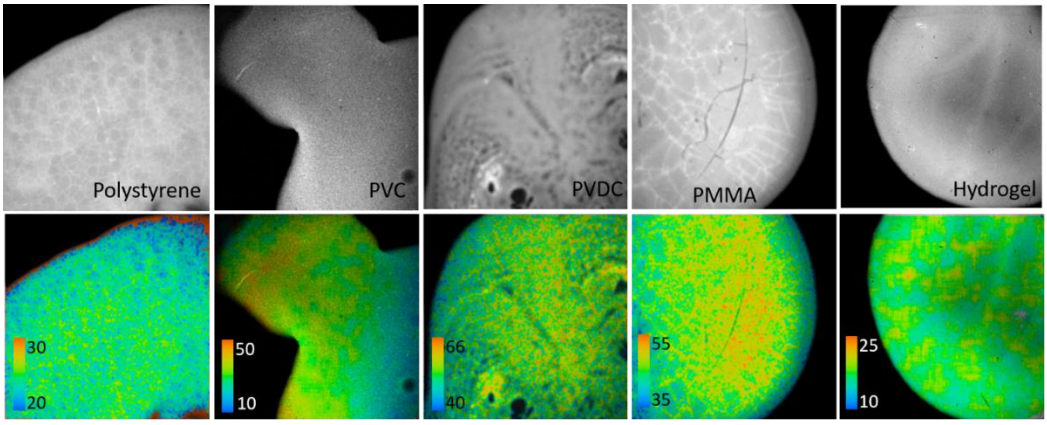


Figure 4.7: Intensity (top) and lifetime (bottom) Images for the different phosphorescent coatings on polyester support, measured on the confocal PLIM microscope at room temperature (Sen, Zhdanov, Hirvonen, et al., 2020b).

PtOEP, PtOEP/OEPK and PtOEP-SB sensors were also measured on the confocal FLIM system. The following imaging parameters were optimised: laser power, pinhole aperture, image collection time, the number of imaging cycles for each pixel, time range for decay recording and laser-on time for generating the phosphorescence signal (% of the total time range). High resolution PLIM images with 0.5-1 × 10^4 counts per pixel were obtained with a 2 mm pinhole and at 30–50% laser power. Fitting accuracy of decay tails having different length was compared and the 250 μs time range was found optimal. 10.26% laser-on time was chosen for systematic imaging of the sensors in oxygenated and deoxygenated states. While optimising data processing, the τ_m and τ_2 values produced via mono- and bi-exponential fitting (20.6 μs and 20.4 μs, respectively for PtOEP in oxygenated state) and the corresponding χ^2 values were almost identical. And τ_1 component was not observed for at 0% oxygen. Therefore, the data processing was simplified to mono-exponential fitting for all the sensors and conditions. Using the algorithm described in (Zhdanov et al., 2017), the phosphorescence lifetimes of the sensors were measured and the result are listed in Table 4.3. Both imaging platforms revealed the bi-exponential nature of

PtOEP decay, but due to the different hardware, software and fitting algorithms, the PLT values produced by the Tpx3cam and the FLIM microscope did not match, although good convergence of the results was observed for PtOEP-SB (Table 4.3).

Table 4.3: PLT measured on the two imaging platforms. The lifetime values (µs) were obtained from the lifetime histograms.*

Sensors and O_2 levels		Confocal			Tpx3Cam		
		25th quartile	**Median**	**75th quartile**	**25th quartile**	**Median**	**75th quartile**
PtOEP	21 %	18.8±0.3	**20.4±0.0**	21.9±0.3	25.3±1.7	**26.9±1.8**	29.1±1.7
	~0 %	51.3±2.2	**57.2±1.7**	61.9±2.1	44.9±5.5	**46.6±6.1**	48.4±6.7
PtOEP + OEPK	21 %	10.1±0.30	**10.8±0.2**	11.6±0.2	13.5±1.3	**14.7±1.3**	15.9±1.3
	~0 %	19.9±0.2	**21.1±0.4**	22.8±0.9	26.1±3.2	**27.04±3.5**	28.3±3.8
PtOEP-SB	21 %	22.0±0.3	**23.7±0.2**	25.6±0.6	20.7±2.7	**22.3±1.9**	23.9±2.1
	~0 %	33.4±0.3	**35.6±0.4**	37.0±0.8	38.9±2.7	**39.7±2.8**	40.7±2.8

* Measured at 37°C in PBS (21% O_2) or PBS with added sulphite (~0% O_2).

Polystyrene and PVDC based sensor coatings with PtBP dye were also measured with a handheld lifetime reader Optech® Platinum (Mocon) at different O_2 concentrations. Figure 4.8 shows the corresponding O_2 calibrations in dry gas at 25°C. One can see, that the polystyrene coating showed a significant change in the lifetime values, so it can act as an efficient sensor for the physiological O_2 range (0 - 21 kPa or 0 - 21% in air). O_2 calibration of the hand-made polystyrene coating was similar to commercial Mocon sensors (Kelly et al., 2020).

The PVDC coating, in contrast, produced only minute lifetime changes at increasing O_2 concentration (from zero to 21 kPa). Due to inadequate O_2 permeability of PVDC (>200-times lower than polystyrene (Brandrup et al., 2003)), such sensors are not suitable for the same applications. However, they can be used at high kPa settings, e.g., in pressurized samples.

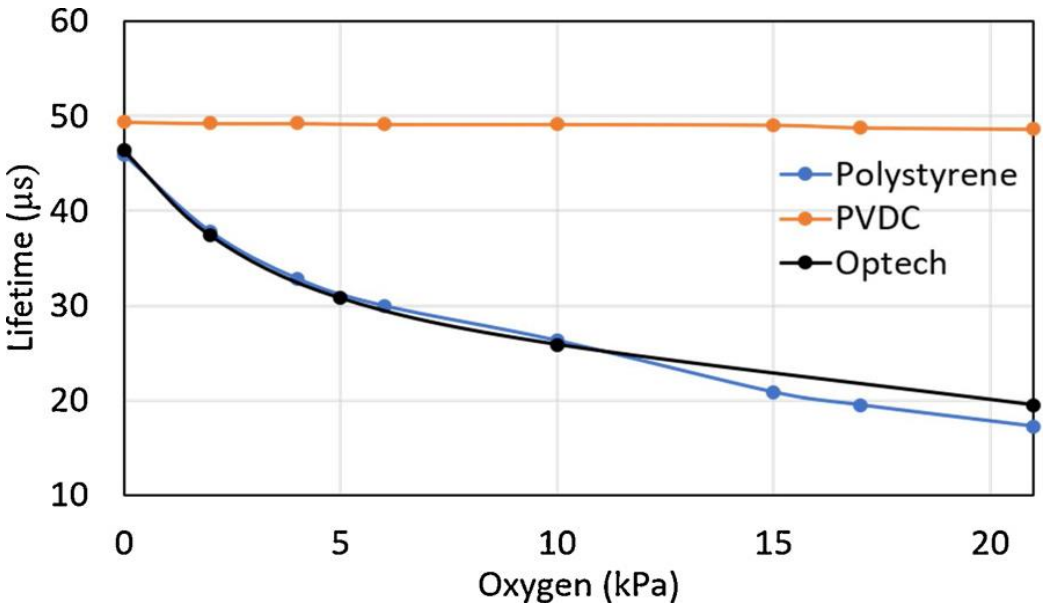


Figure 4.8: Lifetime response to O_2 partial pressure for the polystyrene, PVDC and Optech (Mocon) sensors/coatings at 25 °C (Sen, Zhdanov, Hirvonen, et al., 2020b).

4.3. Sensitivity of the PLIM macro-imager and stability of lifetime measurements.

The sensitivity and stability of PLIM on the Tpx3Cam system was evaluated by imaging an array of phosphorescent coatings with different PtBP content. Figure 4.9 shows the lifetime and intensity images of the sensor palettes in five different polymers in pseudo-colour and grey scale respectively. On each panel, the top left spot corresponds to undiluted cocktail, followed by six spots with 1:3 serial dilutions. The amounts of the dye per spot were 250 ng, 83 ng, 28 ng, 9.2 ng, 3.1 ng, 1.0 ng and 0.34 ng, respectively.

The PLIM images show constant lifetime signal for the first 4-5 spots, i.e., down to about 3 ng of the dye per spot. After this, lifetime values start to change, due to low photon counts and large errors in decay fits. The stable lifetime measurements are reflected by the constant colour for the PLIM images. Among these sensors, Hydrogel D4 spots showed the most stable mean lifetime: 21.9 ± 0.4 µs. For the others, lifetime variations were between 1 and 3 µs.

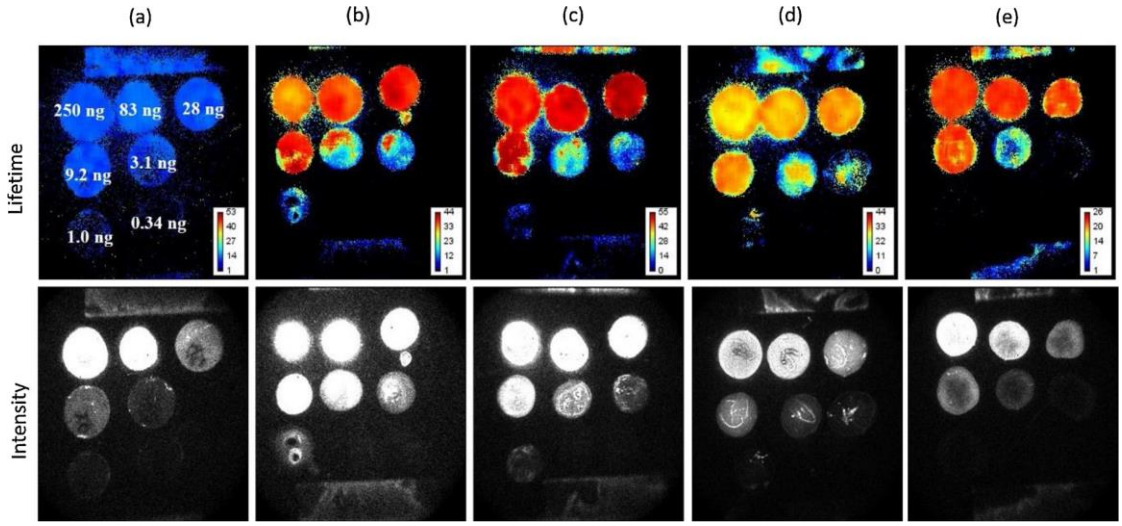


Figure 4.9: PLIM (top row) and intensity (bottom row) images of the sensor palettes prepared using the cocktails with 1:3 serial dilutions of PtBP dye in: (a) Polystyrene, (b) PVC, (c) PVDC, (d) PMMA and (e) Hydrogel D4 (Sen, Zhdanov, Hirvonen, et al., 2020b).

In comparison, the corresponding intensity images showed gradual reduction in sensor intensity signals after first 1-4 dilutions. Figure 4.10 represents the variation in the intensity and lifetime recorded for these spots. While there was a variation in the intensity, the lifetime remained stable at decreasing concentrations. At higher dilutions (starting from the 5th spot) the spotting areas were not clearly visible, since the counts of the emitted photons were comparable with background noise. It is worth noting, that the sensor patterns in Figure 4.9 were produced under the imaging settings optimized for high dye concentrations. The quality of PLIM and intensity images for the spots with low dye content can be significantly improved by increasing excitation energy (pulse width) and integration time. This will increase the sensitivity and stability of PLIM measurements on the Tpx3Cam imager for weakly emitting samples. However, in this case, strongly emitting spots cannot be visualized reliably, due to overload of photons and detector saturation in the corresponding pixels.

4.4. Conclusions

Several phosphorescent coatings based on PtBP dye were prepared and tested with the Tpx3Cam imager. Despite the crude fabrication procedure (manual spotting of the polymeric ‘cocktails’) and prominent heterogeneity in intensity signals, in the PLIM mode these materials exhibited good uniformity, contrast

and lifetime response to changing environmental conditions, particularly temperature and deoxygenation. Among the different phosphorescence materials, polystyrene sensors showed the highest sensitivity to the changing macro environments, whereas PVDC sensors showed the lowest. Although upon deoxygenation, the lifetime signals of all the sensors reached ~50 µs, which corresponds to the unquenched lifetime of PtBP. Analytical performance of

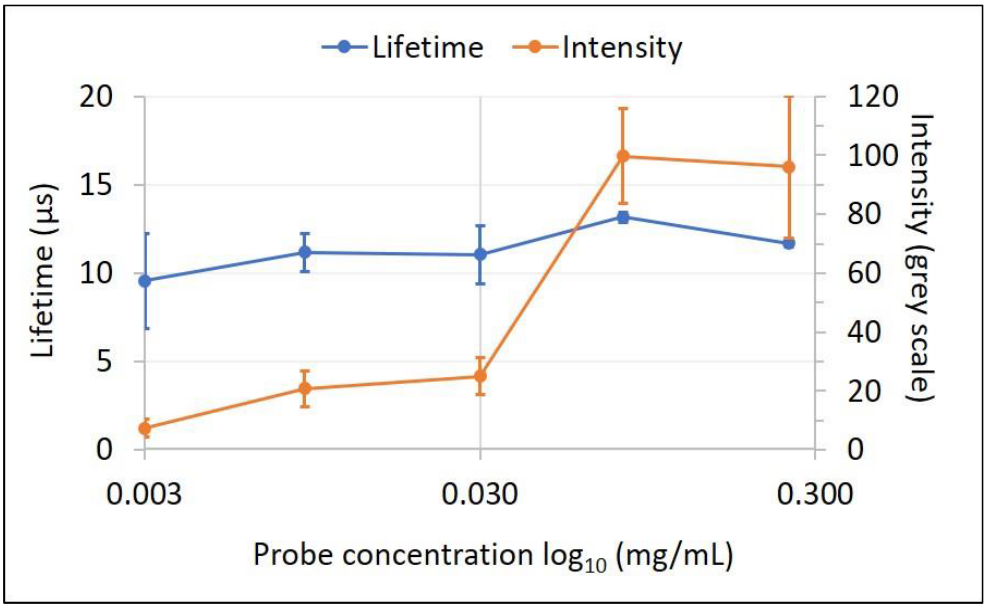


Figure 4.10: Variation of the intensity and lifetime for Polystyrene based PtBP dye with increasing dilutions (Sen, Zhdanov, Hirvonen, et al., 2020a).

these handmade O_2 sensors was comparable to the commercial sensors currently in use. For this type of samples, the Tpx3Cam imager produces more accurate lifetime readings, better quality PLIM images, at superior speed and sensitivity than the state-of-the-art confocal TCSPC-PLIM microscope. The results also reveal a significant number of factors that may lead to measurement artefacts and inaccuracies in the determination of lifetime values under UV excitation. Strong fluorescence in the same range as phosphorescence may 'blind' the detector and decrease the sensitivity of measurements. By carefully eliminating the factors that may lead to measurement artefacts and inaccuracies, the Tpx3Cam imager can be used for fine characterisation of solid-state O_2 sensors, studies and optimisation of their homogeneity and operational performance.

5. Chapter 5: Mapping O_2 in biological samples with Tpx3Cam Imager

O_2 imaging in biological samples by means of phosphorescent probes and live cell optical microscopy is widely being used in biomedical research (Devor et al., 2012; X. D. Wang & Wolfbeis, 2014). The lifetime and intensity of phosphorescent probes used to stain tissue samples are reversibly changed in response to the local O_2 concentration (Borisov, 2018; Papkovsky & Dmitriev, 2018). Low lifetime values indicate high O_2 concentrations (for example, 210 µM in an air-saturated aqueous solution at 37 °C) and low respiratory activity of the sample. High lifetime values, on the other hand, imply depleted O_2. Phosphorescence intensity signal is influenced by the distribution of the probe within the cells or tissue sample, staining efficiency, photobleaching, imaging geometry, and other elements. As a result, it is extremely difficult to obtain good quantitative imaging of O_2 concentration in intensity mode. However, these restrictions are essentially absent from phosphorescence lifetime-based O_2 sensing, which is why it is recognized as the preferred technique for O_2 imaging (Dmitriev & Papkovsky, 2018).

The family of cell-permeable nanoparticulate O_2 sensing probes (Fercher et al., 2011; Kondrashina et al., 2012) includes the NanO2-IR probe. The nanoparticles formed by RL-100 polymer help to maintain the hydrophobic molecules of the phosphorescent dye, provide an ideal microenvironment for their quenching by O_2 molecules, and shield against undesirable interferences. The polymer permits stable and accurate O_2 calibration, effective staining of cells and tissues, and solubility of the probe in aqueous solutions. The high brightness, near-infrared spectral properties of PtBP dye (excitable at 620 nm, emits at 760 nm (Tsytsarev et al., 2013)) enable the detection of minute amounts of NanO2-IR and its use in high-resolution O_2 imaging applications.

In this study, we used NanO2-IR probe and Tpx3Cam imager to measure O_2 levels in various biological samples, including mammalian cell suspensions, *ex vivo* samples of live animal tissue, and whole organs extracted from sacrificed

animals. The objective was to test the sensitivity of the imager, evaluate and optimize conditions for tissue staining and PLIM imaging, intensity signals, and lifetime determination, and produce accurate data on O_2 concentration and distribution in various samples. Additionally, we aimed to determine the imager's suitability for *in vivo* research with live animals and human disease models.

5.1.Imaging of *ex-vivo* tissue samples

Several types of samples, including cultured cells, tissue, and organs extracted from sacrificed mice, were stained with the NanO2-IR probe under different conditions and then imaged on the imager at 37°C to evaluate oxygenation state and O_2 gradients, which reflect cell respiration activity. The staining (time, temperature, probe quantity) and imaging (LED and intensifier power, sample distance, signal collection time) protocols were optimized for each tissue model.

5.1.1. Imaging of respiring cells

Cultured cells are usually stained with nanoprobes based on RL-100 polymer at concentrations 5-50 μg/mL for 3-24 hours incubation times at 37ºC (Fercher et al., 2011; Kondrashina et al., 2012). Probe cytotoxicity is undetectable in these circumstances. *Ex vivo* tissue samples, on the other hand, are unstable and demand faster staining (Tsytsarev et al., 2013), which can be achieved with higher probe concentrations but may have severe cytotoxic effects. The cytotoxicity of NanO2-IR at a concentration of 1 mg/ml in the medium was investigated using two most commonly used cell lines, HCT116 and HEK293a. Total ATP analysis during a 4 hour exposure period showed no significant changes in cell viability in the first hour or so, and a sharp decline in viability from 2 hours onwards (Figure 5.1a). Based on these findings, we aimed to perform imaging tests on live cells and tissues within 1 hour after the start of their staining.

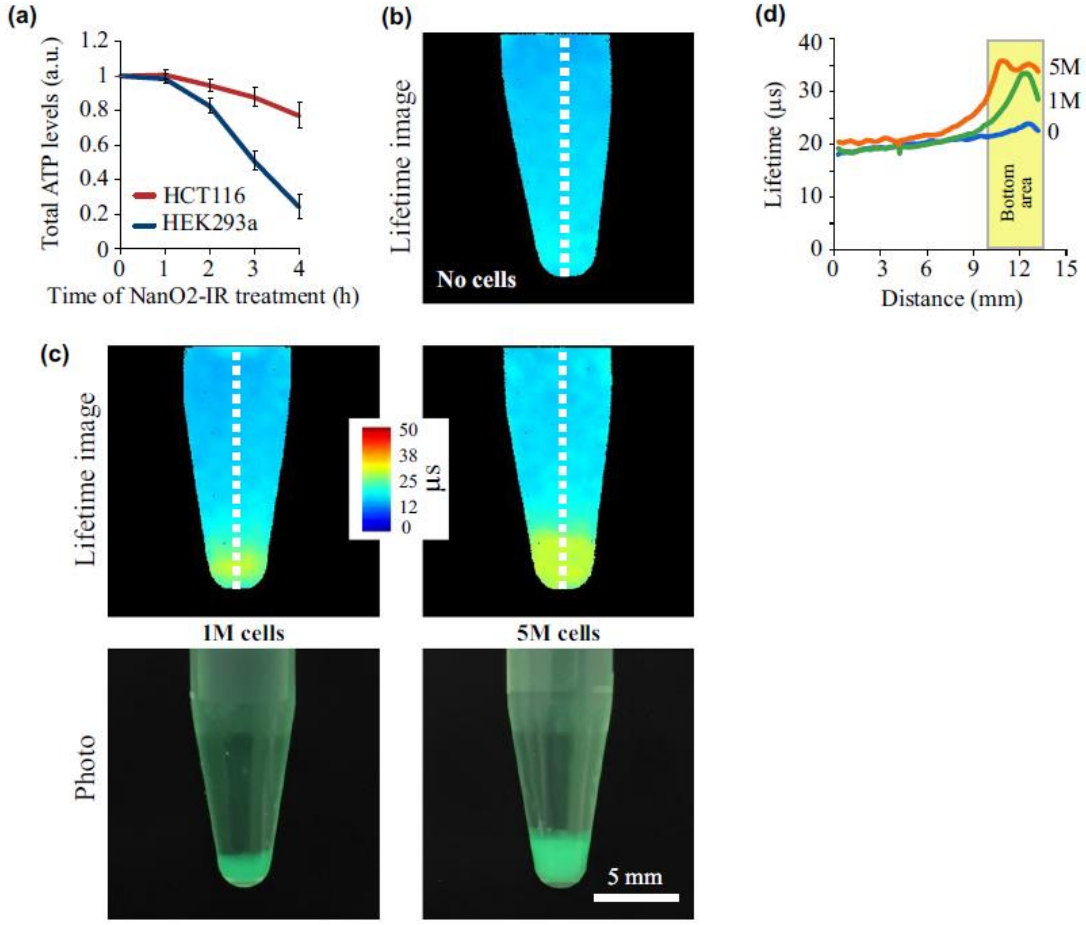


Figure 5.1: PLIM of dissolved O_2 distribution in media containing cultured cells. (a) Effects of NanO2-IR on viability of HCT116 and HEK293a cells. Total ATP levels were measured with CellTiter-Glo ATP assay after incubating the cells with the probe (1 mg/mL) for indicated time; all values are normalised to ATP levels in untreated cells. N = 3, mean ± SD are shown. (b, c) PLIM images of the probe (1 mg/mL) evenly distributed in growth medium containing no cells (b), and 1 × 10^6 or 5 × 10^6 of respiring HCT116 cells precipitated at the bottom; (c) photographs of 0.5 mL qPCR tubes with cell pellets. False colour images show increased lifetime values (µs), or decreased O_2 in and near the cells. (d) line profile analysis (along the dotted lines in (b) and (c)) quantifies this effect (Sen, Zhdanov, Bastiaanssen, et al., 2020).

Next, different number of live mammalian cells in growth media containing 1 mg/ml NanO2-IR were placed in 0.5 mL Eppendorf tubes and gently centrifuged to form a pellet at the bottom of the tube. The sample was incubated 30 min at 37°C to create O_2 gradients in the surrounding liquid, and then imaged. Before centrifugation, the NanO2-IR probe was added at a final concentration of 1 mg/ml, and it stayed both in the medium and within the cell pellet. Figure 5.1b, c show PLIM images of the tubes containing 0, 1x10^6, and 5 x10^6 respiring HCT116 cells. As seen in Figure 5.1b, the sample free of cells exhibits a constant

color and lifetime values, which are consistent with air-saturated conditions (210 µM O_2) throughout the tube. The narrow bottom portion of the tube, which was equilibrated at 37ºC and placed on the imager stage, cooled down more quickly than the middle and top, leading to the small increase in lifetime (color gradient). On the other hand, samples with $1x10^6$ and $5x10^6$ cells had strong O_2 gradients (Figure 5.1c), which increased with cell number. The significantly higher lifetime values within the pellets at the bottom of the tube reflect O_2 depletion caused by cell respiration. The lifetime values in the middle and top parts of the tubes are low and do not vary much due to air saturation in the medium layer, which serves as a barrier for O_2 transport to the cells. Yet, minute changes in temperature can cause the lifetime variability observed in these parts of the samples.

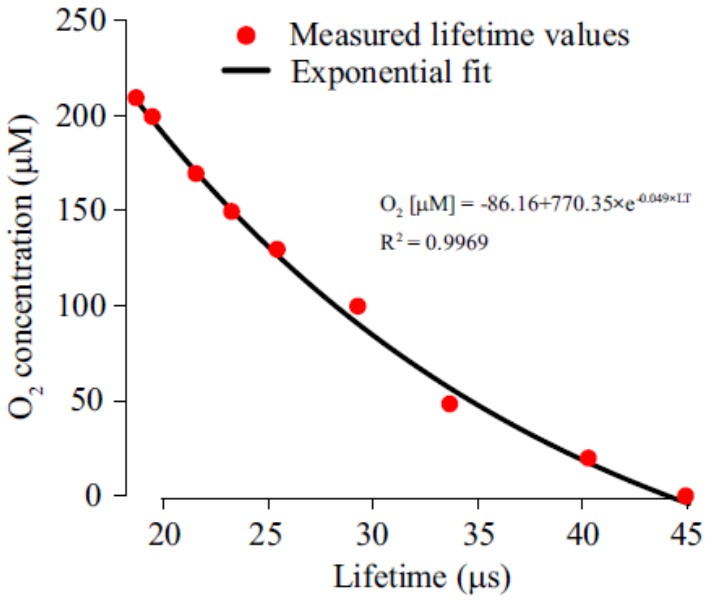


Figure 5.2: O_2 calibration of NanO2-IR probe under physiological conditions. Lifetime values were measured with a handheld reader Optech (Mocon, USA) in liquid samples (DMEM media) equilibrated with 0%, 2.0%, 5.0%, 10.0%, 12.0%, 15.0%, 17.0%, 20.0% and 21.0% O_2 gas standards produced on a gas mixer, at 37 °C. Exponential fitting was performed using https ://mycur vefit .com/ (Sen, Zhdanov, Bastiaanssen, et al., 2020).

O_2 calibration of NanO2-IR (1 mg/mL in DMEM) was performed at 37ºC using the handheld Optech® reader, by measuring the phosphorescence lifetime of the sample equilibrated with known gas mixtures (O_2 balanced with N_2). The calibration data points and their fitting are shown in Figure 5.2, which give the

following analytical equation for O_2 calibration: O_2 [µM] = -86.16+770.35$e^{-0.049xLT}$. It can be used to convert the measured lifetime values (LT [µs]) and PLIM images into O_2 concentrations and O_2 maps, respectively.

Based on these findings, it was concluded that the bright phosphorescent probe NanO2-IR and the novel Tpx3Cam-based PLIM imager can be used to accurately measure O_2 in live tissue samples isolated from sacrificed animals using the once-off calibration function described above.

5.1.2. Imaging of mouse brain and lung tissue surface-stained with NanO2-IR probe

Due to the ethical and technical constraints associated with the use of live animals, in this study we used tissue samples freshly isolated from sacrificed animals. The cells in the isolated tissues were still alive and respiring, though stressed as their normal supply of O_2 through vasculature was interrupted. In the *ex vivo* setting, O_2 passively diffuses to the tissue samples from an air-saturated medium or ambient air, which could impose additional hypoxic stress to the inner tissue areas. O_2 solubility, quenching efficiency of NanO2-IR, and respiration activity of cells are strongly influenced by temperature (Borisov, 2018; Papkovsky & Dmitriev, 2018), therefore temperature of the sample stage was maintained at 37°C during the experiment. With the above limitations, these tissue models are not ideal for physiological studies, however they were considered appropriate to assess the analytical performance and suitability of the PLIM imager for *in vivo* applications.

We imaged different types of animal tissue stained by topical application of NanO2-IR probe. Firstly, three specimens of whole brain cortex and lung were stained with NanO2-IR and analyzed with PLIM. The following staining and imaging protocols were used for both the tissue type. Sample 1 was stained for 30 min and then imaged. Samples 2 and 3 were stained for 15 min, imaged, then treated with respiration inhibitors for 30 min and imaged again under the same settings. Sample 1 was imaged again as an untreated control to trace possible changes in tissue oxygenation over the time of the experiment. The settings for acquiring PLIM images of these and other tissue types are given in Table 5.1.

Table 5.1: Exemplary/typical PLIM acquisition parameters used for the different tissue types and staining methods.

Tissue (staining method)	Treatm-ent	Imaging time (sec)	Total frame number	Triggered pixels number	Readout rate (MHz)	Photon events number	Event size range	Undersize events number	Oversize count rate (MHz)	Photon count rate (MHz)
Cortex (outer surface)	No	20	99210	52803332	2.6	9364458	3-15	704703	1066970	0.5
	AntA / NaN_3	20	99923	38134789	1.9	7196821	3-15	489437	628022	0.4
Lungs (outer surface)	No	20	99453	22779858	1.1	4425511	3-15	355928	336448	0.2
	AntA / NaN_3	20	100014	25072928	1.3	4938119	3-15	404726	361494	0.2
Large intestine (intralu mi-nal)	No	20	100120	28378586	1.4	4713630	3-15	365106	572190	0.2
	AntA / NaN_3	20	100185	24924614	1.2	4226943	3-15	355015	479318	0.2
Small intestine (intralu mi-nal)	No	20	100028	23500000	1.2	4052414	3-15	347450	433438	0.2
	AntA / NaN_3	20	100141	37126634	1.9	6044806	3-15	476891	797582	0.3

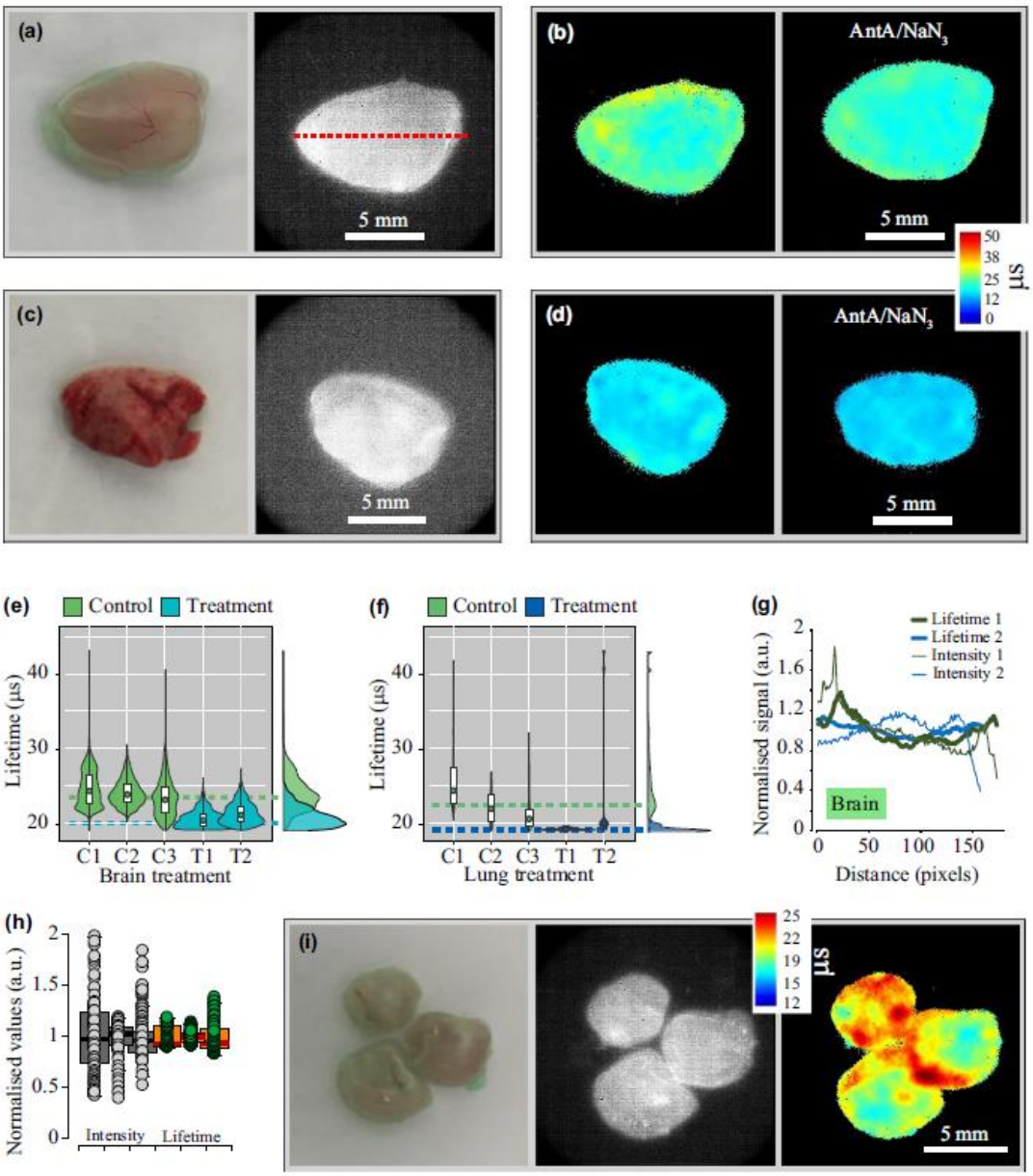


Figure 5.3: PLIM of O_2 in the surface-stained mouse brain and lung tissue samples. (a) Photograph and phosphorescence intensity image of cortex tissue samples stained with NanO2-IR (1 mg/mL in DMEM, 30 min). (b) Corresponding PLIM images of the untreated control (C1-C3) and AntA/NaN3-treated samples (T1, T2). (c) Photograph and phosphorescence intensity image and (d) PLIM images of untreated control (C1–C3) and AntA/NaN_3-treated lung tissue samples (T1, T2). (e, f) Lifetime frequency histograms for the brain and lung tissue with normal and inhibited mitochondrial respiration. Violin plots show: on the Y-axis—the distribution of lifetime values; on the X-axis—sample names and relative frequencies, with which lifetime values were recorded. Box-plot partition of the violin plots represent the median (circle) and interquartile ranges. Dashed horizontal lines represent the aggregated modes per tissue type and treatment. On the right side, semi-transparent colour-matched aggregated lifetime distributions are shown. Colours correspond to the predominant spectrum in the PLIM images. (g, h) Line

profile analysis of the variability and interdependence of the intensity and lifetime values across the brain tissue samples (exemplified by a red dotted line in (a)); three-line profiles in three brain samples were analysed in total. In (h), all measured values are shown as single data points normalised to the mean; average deviations (in a.u.) were: for intensity signals—0.287, 0.076 and 0.159; for lifetime values-0.097, 0.057 and 0.124. (i) Tissue photograph, phosphorescence intensity of the probe and PLIM images of cortex slices are shown. Scale bars show object dimensions. Rainbow false colours in (b, d, i) are used to visualise the range of lifetime values (Sen, Zhdanov, Bastiaanssen, et al., 2020).

The phosphorescence intensity and PLIM images in Figure 5.3a-d reveal efficient surface staining with NanO2-IR for the two tissues. The colors clearly reflect the difference in lifetime values for the two tissue types and, hence, their different oxygenation, which is driven by respiratory activity. The overall variability of lifetime signals in the lung tissue was higher than in the brain due to the elevated values in sample 1, which has no conclusive explanation.

As expected, treatment of the brain tissue with AntA/NaN_3 caused a reduction in NanO2-IR lifetime (Δ-mode = 3.48 μs), indicating change in tissue oxygenation from ~150 to 200 μM upon the dual inhibition of mitochondrial cytochrome c reductase and oxidase (Figure 5.3b and e, Figure 5.4a). Similar inhibition of mitochondrial respiration in lung tissue had little effect on lifetime values (Δ-mode = 1.46 μs, Figure 5.3d and f). We attribute this to the intrinsically low respiratory activity of the lungs: the initial O_2 levels in resting tissue were close to air-saturated and could not be further increased by inhibitory treatments. The porous structure of the lung tissue has higher area of gas exchange, thus also contributing to increased tissue oxygenation.

PLIM of different surface-stained samples of the same tissue (e.g. samples 1, 2, and 3 of the brain, Figure 5.3e) or the same sample at different time points (sample 1 of the brain, not shown) produced consistent lifetime values with moderate variability, which was lower than the variability of intensity signals, as demonstrated by analyzing line profiles across the sample (Figure 5.3g, h). We observed no correlation between intensity signals and lifetime by superimposing the data obtained from all of the intensity and PLIM images (Figure 5.4b). The higher uniformity of lifetime values and their independence from the measured phosphorescence signals indicate that lifetime was not affected by the variability in tissue staining efficiency (Suhling et al., 2015). Based on these results, we

conducted PLIM of freshly dissected brain cortex slices (~1 cm^2, ~1 mm thick), surface-stained with NanO2-IR (Figure 5.3i). The observed lifetime values (ranging from ~20-25 µs) suggested that differences in local oxygenation are driven mainly by the respiratory activity of particular areas of the tissue.

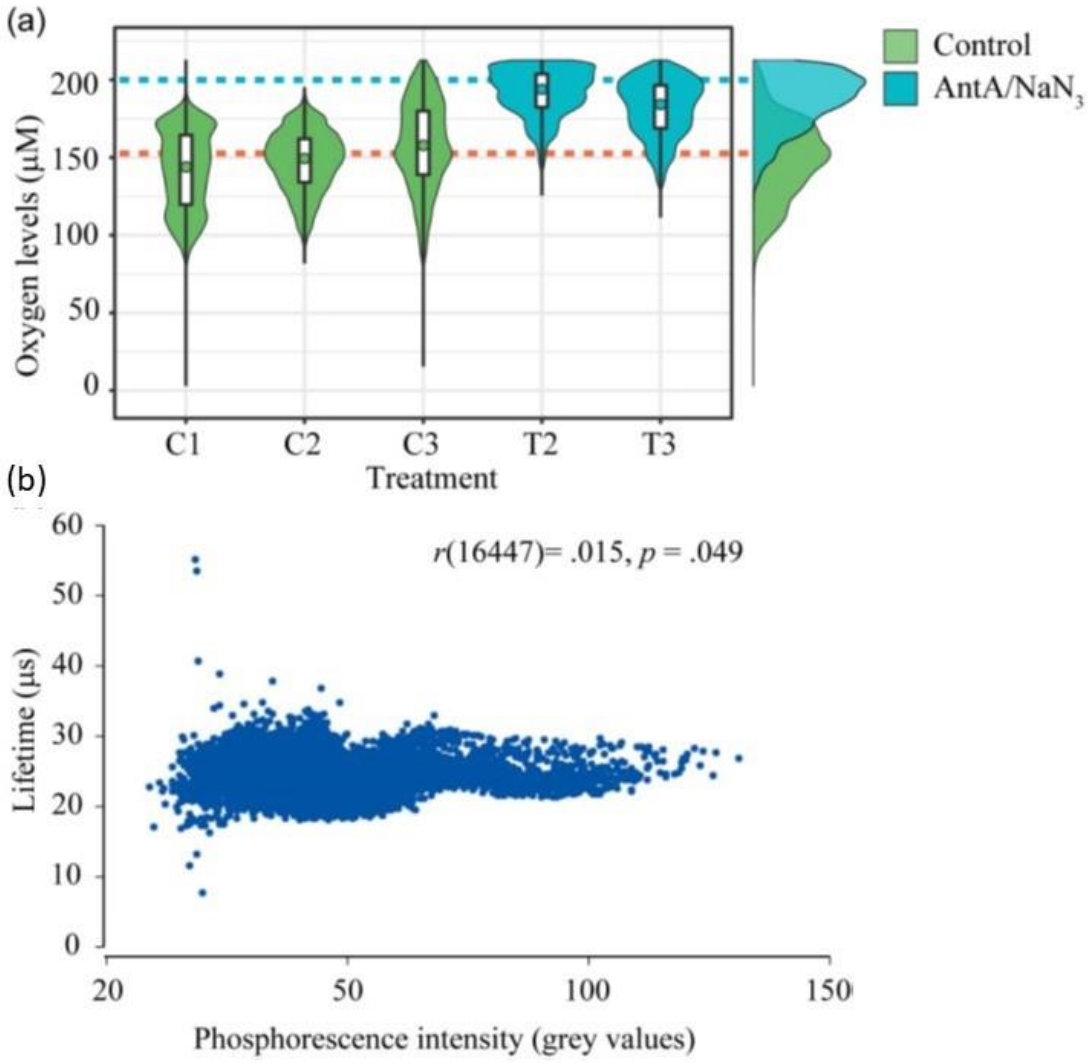


Figure 5.4: (a) Imaging of oxygenation in ex-vivo samples of mouse tissue: effects of tissue type, treatment and O_2 availability. O_2 levels in the normally respiring brain tissue surface-stained with NanO2-IR, and in the tissue with inhibited mitochondrial respiration (AntA/NaN_3). O_2 levels are calculated from lifetime values shown it Figure 5.3e. Violin plots show: on the Y-axis – the distribution of O_2 values; on the X-axis – relative frequencies of given O_2 values. Colours correspond to the predominant spectrum in the PLIM images. Box-plot partition of the violin plots represents the median and interquartile ranges. Dashed horizontal lines represent the aggregated modes for the different tissue type, treatment or staining method. On the right side, semi-transparent colour-matched aggregated distributions are shown. (b) Dependence of the calculated lifetime values on measured phosphorescence intensity signals. Pearson correlation

analysis of the PLIM and intensity images of a surface-stained brain sample (Sen, Zhdanov, Bastiaanssen, et al., 2020).

The results concluded that the surface staining of the two tissue types with NanO2-IR works reasonably well and the PLIM imager enables fast visualization of O_2 levels at tissue/media interface. As expected, the O_2 concentrations were close to ambient O_2 levels, with the interquartile range ~125-175 µM in the brain and ~170-200 µM in the lung (Figure 5.4a). The magnitude of responses to mitochondrial modulators was proportional to respiratory activity of the tissue.

5.1.3. Deep tissue staining and imaging using NanO2-IR probe

To probe O_2 levels deeper inside tissue, we injected 1 µl of NanO2-IR (1 µg of the probe) into the lumen of excised samples of large and small mouse intestine (Figure 5.5). In this case, the probe was shielded from the detector by 0.2-0.25 mm thick intestinal wall (Abdelrahman et al., 2012). It was contained inside the intestine and reported on O_2 levels in the lumen and at the surface of mucosa. A separate series of intestinal samples were also surface-stained and imaged as described before.

Comparison of the PLIM images recorded from the mucosal and serosal sides of the small and large intestine revealed pronounced differences. For intraluminally stained samples, the lifetime distribution histogram markedly shifted towards larger values compared to the surface-stained tissue (for the colon, Δ-mode = 10.45 s, Figure 5.5i, Table 5.2). This indicated a lower oxygenation of the inner areas of the intestine (Figure 5.6). The intraluminally stained samples with inhibited mitochondrial respiration showed largely reduced lifetime values, compared to the untreated samples (Δ-mode = 4.45 µs and 3.93 µs for the small and large intestine, respectively; Figure 5.5c, e; Table 5.2). Still, lifetime signals were not uniform and did not correspond to a fully oxygenated state (refer to calibration in Figure 5.2), most likely because respiration in the surrounding tissue was not fully inhibited by the slowly diffusing drugs. Non-mitochondrial, AntA/NaN_3-independent respiration could also contribute to the residual tissue deoxygenation (Pircalabioru et al., 2016). Detailed oxygenation maps of the colonic tissue samples are shown in

supplementary Figure S.0.1. Also, a comparison between the non-treated intraluminally stained samples from the two anatomically distinct regions of the intestine showed larger lifetime values for the colon compared to the small intestine, suggesting deeper colonic deoxygenation (Δ -mode = 10.13 µs, Figure 5.5c, e, g, h).

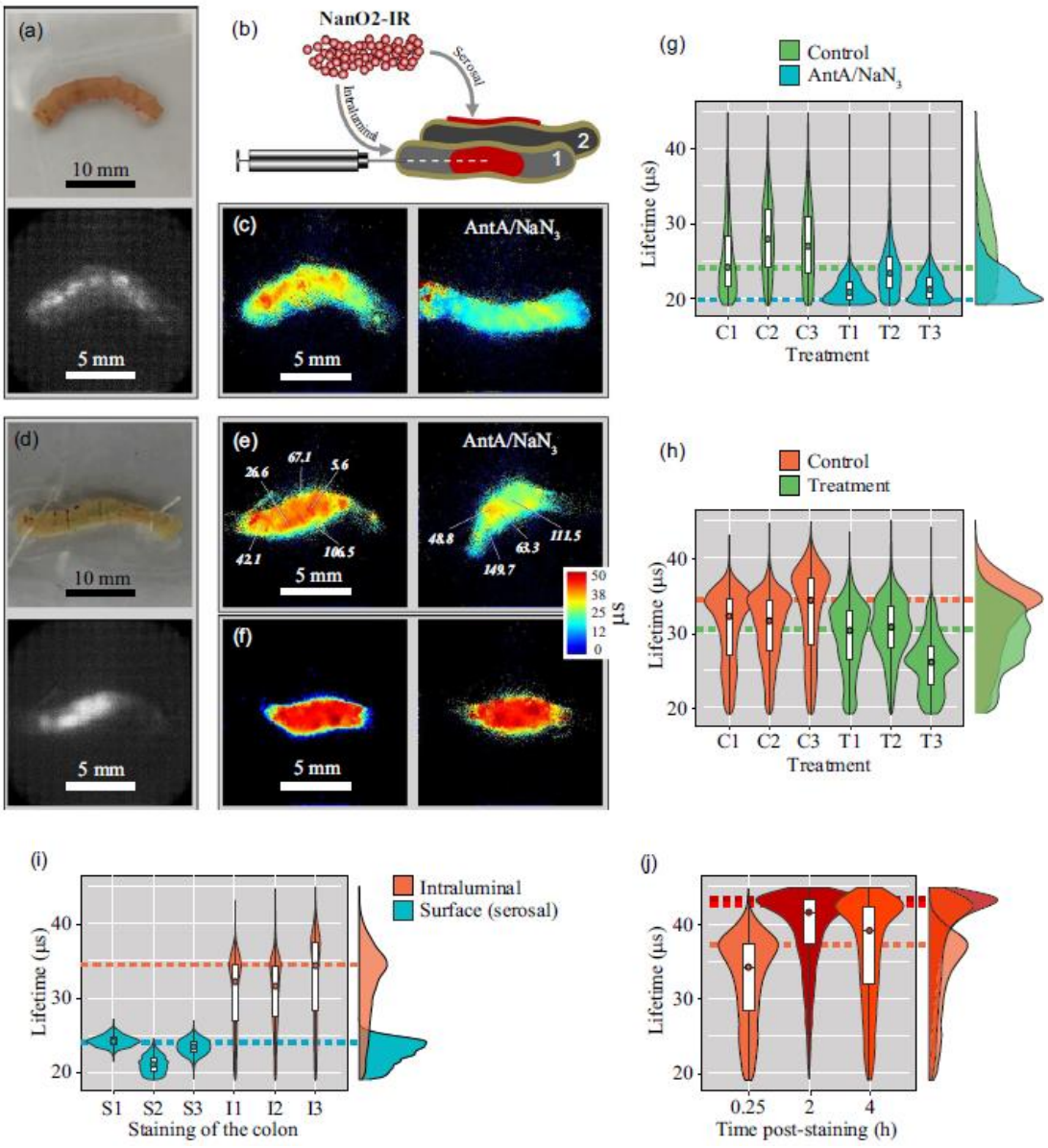


Figure 5.5: PLIM of O_2 in the intraluminally stained mouse intestine samples. Photographs and phosphorescence intensity images of the small (a) and large (d) intestine stained for 15 min with NanO2-IR by intraluminal injection (1 mg/ml, 1 µl) as shown in (b); a separate set of samples was surface-stained in parallel. Typical PLIM images of the small (c) and large (e) intestine in the respiring state (left) and upon mitochondrial inhibition for 15 min by 10 µM AntA and 0.1% NaN3 (right). In (e), selected localised O_2 concentrations (in µM) are shown in italic (see also Figs. S1 and S3). (f) PLIM images of the colon sample (e), collected 2 h and 4 h after the NanO2-

IR injection. Lifetime frequency histograms in samples of the small (g) and large intestine (h) with normal and inhibited mitochondrial respiration. (i) Comparative analysis of lifetime frequencies in the colon samples stained with NanO2-IR intraluminally and topically on the serosal side. (j) Lifetime frequency histograms corresponding to the colon sample are shown in (e, f): lifetime images are taken 15 min, 2 h and 4 h post injection. PLIM images are prepared using rainbow false colours. In (g–j), violin plots show the distribution of lifetime values along the Y-axis against relative frequencies, with which these values were recorded in individual samples (X-axis). Box-plot partition of the violin plots demonstrates the median (circle) and interquartile ranges. Dashed horizontal lines show the aggregated modes per tissue type / staining protocol / treatment. On the right side, semi-transparent colour-matched aggregated lifetime distributions are shown. Colours correspond to the predominant spectrum in the PLIM images (Sen, Zhdanov, Bastiaanssen, et al., 2020).

Aiming to examine the stability of lifetime signals and respiratory activity of the intestinal tissue, we also conducted time-lapse PLIM analysis of intraluminally stained colon samples over 4 hours. We observed a significant increase in lifetime values between 15 minutes and 2 hours of incubation (Δ-mode = 6.09 µs), which reflected the reduction in O_2 levels in the luminal part of the intestine. No further changes in lifetime values / oxygenation occurred between 2 and 4 hours of incubation. The mode value of ~43 µs corresponded to almost complete deoxygenation (~1 µM O_2), with Δ-O_2 = ~140 µM between the serosal and mucosal sides. We think that the lower lifetime values at 15 minutes reflect the partial reoxygenated lumen during NanO2-IR injection with a Hamilton needle (Φ = 0.72 mm), which transiently enabled O_2 access to the lumen (Figure 5.5b, e, f, j). Since O_2 levels remained very low for at least 4 hours, we also conclude that tissue sustained respiration over the whole period of manipulation, including the dissection, preparation, staining, incubation and imaging procedures.

The NanO2-IR probe was also subcutaneously injected into intact tissue of freshly sacrificed mice. The selected areas of the tail and paw were thicker (~0.5 mm (Liakath-Ali et al., 2014; Press et al., 2017)) and less light-permeable than intestinal wall. So, the first attempt with 1 µl injection of NanO2-IR failed to produce enough signals under the same imaging setting as above. However, when the injection volume was raised to 5 µl (5 µg of the probe), NanO2-IR was successfully imaged and PLIM produced high lifetime values both in the tail and the paw (Figure 5.7, Table 5.2). These PLIM findings are in agreement with the

current knowledge about deep or even complete deoxygenation of tissues with interrupted O_2 supply, as exemplified by the brain tissue after clinical death (Smith et al., 2007).

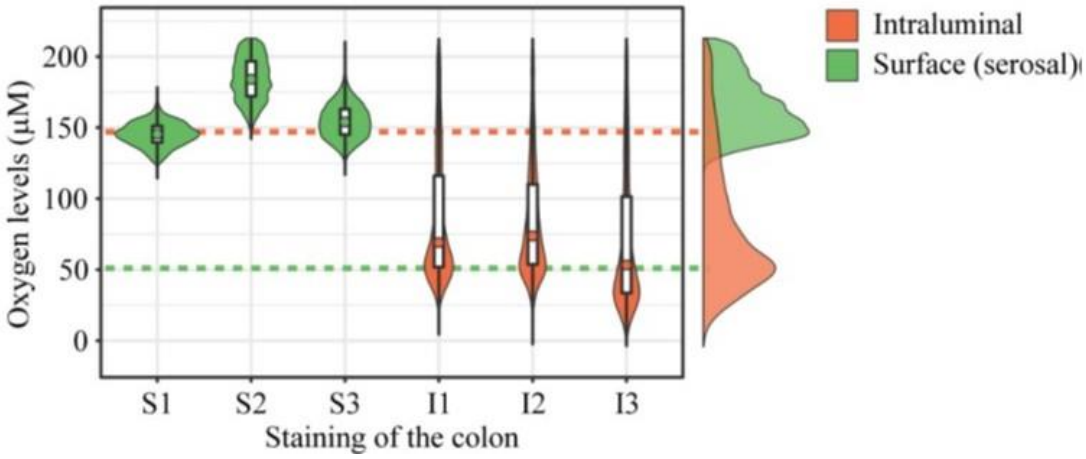


Figure 5.6: Imaging of oxygenation in ex-vivo samples of mouse tissue: effects of tissue type, treatment and O_2 availability. O_2 levels on the outer, serosal side of the colon (surface-stained) and inside the lumen or on the inner, mucosal surface. O_2 levels are calculated from lifetime values shown it Figure 5.5i. Violin plots show: on the Y-axis - the distribution of O_2 values; on the X-axis - relative frequencies of given O_2 values. Colours correspond to the predominant spectrum in the PLIM images. Box-plot partition of the violin plots represents the median and interquartile ranges. Dashed horizontal lines represent the aggregated modes for the different tissue type, treatment or staining method. On the right side, semi-transparent colour-matched aggregated distributions are shown (Sen, Zhdanov, Bastiaanssen, et al., 2020).

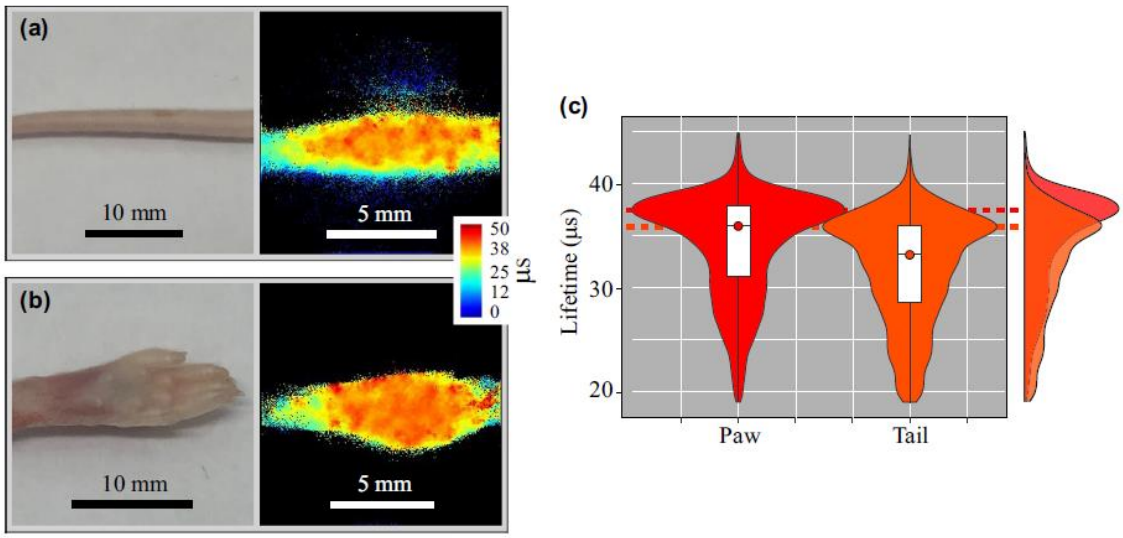
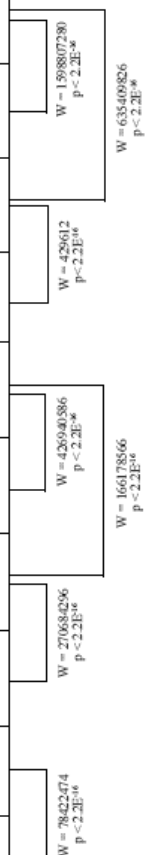


Figure 5.7: PLIM of O_2 in the subcutaneously stained tail (a) and paw (b) of a mouse (post mortem). On the left, photographs and PLIM images are shown. Rainbow false colours demonstrate the range of lifetime values. (c) Lifetime frequency distribution calculated from (a) and (b); violin plots show the distribution of lifetime values along the Y-axis, and relative frequencies, with which these values were obtained (X-axis). Box-plot partition of the violin plots demonstrates the median (circle) and interquartile ranges. Dashed horizontal lines show the aggregated modes for each tissue type. On the right side, semi-transparent colour-matched aggregated lifetime distributions are shown (Sen, Zhdanov, Bastiaanssen, et al., 2020).

Table 5.2: Characteristics of lifetime values measured ex vivo in mouse tissues

Tissue / Staining	Sample /Treatment	Median	Interquartile range	Mode
Brain / surface-stained	C1	24.25	3.94	23.42
	C2	23.78	2.4	
	C3	23.08	3.36	
	T1 / AntA/NaN_3	NA	NA	19.93
	T2 / AntA/NaN_3	23.08	1.54	
	T3 / AntA/NaN_3	21.02	2.07	
Lung / surface stained	C1	21.32	2.08	20.51
	C2	20.27	1.53	
	C3	19.67	0.9	
	T1 / AntA/NaN_3	NA	NA	19.05
	T2 / AntA/NaN_3	19.05	0.05	
	T3 / AntA/NaN_3	19.42	0.3	
Small intestine / intraluminal	C1	24.2	6.44	24.26
	C2	27.96	7.54	
	C3	26.92	7.58	
	T1 / AntA/NaN_3	21.06	2.39	19.81
	T2 / AntA/NaN_3	23.56	4.27	
	T3 / AntA/NaN_3	20.91	2.96	
Large intestine / intraluminal	C1	32.13	7.65	34.39
	C2	31.53	6.77	
	C3	34.28	8.99	
	T1 / AntA/NaN_3	30.21	6.62	30.46
	T2 / AntA/NaN_3	30.68	5.55	
	T3 / AntA/NaN_3	25.95	5.18	
Large intestine / surface-stained *vs* intraluminal	S1	24.13	1.01	23.95
	S2	21.02	1.83	
	S3	23.4	1.5	
	I1	32.13	7.65	34.39
	I2	31.53	6.77	
	I3	34.28	8.99	
Large intestine time lapse	15 min	34.28	8.99	37.2
	2 h	41.68	6.05	43.29
	2 h	39.2	10.39	42.5
Paw-Tail	Paw	35.99	6.76	37.57
	Tail	33.23	7.47	35.97



5.2.*In-vivo* imaging of live and sacrificed animals

The novel Tpx3Cam imager was used in a minimally invasive method to track tissue oxygenation in developing grafted tumours. CT26 cells stained with NanO2-IR probe were injected to mice to generate grafted tumours with phosphorescence characteristic. The tumours were allowed to develop for 3, 7, 10 and 17 days, with O_2 imaging experiments performed on live and euthanised animals at different time points. After the *in vivo* and post mortem O_2 imaging with animals, tumours were excised, fixed, sliced on a vibratome and then

examined on a confocal PLIM microscope for the presence and distribution of the probe.

5.2.1. Optimisation of NanO2-IR probe delivery and tumour growth

First, we optimized the conditions for delivery of the NanO2-IR probe in mice and its incorporation in the tumours produced by the subcutaneous injection of CT26 cells. For that, we examined cell staining and toxicity effects of the probe on cultured cells, and optimised conditions for producing grafted tumours stained with NanO2-IR. This allowed us to choose the staining concentration of NanO2-IR for cell staining that produce measurable phosphorescence during tumour growth, which was monitored for up to 17 days.

The CellTiterGlo® cytotoxicity assays did not show major effects on cells of the NanO2-IR probe used at concentrations 0-200 µg/ml and incubation time 18 hours (Figure 5.8a). However, microscopy analysis showed some long-term effects of NanO2-IR. The cells treated with >50 µg/ml probe for 20 hours did not proliferate and died within 20–30 hours of the staining (Figure S.0.2A). Even at 50 µg/ml, the probe strongly reduced cell proliferation rate, which gradually increased with decreasing NanO2-IR concentrations.

These in vitro results suggested that development of tumours from cells pre-stained with NanO2-IR at >50 µg/ml, or even lower concentrations, could be problematic. Therefore, we tested proliferation of 1:1 mixtures of non-stained and stained cells at different NanO2-IR concentrations. This method markedly improved cell proliferation *in vivo*. Even in the presence of cells stained with 200 µg/ml NanO2-IR, the non-stained cells grew and formed tumours (Figure S.0.2B). So, the injection of a mixture of stained and non-stained cells produced efficient tumour growth and adequate amount of probe in the tumour tissue. Alternatively, non-stained cells combined with NanO2-IR were also administered just before the injection.

Next, the efficiency of cell staining at different NanO2-IR concentrations were examined. When analysing phosphorescence of NanO2-IR in the stained CT26 cells on a confocal PLIM microscope, we noticed that intensity signals do not increase proportionally with probe concentration used for the staining. Thus,

when NanO2-IR levels in the medium increased from 25 µg/ml to 200 µg/ml, signals produced by cells increased by less than 50% (Figure 5.8b, c).

When used at concentrations of 25–200 µg/ml, NanO2-IR produced constant lifetime values and strong and sustained intensity signals in cells which were useful for the analysis of tissue oxygenation in mice on the PLIM macro-imager (Figure 5.8d). To prove this, we injected the cells with the probe in the right flank of freshly sacrificed animals, and then imaged the areas. Three different methods were used to deliver the NanO2-IR probe into animal tissue at three different concentrations (25, 50, and 100 µg/ml): i) non-stained cells mixed with the probe; ii) cells stained with the probe; and iii) 1:1 mixture of the non-stained and stained cells. For the first two methods, post-mortem animals were injected and images were taken within 20 minutes. For the third technique, live animals were injected and images were taken on days 4, 7, and 10 of the tumour growth. Figure 5.8e shows PLIM images for the different methods of delivery at three different concentrations of NanO2-IR probe. Figure 5.8f shows the corresponding lifetime values, and that the 1:1 mixture of non-stained and stained cells produced the most stable lifetime signals at all three concentrations. Based on the results of cell staining, analysis of proliferation, and post-mortem animal imaging, injection of 1:1 mixture of stained cells (stained with 50 µg/ml probe) and non-stained cells were chosen for the *in vivo* imaging experiments (Figure 5.9a).

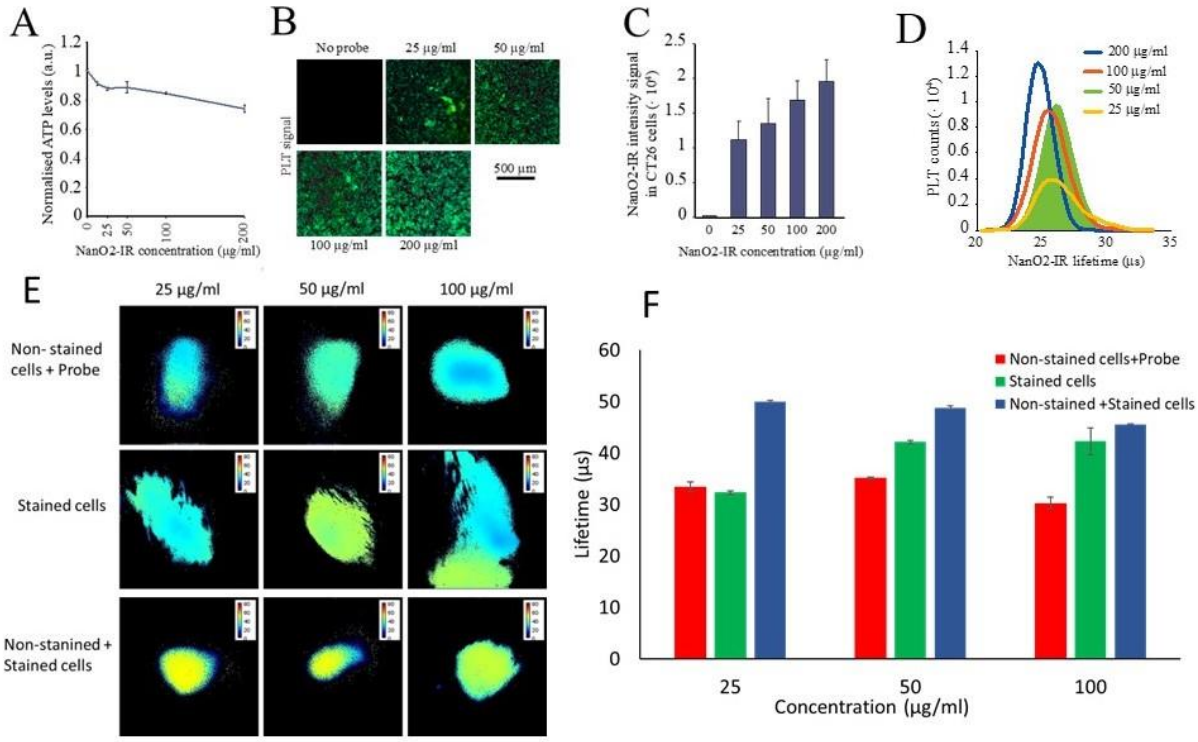


Figure 5.8: Optimisation of NanO2-IR delivery to grafted tumours in mice. (a) Effects of the different concentrations of NanO2-IR probe (indicated, incubation time 18 h) on the viability of cultured CT26 cells. Analysed with a CellTiter-Glo® kit which measures total cellular ATP levels. (b, c) Confocal microscopy analysis of staining efficiency of CT26 cell at different concentrations of NanO2-IR (18 h). (d) Distribution histogram of lifetime values, calculated for the cells stained with different concentrations of NanO2-IR (as in b, c). (e) PLIM images of tumour tissue produced by different means of NanO2-IR delivery. (f) Bar charts comparing probe lifetime values for the different trials.

5.2.2. *In vivo* and post-mortem analysis of O_2 levels in tumours

The O_2 imaging analysis in live animals was performed on days 3, 7, 10, and 17 of the tumour growth (Figure 5.9a). Grafted tumours stained with NanO2-IR were seen to grow two times slower than those produced with unstained CT26 cells (Figure 5.9b). This is in agreement with the toxic effects of the probe. By day 17, tumour size reached to 0.12 cm^3, compared to 0.23 cm^3 for the control group. Figure 5.9c shows that the tumour regions were easily visible on the intensity images at all stages of tumour growth, enabling accurate calculation of phosphorescence lifetime values. The lifetime values ranged between 44-52 µs on the different days of tumour growth (Figure 5.9d). However, analysis of the

PLIM data (Figure 5.9d) did not show any significant trends in tumour growth: lifetime values in living animals ranged from ~44 µs (days 3 and 17) to ~46 µs (days 7 and 10). Also, the repeated measures ANOVA test did not show significant difference in lifetime values between PLIM images of live and post-mortem tumour tissue taken during each day of tumour growth. The ANOVA test also showed a trend toward higher lifetime values in euthanized animals compared to live animals (see statistical details in Figure 5.9). The trend was stronger for day 17, with p = 0.131 for live vs dead mice. It is understood that when blood circulation stops shortly after death, tissue O_2 rapidly depletes. Little difference in NanO2-IR lifetime values between the live and euthanized animals revealed that tissue oxygenation was relatively low at all stages of tumour progression, including the initial 3 to 7 days when tumours were not palpable (Figure 5.9b). This early-stage effect can be caused by local inflammation, which is known to induce tissue hypoxia.

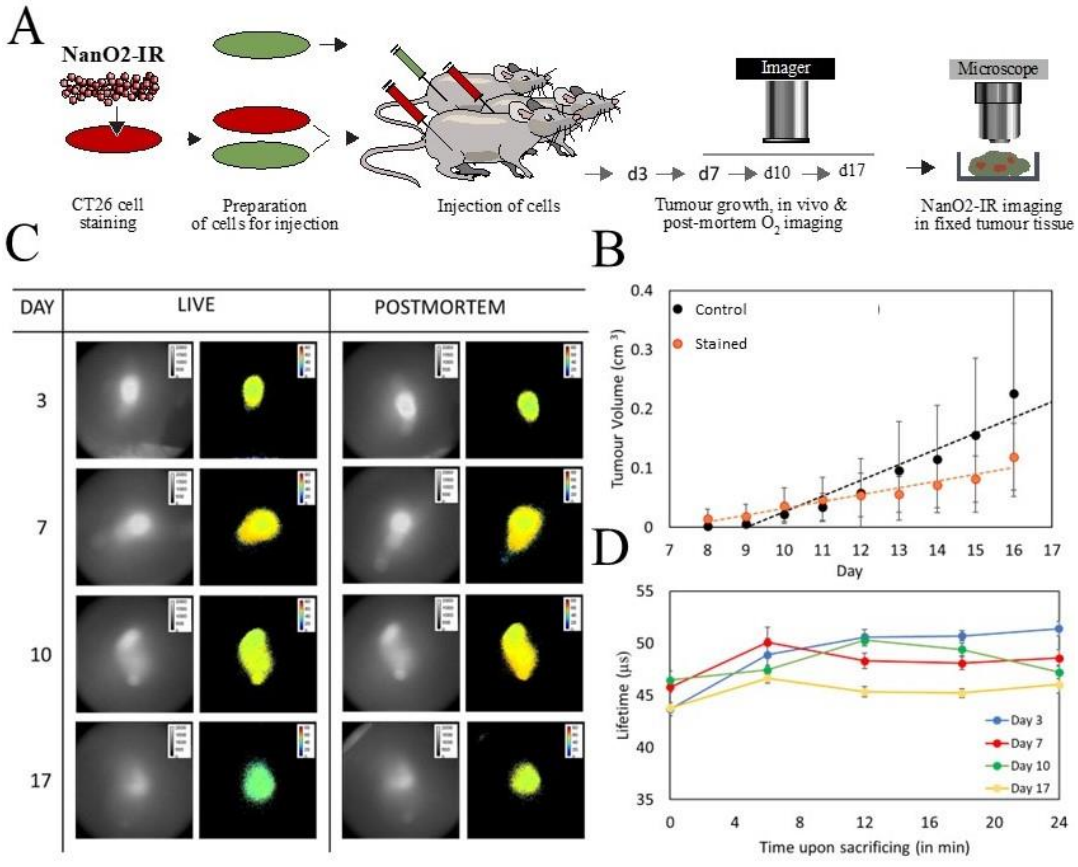


Figure 5.9: Imaging analysis of tumour oxygenation. (a) The scheme of in vivo and post-mortem O_2 imaging of tumour tissue of mice. CT26 cells stained with NanO2-IR (50 mg/ml, 18 h) were mixed with non-stained CT26 cells (1:1) and injected in mice subcutaneously (right flanks); tumours were allowed to grow for up to 17 days, and then were analysed on the Tpx3Cam PLIM

imager on days 3, 7, 10 and 17 in vivo and immediately after animal death. After this NanO2-IR distribution was analysed in fixed tumour tissues on the confocal PLIM microscope. Animals in control group (tumour size and phosphorescence background controls) were injected with non-stained CT26 cells. N=6 in all animal groups. (b) Comparison of the growth rate of the control and stained tumours. (c) Intensity and PLIM images of the live and euthanised animals on different days of tumour growth. (d) The LT values in tumour regions of live and euthanised animals, taken with 6 min intervals on the different days of tumour growth (N=3 in each group).

Statistical analysis

The repeated measures ANOVA test was performed on the lifetime values recorded on the different days (shown in Figure 5.9d), which shows:

a) On day 3, for different imaging time F(1.05, 2.1) = 1.89, p = 0.301, with a mean of 43.7 µs for 0 min, 48.9 µs for 6 min, 50.59 µs for 12 min, 50.7 µs for 18 min, 51.38 µs for 24 min. F = 5.2, p = 0.3857 for 0 min vs 6 min; F = 6.889, p = 0.2672 for 0 min vs 12 min; F = 6.999, p = 0.3215 for 0 min vs 18 min; F = 7.684, p = 0.2839 for 0 min vs 24 min.

b) On day 7, for different imaging time, F(1.45, 2.89) = 2.44, p = 0.232, with a mean of 45.8 µs for 0 min, 50.1 µs for 6 min, 48.3 µs for 12 min, 48.1 µs for 18 min, 48.6 µs for 24 min. F = 4.274, p = 0.2143 for 0 min vs 6 min; F = 2.515, p = 0.1808 for 0 min vs 12 min; F = 2.298, p = 0.165 for 0 min vs 18 min; F = 2.783, p = 0.2031 for 0 min vs 24 min.

c) On day 10, for different imaging time F(4, 8) = 2.24, p = 0.154, with a mean of 46.5 µs for 0 min, 47.4 µs for 6 min, 50.3 µs for 12 min, 49.4 µs for 18 min, 47.2 µs for 24 min. F = 0.951, p = 0.2469 for 0 min vs 6 min; F = 3.8277, p = 0.144 for 0 min vs 12 min; F = 2.928, p = 0.2507 for 0 min vs 18 min; F = 0.7453, p = 0.5331 for 0 min vs 24 min.

d) On day 17, for different imaging time, F(1.8, 3.59) = 3.79, p = 0.131, with a mean of 43.8 µs for 0 min, 46.7 µs for 6 min, 45.3 µs for 12 min, 45.2 µs for 18 min, 46.0 µs for 24 min. F = 2.85, p = 0.0746 for 0 min vs 6 min; F = 1.5387, p = 0.0214 for 0 min vs 12 min; F = 1.4177, p = 0.1182 for 0 min vs 18 min; F = 2.2347, p = 0.1981 for 0 min vs 24 min.

5.2.3. Analysis of NanO2-IR distribution in tumour tissue

The localization of NanO2-IR in tumour tissue was also studied. For this, the tumour slices were examined on a confocal PLIM microscope for the presence and distribution of the probe. Tissue regions containing NanO2-IR probes could be detected visually as dark spots (Figure 5.10a). Further analysis confirmed the presence of NanO2-IR in these "isles", surrounded mostly by non-stained tissue or tissue with low concentrations of the probe dispersed diffusely. This uneven distribution of the probe suggested that stained CT26 cells died soon after

injection, and their debris forms these 1-3 mm-sized "isles" of NanO2-IR probe. These "isles" were surrounded by non-stained cells which actively proliferated and produced tumours similar in size of the control (non-stained) tumours.

The lifetime signals across the stained "isles" were also examined using 3D image reconstructions. The results showed that they were unaffected by the probe concentration and aggregation (Figure 5.10b, c). The size and average intensity signals from the NanO2-IR "isles" were unaffected by the tumour growth and were similar to the tumour samples collected on days 10 and 17 (Figure 5.10d, Figure S.0.3). The median lifetime values in the tissues at different stages of tumour growth were between 22–24 μs and did not vary. After chemical deoxygenation, the lifetimes increased to >40 μs. This confirms the accuracy of the phosphorescent signals recorded from the probe, which were unaffected by sample preparation, including fixation with paraformaldehyde (Figure 5.10e).

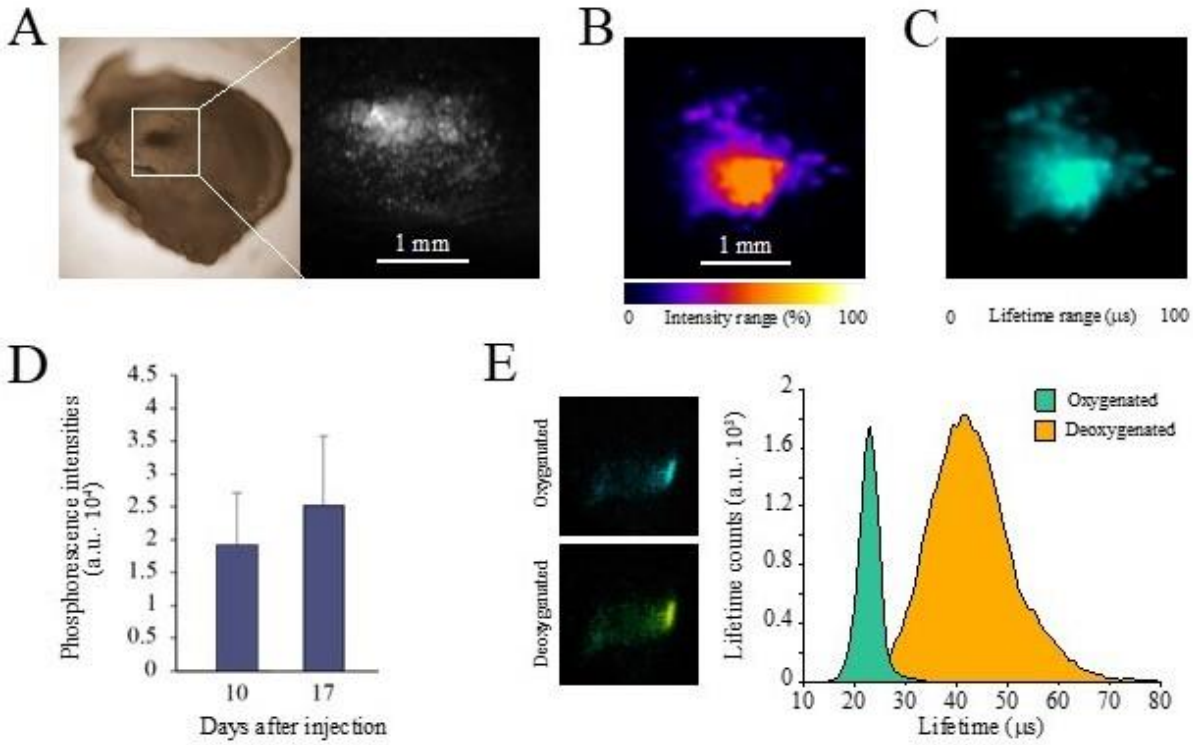


Figure 5.10: Analysis of NanO2-IR localisation in tumour tissue. (a) Representative image of tumour tissue with NanO2-IR 'isle' positioned in the middle (left). The corresponding phosphorescence intensity image obtained by confocal PLIM microscopy (right, 5x magnification). (b, c) Typical span of the phosphorescence intensity signals across the NanO2-IR 'isle' (B) and the corresponding lifetime values (c). (d) Analysis of the intensity signal of NanO2-

IR residing in tumour tissue at different stages of tumour development. (e) Response of NanO2-IR 'isle' to chemical deoxygenation of the tissue by sulphite. Right panel shows the typical shift of the distribution of lifetime values in response to decreased O_2 levels. Images represent stacks of six (a-c) or three (e) focal planes taken in 5 µm step.

5.3. Conclusions

The Tpx3Cam imager demonstrated fast, high-resolution O_2 imaging in sizable biological samples, including liquid samples with respiring cells, live post-mortem animal tissue, and complete organs, passively stained with NanO2-IR probe on the surface or microinjected in tissue depth. To prevent adverse effects of the NanO2-IR probe on the live tissue samples within 1 hour of imaging, tissue staining and PLIM techniques were optimized. Tissues also maintained respiratory activity for at least 4 hours following isolation. The imager allowed accurate lifetime measurements of the probe and generated detailed O_2 concentration maps for tissue surface/interface and deeper areas, the latter imaged through 0.2-0.5 mm thick tissue layers. The ability of the imager to measure the changes in lifetime signal upon mitochondrial inhibition (decrease in lifetime) or after moving deeper into tissue (increase in lifetime), supported its potential use in physiological studies with *in vivo* models (live or anesthetized animals).

The imager and the probe were used to demonstrate their performance in rapid quantitative imaging of tissue hypoxia in animal models with grafted tumours. The NanO2-IR staining conditions in animals were optimized to minimise the negative effects of the probe on grafted tumours and enable long-term retention of the probe in grafts. The imager produced accurate lifetime maps that showed hypoxic conditions in tumour regions, both in living and euthanized animals. The lifetime values measured in live animals from day 3 to day 17 of tumour growth were in line with previous studies demonstrating profound hypoxia in the tumour tissue. Confocal PLIM microscopy of tissues samples excised on days 3–17 showed the distribution of the NanO2-IR probe in the tumours and its lifetime signal in oxygenated and deoxygenated conditions. Compared to the other O_2 sensitive phosphorescent probes intended for intravital use, NanO2-IR was seen to be the most long-lasting probe, which produces stable and easily detectable

intensity and lifetime signals for at least 17 days, little affected by tissue environment and tumour growth. Overall, the study showed that the new PLIM macro-imager can successfully be used in fast, high resolution, quantitative, minimally invasive method of PLIM imaging in physiological *in vivo* studies.

Chapter 6: Final Discussion

The novel fast optical imager, Tpx3Cam, designed for macroscopic wide-field PLIM applications, was constructed and integrated. By means of an opto-mechanical adapter, Cricket (Photonis) with standard C-mount connectors on both sides, the Tpx3Cam camera was coupled to an image intensifier, a 760 nm emission filter and a 50 mm lens, to allow imaging of 18 x 18 mm sample area. A super-bright LED provided pulsed excitation of the sample area and subsequent PLIM. The main working module of the resulting macro-imager had a compact size, rigid design, and flexible architecture. The Cricket adapter provided rigid optical alignment to the main components so that the imager can be rotated 360° and tuned geometrically for the analysis of different samples. The imager was mainly used in the upright orientation for all the experiments, but can also be used in inverted and side orientation.

The imager was initially characterised using planar phosphorescent O_2 sensors and a resolution plate mask. Several acquisition and image processing algorithms were evaluated and compared to optimise system resolution and performance for the wide-field PLIM. With centroiding and TOT corrections, the resolving power was found to be 12.7 lp/mm, and line width - 39.4 μm and the IRF gave a temporal resolution of 30.6 ns (FWHM). The imager temporal resolution was limited by the LED, so it can be improved by using a ps laser.

Next, we imaged a set of phosphorescent materials on the macro-imager. The near-infrared emitting O_2-sensitive PtBP dye was embedded into five polymers having different permeability for O_2 and applied as solid-state coatings on a polyester film support. These sensor materials were placed on a temperature-controlled stage and imaged under pulsed excitation with a 627 nm LED and 760 nm emission filter which are optimal for PtBP dye. The resulting PLIM images showed good uniformity, accuracy, and contrast of the lifetime values for the different phosphorescent materials. The lifetime values also changed with altered temperature or oxygenation conditions, proving the dynamic mechanism of quenching by O_2. In agreement with the literature data and our expectations, the polystyrene and PtBP based sensors showed the highest sensitivity to the changing macro-environment, whereas the lowest sensitivity was observed in the

PVDC sensors. Several other commercial and non-commercial O_2 sensors based on PtBP and PtOEPK dyes were also imaged and their imaging results were consistent with previously published data.

A series of PtOEP based O_2 sensors were also measured. In this case, the LED and emission filter were replaced with a 390 nm LED and a 648 nm bandpass emission filter and the LED parameters were optimised. For these sensor materials, high background signals from the support material and afterglow or autofluorescence under UV excitation resulted in inaccurate lifetime values. To overcome this, the decay fitting parameters were further optimised to minimise these measurement artefacts.

Lifetime measurements on the new imager were also compared with those performed on the confocal TCSPC-PLIM microscope. PtBP based commercial and handmade sensors showed generally consistent lifetime values on both the platforms. Although a greater variability in the lifetime signals was seen on the confocal system due to its raster scanning, the Tpx3Cam imager produced more accurate lifetime readings at a superior speed and with better quality PLIM images. But lifetime values produced by the PtOEP and PtOEP/OEPK sensors did not match, although good convergence of the results was observed for PtOEP-SB. Therefore, platform-specific calibration for each particular sensor is important for accurate analysis of sample oxygenation.

PLIM of the sensor spots with increasing dilutions showed constant lifetime signals and decreasing intensity signals which demonstrated high sensitivity and stability of the PLIM mode. Thus, we examined how variations in imaged objects, namely brightness, hosting media/LT range, environmental conditions and their changes can influence the results of the PLIM imaging and mapping of LT values and O_2 concentration.

Next, the Tpx3Cam imager was used to map O_2 concentration in various live tissue samples stained with a nanoparticle-based NanO2-IR probe. The tissues were carefully chosen to demonstrate the performance of the imager when comparing oxygenation between: 1) tissues with high and low O_2 consumption (such as brain vs. lung, or, resting vs. inhibited tissue); 2) inner and outer areas of hollow organs exposed to air (intestine); and 3) subcutaneous tissue areas imaged through a thick skin layer (tail and paws). The cytotoxic effect of the probe at 1 mg/ml was tested on cultured cells which showed no effects in the first hour of

experiment. So, all the imaging experiments on live tissues were completed within 1 hour of staining. Robust phosphorescence intensity and lifetime signals were produced by passive staining of the mouse brain, lung or intestinal tissue surface with 2 ml of NanO2-IR or by microinjecting the probe into the lumen of small or large intestine fragments, which allowed O_2 mapping in the tissue within 20 s. Inhibition of tissue respiration or limitation of O_2 diffusion to tissue produced the anticipated increase or decrease in O_2 levels, respectively. Furthermore, subcutaneous injection of 5 µl of the probe in intact paw and tail of sacrificed mice enabled efficient O_2 imaging at tissue depths of up to 0.5 mm. Overall, the imager was able to reveal an adequate span of measurable O_2 levels (0–210 µM) in *ex vivo* tissue samples with higher (e.g. the lungs or brain surface) and lower (e.g. colonic lumen or inner areas of the paw and tail) O_2 levels.

Lastly, the imager was used in a minimally invasive technique for the monitoring of tissue oxygenation in developing grafted tumours. First the probe delivery conditions were optimized. Based on the results, 1:1 mixture of CT26 cells stained with 50 µg/ml of NanO2-IR probe and non-stained cells were injected into mice to produce grafted tumours with characteristic phosphorescence. The tumours were allowed to develop for 3, 7, 10 and 17 days, with O_2 imaging experiments were performed on live and euthanised animals at different time points. Despite a marked trend towards decreased O_2 in dead animals, their tumour areas produced phosphorescence lifetime values between 44-47 µs, which corresponded to deeply hypoxic tissue. After the O_2 imaging in animals, confocal PLIM was conducted to examine the distribution of NanO2-IR probe in the tumour slices. The probe remained visible as bright and discrete ‘islands’ embedded in the tumour tissue until day 17 of tumour growth.

In conclusion, the new Tpx3Cam macro-imager demonstrated good functionality and operational performance for wide-field PLIM applications. It can image objects of several centimetres in size with high spatial resolution within 20 seconds. Along with single photon sensitivity and quantitative lifetime imaging, advantages of the platform also include flexibility, transportability, high level of technology integration and relatively low cost (< 30% of the price of a standard PLIM system). In its present form, the imager is limited to applications based on wide-field PLIM. Other limitations of the imager include the large size of its data sets (~ 2 Gb) and complex data analysis. The performance of the

imager can be improved further with the next generation Timepix4 readout chip with timing resolution of 200 ps (Llopart et al., 2022). The system performance can be further improved and extended to nanosecond FLIM mode by replacing the LED with a fast laser source.

Appendix

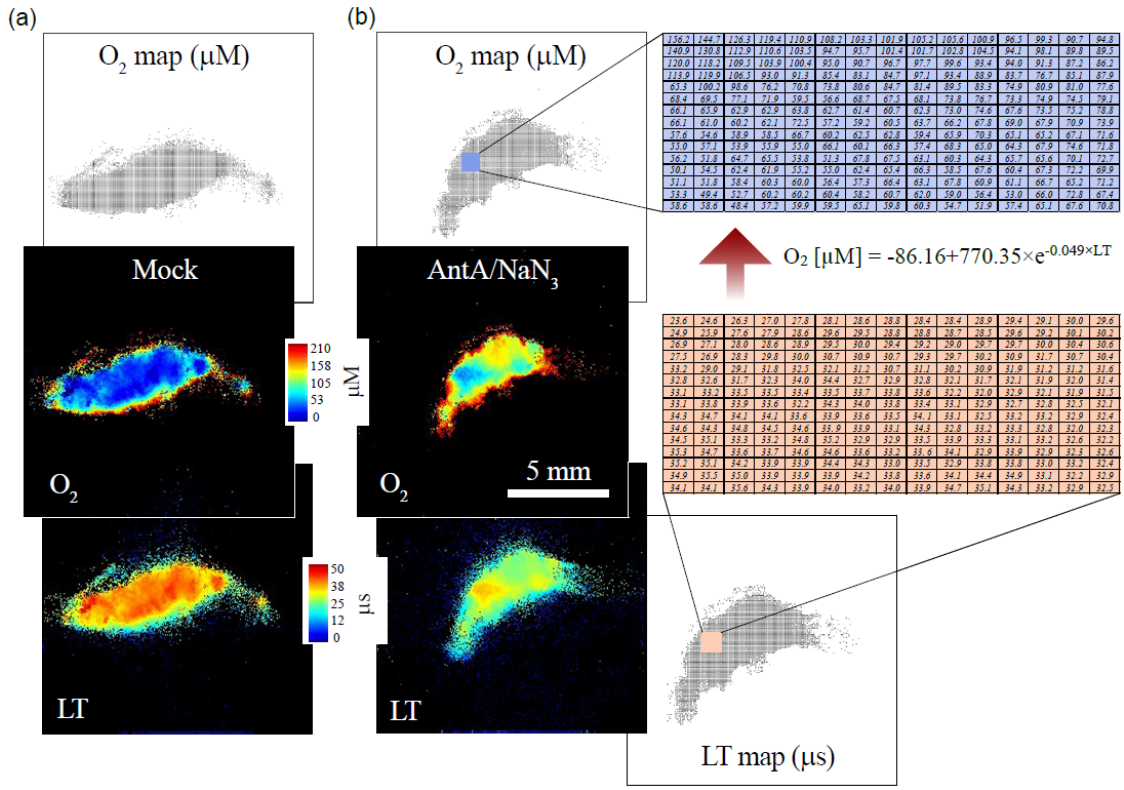


Figure S.0.1: Mapping O_2 in the lumen of mouse colon ex vivo. (a) From bottom to top, the lifetime (LT) image, O_2 image and detailed O_2 map of the lumen of mouse colon stained as described for Figure 5.5e. (b) Similar to (a) data set obtained using mouse colon treated for 15 min with AntA and NaN_3. Right panel in (b) also shows the LT map and magnified fragments of LT and O_2 maps that show the conversion of LT values (µs) into O_2 concentrations (µM) using the indicated analytical equation.

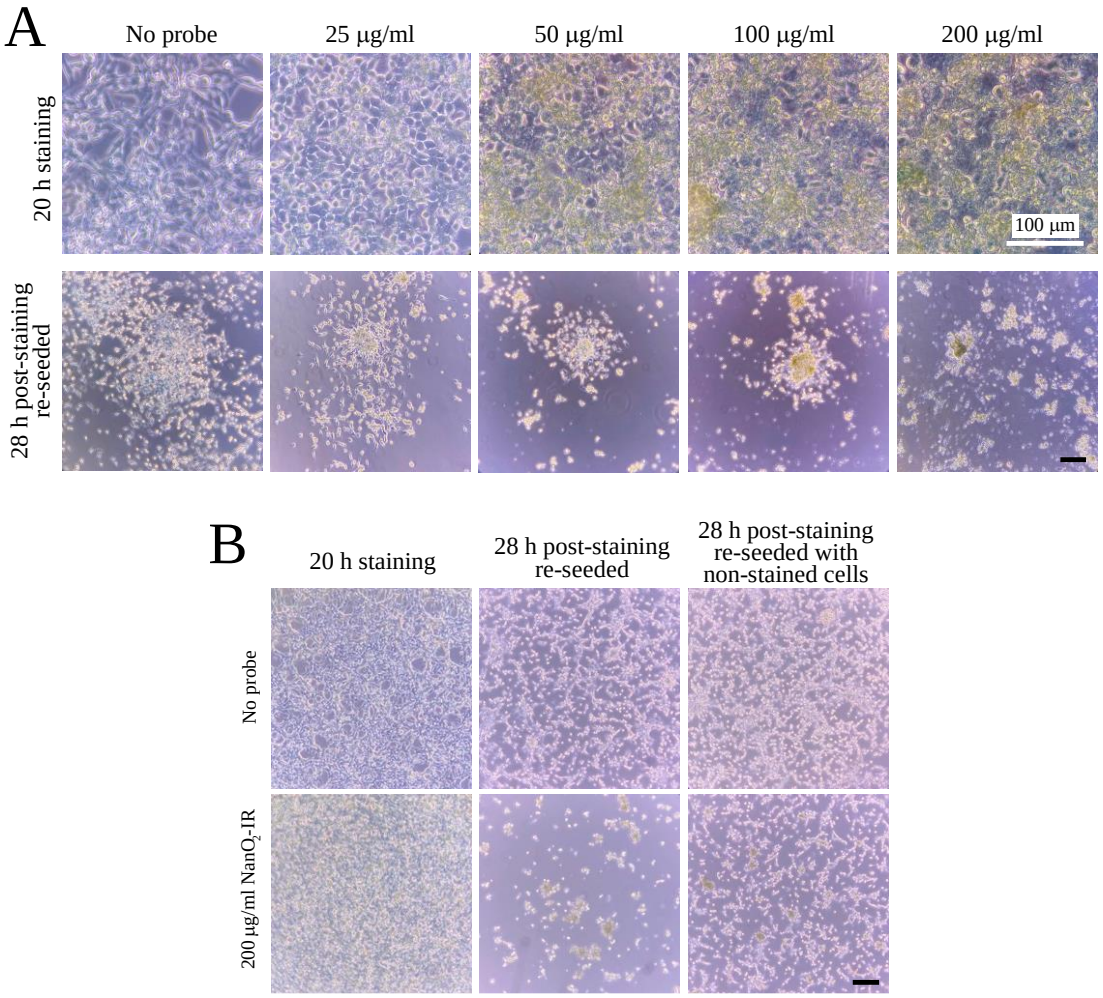
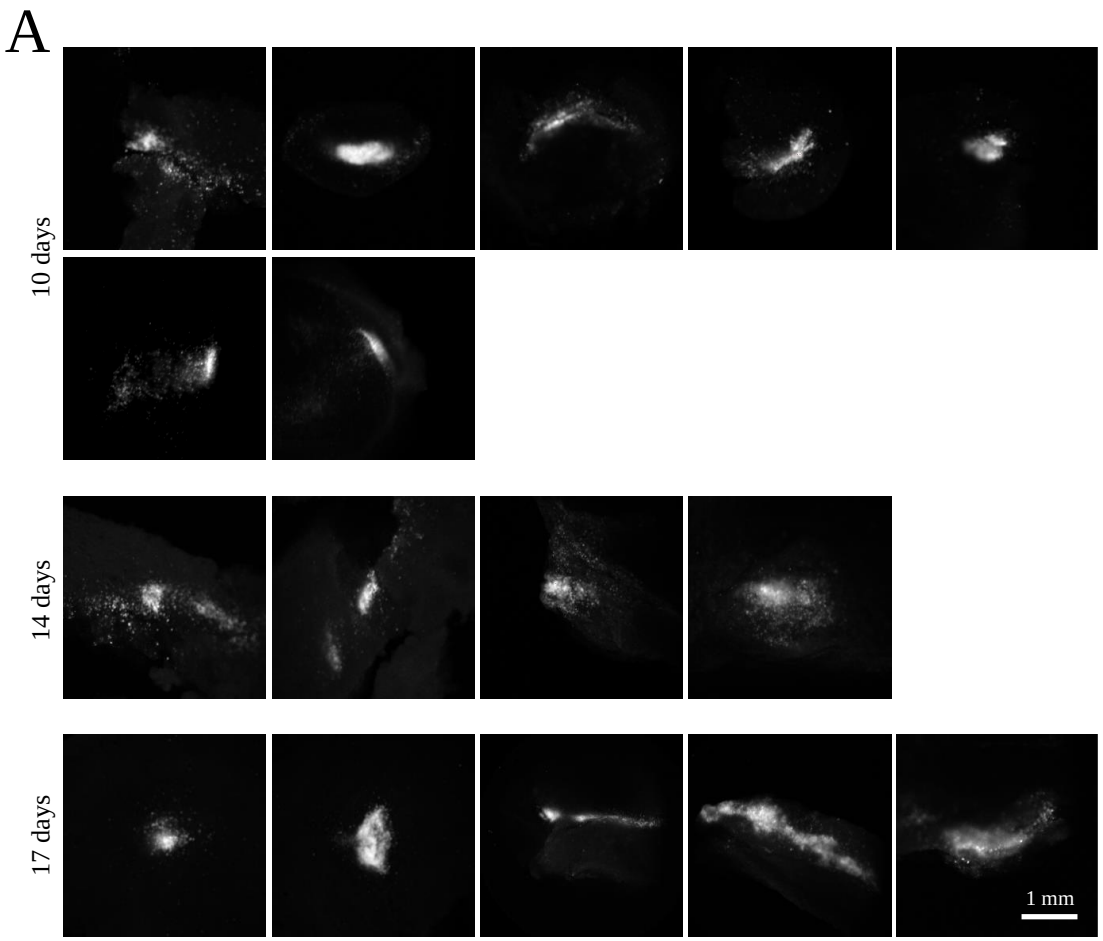


Figure S.0.2: Effects of NanO2-IR on CT26 cell proliferation capacity. A. Cells were stained for ~20 h with the probe at the indicated concentrations (top panel), washed, re-plated and grown for further 28 h (bottom panel). B. Cells stained as in (A) with 200 µg/ml probe were mixed with non-stained cells (1:1), re-plated and grown for 28 h (right panel); non-stained cells (left) and stained cells (middle) only are shown as controls for maximal and minimal proliferation, respectively. Bars indicate ~100 µm scale. Images were taken using a light microscope and iPhone camera.



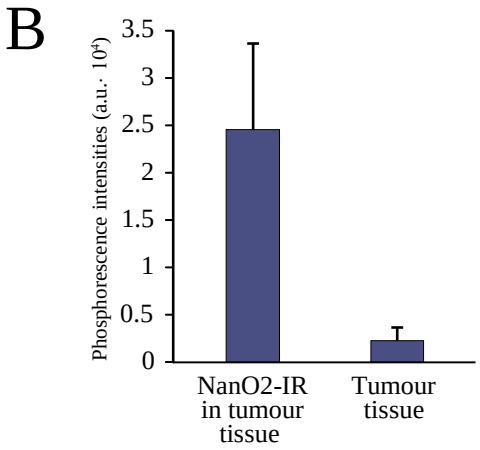


*Figure S.0.3: Analysis of NanO2-IR phosphorescence intensity in tumour tissue at different stages of tumour development. Images in (**A**) were collected using confocal PLIM microscope with 5x magnification. **B**. Quantitative analysis of NanO2-IR signals in tumour tissue (N=16, including days 10, 14 and 17); tissue with no NanO2-IR was used as background control.*

List of tables

Table 1.1: O_2 concentration in various human tissues, expressed in mmHg and in percentage of O_2 in the microenvironment 12

Table 1.2: Summary of the different O_2 detection methods..... 16

Table 1.3: Phosphorescent O_2 sensing materials and applications. 24

Table 1.4: Summary of O_2 imaging applications 47

Table 4.1: Comparison of the K_{sv}^{app} values for the different sensor materials and temperatures. 71

Table 4.2: Comparison of phosphorescence lifetime measurements on the Tpx3Cam imager and confocal PLIM microscope. 76

Table 4.3: PLT measured* on the two imaging platforms. The lifetime values (µs) were obtained from the lifetime histograms..... 78

Table 5.1: Exemplary/typical PLIM acquisition parameters used for the different tissue types and staining methods. 87

Table 5.2: Characteristics of lifetime values measured ex vivo in mouse tissues 96

List of figures

Figure 1.1: Hypoxia-inducible factor (HIF) regulation during physiological normoxia and hypoxia (J. W. Lee et al., 2019). 13

Figure 1.2: Jablonski diagram showing different photophysical processes occurring within O_2-sensitive luminescent sensors (Quaranta et al., 2012). 17

Figure 1.3: Dye structures of a few popular O_2-sensitive dyes. 19

Figure 1.4: Intensity-based detection. (a) Phosphorescence intensity spectra measurement at a single wavelength with a large Stokes' shift. (b) Principle of Time-Resolved Fluorescence (TR-F) Measurement. (c) Ratiometric measurement. Excitation and emission spectra of O_2-sensitive and reference dyes at 0 and 21% O_2. 27

Figure 1.5: Lifetime-based detection. (a) Time-domain lifetime detection; (b) Principle of TCSPC measurements; (c) Schematic presentation of the RLD method; (d) Frequency-domain measurement. 29

Figure 1.6: (a) Measurement and (b) histogram of start-stop times in time-resolved fluorescence measurement with TCSPC (Wahl, 2014). 33

Figure 1.7: Principle of simultaneous FLIM/PLIM with TCSPC. FLIM is recorded in the "Laser ON" phases, PLIM in the "Laser OFF" phases (Chelushkin & Tunik, 2019). 34

Figure 1.8: (a) PLIM of beads infused with different Ir-compounds and fluorescent plastic acquired with TimepixCam. (b) Phosphorescence decays for areas A1-A4 indicated in (a), with monoexponential fits and residuals of the fits. (Hirvonen et al., 2017) 39

Figure 1.9: Schematic layout of the intensified Tpx3Cam camera (Sen, Hirvonen, et al., 2020). 40

Figure 2.1: Components used to build the new wide-field Tpx3Cam imager. (a) Tpx3Cam coupled to Cricket, filter and lens; (b) Cricket adapter; (c) Lens; (d) C-mount and ring connectors, (d) LED; Imager setup covered in black box; Electronic connections of pulse generators, oscilloscope and power supply; (d) PC for collection of raw data. 54

Figure 2.2: Pulsing scheme of the imager. The LED is pulsed every 100 μs with 50 ns duration of the pulse. Tpx3Cam is provided with a synchronous pulse 10 μs before the LED, which is time-stamped and included into the data stream. The camera records the photon hits for 100 μs until the next LED pulse (Sen, Hirvonen, et al., 2020). 55

Figure 3.1: Experimental setup of the PLIM macro-imager based on Tpx3Cam (Sen, Hirvonen, et al., 2020).....60

Figure 3.2: Samples used to characterize the imager: (a) USAF resolution test target; (b) Planar PtBP-RL100 based O_2 sensor film and (c) its absorption spectrum; (d) PtBP-RL100 sensor spots on PVDF membrane, (e) Sensor film with PtBP and aza-Bodipy dyes in RL100, and (f) its absorption spectrum. Spectra were measured on an 8453UV-Visible spectrophotometer (Agilent). Adapted from (Sen, Hirvonen, et al., 2020). 61

Figure 3.3: Single photon events detected with the Tpx3Cam setup. (a) TOT, i.e., intensity, (b) arrival time, (c-e) Re-scaled arrival time for individual photon events showing the "timewalk" effect (Sen, Hirvonen, et al., 2020). 62

Figure 3.4: Images of 1951 USAF resolution test target overlaid on top of a phosphorescent O_2 sensor foil. (a) Sum image showing the PLIM imager field of view. (b-e) images of the area indicated in (a) centroided with different methods: (b) sum, (c) brightest pixel (BP), (d) earliest timecode, (e) center-of-mass with 1/5-pixel accuracy (CoM 5). (f) Cross-sections of the bars in the area indicated in (e), where the sub-pixel centroiding can still resolve lines with ~40 μm spacing, that cannot be resolved with the other centroiding methods (Sen, Hirvonen, et al., 2020).....63

Figure 3.5: Instrument Response Function (IRF) position in the measurement time interval is shown for all hit pixels and for the centroided pixels. In both cases the distributions are shown before and after the TOT correction. Gaussian fit of the centroided and TOT corrected distribution corresponds to the IRF FWHM of 30.6 ns. Background was described with a constant in the fit (Sen, Hirvonen, et al., 2020). 64

Figure 3.6: Two-dimensional distributions of time, in microseconds, versus TOT, in nanoseconds, for four cases: (a) all hit pixels; (b) all hit pixels with TOT correction applied; (c) centroided pixels; (d) centroided pixels with TOT correction applied (Sen, Hirvonen, et al., 2020). 65

Figure 4.1: Exemplary photographs of arrays of the phosphorescent coatings with 250 ng of PtBP dye in the different polymers (a) and with decreasing PtBP concentration in one polymer (seven serial 1:3 dilutions) (b), spotted on planar solid support. Spot size is 2-3 mm across (Sen, Zhdanov, Hirvonen, et al., 2020b). 69

Figure 4.2: Images of the different phosphorescent coatings spotted on polyester film. (a) Grey scale intensity images; (b) PLIM images at room temperature; (c) PLIM images of the sensors obtained at 40 °C; (d) PLIM images of the sensors obtained under zero O_2 condition at room temperature (Sen, Zhdanov, Hirvonen, et al., 2020b). Images were acquired for 20 seconds with LED at 4V with pulse width of 50 ns. 69

Figure 4.3: Graphs representing (a) line profile across the sensor spots for the PLIM images shown in Figure 4.2b; (b) line profile across the sensor spots for the intensity

images shown in Figure 4.2a; (c) Phosphorescence decays with bi-exponential fits for the different ROIs marked in Figure 4.2b (Sen, Zhdanov, Hirvonen, et al., 2020b). 70

Figure 4.4: Images of the polymeric phosphorescent coatings on polyester support taken on the Tpx3Cam imager at 20^{o}C (a) and at 40^{o}C (b) and presented in lifetime (left) and Intensity (right) scale; (c) Normalised phosphorescence decays for the Hydrogel sensor at different temperatures (Sen, Zhdanov, Hirvonen, et al., 2020b).71

Figure 4.5: Sets of commercial and custom-made O_2 sensors imaged with the Tpx3Cam imager. (a) Photograph and (b) PLIM image of the PtBP based sensors in various forms; (c) Photograph and (d) PLIM image of LDPE-PLA based PtBP sensors and (e) Photograph and (f) PLIM image of the two PtOPEK based sensors (Sen, Zhdanov, Hirvonen, et al., 2020a). 73

Figure 4.6: The PLT data for Sensors 1–3* generated on the Tpx3cam imager under oxygenated and deoxygenated conditions. (a) shows the intensity and PLIM images of sensor 1–3 in their oxygenated and deoxygenated state. (b) shows the decay fittings for sensor 1 in its oxygenated and deoxygenated state. c, d and e represent the cumulative distribution histograms for sensors 1–3 in oxygenated (21% O_2) and deoxygenated (~0% O_2) conditions (Sen et al., 2022). *Sensor 1: PtOEP, Sensor 2: PtOEP + OEPK, Sensor 3: PtOEP-SB 75

Figure 4.7: Intensity (top) and lifetime (bottom) Images for the different phosphorescent coatings on polyester support, measured on the confocal PLIM microscope at room temperature (Sen, Zhdanov, Hirvonen, et al., 2020b). 77

Figure 4.8: Lifetime response to O_2 partial pressure for the polystyrene, PVDC and Optech (Mocon) sensors/coatings at 25 °C (Sen, Zhdanov, Hirvonen, et al., 2020b). 79

Figure 4.9: PLIM (top row) and intensity (bottom row) images of the sensor palettes prepared using the cocktails with 1:3 serial dilutions of PtBP dye in: (a) Polystyrene, (b) PVC, (c) PVDC, (d) PMMA and (e) Hydrogel D4 (Sen, Zhdanov, Hirvonen, et al., 2020b). 80

Figure 4.10: Variation of the intensity and lifetime for Polystyrene based PtBP dye with increasing dilutions (Sen, Zhdanov, Hirvonen, et al., 2020a).....81

Figure 5.1: PLIM of dissolved O_2 distribution in media containing cultured cells. (a) Effects of NanO2-IR on viability of HCT116 and HEK293a cells. Total ATP levels were measured with CellTiter-Glo ATP assay after incubating the cells with the probe (1 mg/mL) for indicated time; all values are normalised to ATP levels in untreated cells. N = 3, mean ± SD are shown. (b, c) PLIM images of the probe (1 mg/mL) evenly distributed in growth medium containing no cells (b), and 1×10^6 or 5×10^6 of respiring HCT116 cells precipitated at the bottom; (c) photographs of 0.5 mL qPCR tubes with cell pellets. False colour images show increased lifetime values (μs), or decreased O_2 in and near the cells. (d) line profile analysis (along the dotted

lines in (b) and (c)) quantifies this effect (Sen, Zhdanov, Bastiaanssen, et al., 2020). 84

Figure 5.2: O_2 calibration of NanO2-IR probe under physiological conditions. Lifetime values were measured with a handheld reader Optech (Mocon, USA) in liquid samples (DMEM media) equilibrated with 0%, 2.0%, 5.0%, 10.0%, 12.0%, 15.0%, 17.0%, 20.0% and 21.0% O_2 gas standards produced on a gas mixer, at 37 °C. Exponential fitting was performed using https ://mycur vefit .com/ (Sen, Zhdanov, Bastiaanssen, et al., 2020). 85

Figure 5.3: PLIM of O_2 in the surface-stained mouse brain and lung tissue samples. (a) Photograph and phosphorescence intensity image of cortex tissue samples stained with NanO2-IR (1 mg/mL in DMEM, 30 min). (b) Corresponding PLIM images of the untreated control (C1-C3) and AntA/NaN3-treated samples (T1, T2). (c) Photograph and phosphorescence intensity image and (d) PLIM images of untreated control (C1–C3) and AntA/NaN_3-treated lung tissue samples (T1, T2). (e, f) Lifetime frequency histograms for the brain and lung tissue with normal and inhibited mitochondrial respiration. Violin plots show: on the Y-axis—the distribution of lifetime values; on the X-axis—sample names and relative frequencies, with which lifetime values were recorded. Box-plot partition of the violin plots represent the median (circle) and interquartile ranges. Dashed horizontal lines represent the aggregated modes per tissue type and treatment. On the right side, semi-transparent colour-matched aggregated lifetime distributions are shown. Colours correspond to the predominant spectrum in the PLIM images. (g, h) Line profile analysis of the variability and interdependence of the intensity and lifetime values across the brain tissue samples (exemplified by a red dotted line in (a)); three-line profiles in three brain samples were analysed in total. In (h), all measured values are shown as single data points normalised to the mean; average deviations (in a.u.) were: for intensity signals—0.287, 0.076 and 0.159; for lifetime values-0.097, 0.057 and 0.124. (i) Tissue photograph, phosphorescence intensity of the probe and PLIM images of cortex slices are shown. Scale bars show object dimensions. Rainbow false colours in (b, d, i) are used to visualise the range of lifetime values (Sen, Zhdanov, Bastiaanssen, et al., 2020). 88

Figure 5.4: (a) Imaging of oxygenation in ex-vivo samples of mouse tissue: effects of tissue type, treatment and O_2 availability. O_2 levels in the normally respiring brain tissue surface-stained with NanO2-IR, and in the tissue with inhibited mitochondrial respiration (AntA/NaN_3). O_2 levels are calculated from lifetime values shown it Figure 5.3e. Violin plots show: on the Y-axis – the distribution of O_2 values; on the X-axis – relative frequencies of given O_2 values. Colours correspond to the predominant spectrum in the PLIM images. Box-plot partition of the violin plots represents the median and interquartile ranges. Dashed horizontal lines represent the aggregated modes for the different tissue type, treatment or staining method. On the right side, semi-transparent colour-matched aggregated distributions are shown. (b) Dependence of the calculated lifetime values on measured phosphorescence intensity signals. Pearson correlation analysis of the PLIM and intensity images of a surface-stained brain sample (Sen, Zhdanov, Bastiaanssen, et al., 2020).....90

Figure 5.5: PLIM of O_2 in the intraluminally stained mouse intestine samples. Photographs and phosphorescence intensity images of the small (a) and large (d) intestine stained for 15 min with NanO2-IR by intraluminal injection (1 mg/ml, 1 μl) as shown in (b); a separate set of samples was surface-stained in parallel. Typical PLIM images of the small (c) and large (e) intestine in the respiring state (left) and upon mitochondrial inhibition for 15 min by 10 μM AntA and 0.1% NaN3 (right). In (e), selected localised O_2 concentrations (in μM) are shown in italic (see also Figs. S1 and S3). (f) PLIM images of the colon sample (e), collected 2 h and 4 h after the NanO2-IR injection. Lifetime frequency histograms in samples of the small (g) and large intestine (h) with normal and inhibited mitochondrial respiration. (i) Comparative analysis of lifetime frequencies in the colon samples stained with NanO2-IR intraluminally and topically on the serosal side. (j) Lifetime frequency histograms corresponding to the colon sample are shown in (e, f): lifetime images are taken 15 min, 2 h and 4 h post injection. PLIM images are prepared using rainbow false colours. In (g–j), violin plots show the distribution of lifetime values along the Y-axis against relative frequencies, with which these values were recorded in individual samples (X-axis). Box-plot partition of the violin plots demonstrates the median (circle) and interquartile ranges. Dashed horizontal lines show the aggregated modes per tissue type / staining protocol / treatment. On the right side, semi-transparent colour-matched aggregated lifetime distributions are shown. Colours correspond to the predominant spectrum in the PLIM images (Sen, Zhdanov, Bastiaanssen, et al., 2020). 92

Figure 5.6: Imaging of oxygenation in ex-vivo samples of mouse tissue: effects of tissue type, treatment and O_2 availability. O_2 levels on the outer, serosal side of the colon (surface-stained) and inside the lumen or on the inner, mucosal surface. O_2 levels are calculated from lifetime values shown it Figure 5.5i. Violin plots show: on the Y-axis - the distribution of O_2 values; on the X-axis - relative frequencies of given O_2 values. Colours correspond to the predominant spectrum in the PLIM images. Box-plot partition of the violin plots represents the median and interquartile ranges. Dashed horizontal lines represent the aggregated modes for the different tissue type, treatment or staining method. On the right side, semi-transparent colour-matched aggregated distributions are shown (Sen, Zhdanov, Bastiaanssen, et al., 2020). 94

Figure 5.7: PLIM of O_2 in the subcutaneously stained tail (a) and paw (b) of a mouse (post mortem). On the left, photographs and PLIM images are shown. Rainbow false colours demonstrate the range of lifetime values. (c) Lifetime frequency distribution calculated from (a) and (b); violin plots show the distribution of lifetime values along the Y-axis, and relative frequencies, with which these values were obtained (X-axis). Box-plot partition of the violin plots demonstrates the median (circle) and interquartile ranges. Dashed horizontal lines show the aggregated modes for each tissue type. On the right side, semi-transparent colour-matched aggregated lifetime distributions are shown (Sen, Zhdanov, Bastiaanssen, et al., 2020). 95

Figure 5.8: Optimisation of NanO2-IR delivery to grafted tumours in mice. (a) Effects of the different concentrations of NanO2-IR probe (indicated, incubation

time 18 h) on the viability of cultured CT26 cells. Analysed with a CellTiter-Glo® kit which measures total cellular ATP levels. (b, c) Confocal microscopy analysis of staining efficiency of CT26 cell at different concentrations of NanO2-IR (18 h). (d) Distribution histogram of lifetime values, calculated for the cells stained with different concentrations of NanO2-IR (as in b, c). (e) PLIM images of tumour tissue produced by different means of NanO2-IR delivery. (f) Bar charts comparing probe lifetime values for the different trials. 99

Figure 5.9: Imaging analysis of tumour oxygenation. (a) The scheme of in vivo and post-mortem O_2 imaging of tumour tissue of mice. CT26 cells stained with NanO2-IR (50 mg/ml, 18 h) were mixed with non-stained CT26 cells (1:1) and injected in mice subcutaneously (right flanks); tumours were allowed to grow for up to 17 days, and then were analysed on the Tpx3Cam PLIM imager on days 3, 7, 10 and 17 in vivo and immediately after animal death. After this NanO2-IR distribution was analysed in fixed tumour tissues on the confocal PLIM microscope. Animals in control group (tumour size and phosphorescence background controls) were injected with non-stained CT26 cells. N=6 in all animal groups. (b) Comparison of the growth rate of the control and stained tumours. (c) Intensity and PLIM images of the live and euthanised animals on different days of tumour growth. (d) The LT values in tumour regions of live and euthanised animals, taken with 6 min intervals on the different days of tumour growth (N=3 in each group). 100

Figure 5.10: Analysis of NanO2-IR localisation in tumour tissue. (a) Representative image of tumour tissue with NanO2-IR ‘isle’ positioned in the middle (left). The corresponding phosphorescence intensity image obtained by confocal PLIM microscopy (right, 5x magnification). (b, c) Typical span of the phosphorescence intensity signals across the NanO2-IR ‘isle’ (B) and the corresponding lifetime values (c). (d) Analysis of the intensity signal of NanO2-IR residing in tumour tissue at different stages of tumour development. (e) Response of NanO2-IR ‘isle’ to chemical deoxygenation of the tissue by sulphite. Right panel shows the typical shift of the distribution of lifetime values in response to decreased O_2 levels. Images represent stacks of six (a-c) or three (e) focal planes taken in 5 µm step. 102

Figure S.0.1: Mapping O_2 in the lumen of mouse colon ex vivo. (a) From bottom to top, the lifetime (LT) image, O_2 image and detailed O_2 map of the lumen of mouse colon stained as described for Figure 5.5e. (b) Similar to (a) data set obtained using mouse colon treated for 15 min with AntA and NaN_3. Right panel in (b) also shows the LT map and magnified fragments of LT and O_2 maps that show the conversion of LT values (µs) into O_2 concentrations (µM) using the indicated analytical equation. 109

Figure S.0.2: Effects of NanO2-IR on CT26 cell proliferation capacity. A. Cells were stained for ~20 h with the probe at the indicated concentrations (top panel), washed, re-plated and grown for further 28 h (bottom panel). B. Cells stained as in (A) with 200 µg/ml probe were mixed with non-stained cells (1:1), re-plated and grown for 28 h (right panel); non-stained cells (left) and stained cells (middle) only are shown as

controls for maximal and minimal proliferation, respectively. Bars indicate ~100 µm scale. Images were taken using a light microscope and iPhone camera. 110

Figure S.0.3: Analysis of NanO2-IR phosphorescence intensity in tumour tissue at different stages of tumour development. Images in (**A**) were collected using confocal PLIM microscope with 5x magnification. **B**. Quantitative analysis of NanO2-IR signals in tumour tissue (N=16, including days 10, 14 and 17); tissue with no NanO2-IR was used as background control. 111

Thesis Outcomes

Peer reviewed papers:

Rajannya Sen, Liisa M. Hirvonen, Alexander Zhdanov, Peter Svihra, Stefan Andersson-Engels, Andrei Nomerotski, and Dmitri Papkovsky. "New luminescence lifetime macro-imager based on a Tpx3Cam optical camera." *Biomedical Optics Express* 11, no. 1 (2020): 77-88.

Rajannya Sen, Alexander V. Zhdanov, Liisa M. Hirvonen, Peter Svihra, Stefan Andersson-Engels, Andrei Nomerotski, and Dmitri B. Papkovsky. "Characterization of planar phosphorescence based oxygen sensors on a TCSPC-PLIM macro-imager." *Sensors and Actuators B: Chemical* 321 (2020): 128459.

Rajannya Sen, Alexander V. Zhdanov, Thomaz FS Bastiaanssen, Liisa M. Hirvonen, Peter Svihra, Patrick Fitzgerald, John F. Cryan, Stefan Andersson-Engels, Andrei Nomerotski, and Dmitri B. Papkovsky. "Mapping O_2 concentration in ex-vivo tissue samples on a fast PLIM macro-imager." *Scientific Reports* 10, no. 1 (2020): 1-11.

Rajannya Sen, Liang Li, Alexander V. Zhdanov, Rafael DL Gaspar, and Dmitri B. Papkovsky. "Phosphorescence lifetime measurements with sensor materials: Comparison of the four different detection platforms." *Sensors and Actuators B: Chemical* 371 (2022): 132496.

Alexander V. Zhdanov, Rajannya Sen, Ciaran Devoy, Liang Li, Mark Tangney, and Dmitri B. Papkovsky. “Analysis of tumour oxygenation in model animals on a phosphorescence lifetime based macro-imager.” (Submitted)

Conference proceedings:

Rajannya Sen, Alexander Zhdanov, Liisa M. Hirvonen, Peter Svihra, Stefan Andersson-Engels, Andrei Nomerotski, and Dmitri Papkovsky. "A new macro-imager based on Tpx3Cam optical camera for PLIM applications." In Biomedical Spectroscopy, Microscopy, and Imaging, vol. 11359, pp. 243-250. SPIE, 2020.

Bibliography

Abdelrahman, M. A., Marston, G., Hull, M. A., Markham, A. F., Jones, P. F., Evans, J. A. & Coletta, P. L. (2012). High-frequency ultrasound for in vivo measurement of colon wall thickness in mice. *Ultrasound in Medicine & Biology*, *38*(3), 432–442.

Agronskaia, A. V., Tertoolen, L. & Gerritsen, H. C. (2004). Fast fluorescence lifetime imaging of calcium in living cells. *Journal of Biomedical Optics*, *9*(6), 1230. https://doi.org/10.1117/1.1806472

Al Darwish, R., Marcu, L. & Bezak, E. (2019). Overview of current applications of the Timepix detector in spectroscopy, radiation and medical physics. *Applied Spectroscopy Reviews*, 1–19.

Allum, F., Cheng, C., Howard, A. J., Bucksbaum, P. H., Brouard, M., Weinacht, T. & Forbes, R. (2021). Multi-particle three-dimensional covariance imaging:“coincidence” insights into the many-body fragmentation of strong-field ionized D2O. *The Journal of Physical Chemistry Letters*, *12*(34), 8302–8308.

Amao, Y., Ishikawa, Y. & Okura, I. (2001). Green luminescent iridium (III) complex immobilized in fluoropolymer film as optical oxygen-sensing material. *Analytica Chimica Acta*, *445*(2), 177–182.

Amao, Y. & Okura, I. (2003). Optical oxygen sensing materials: chemisorption film of ruthenium (II) polypyridyl complexes attached to anionic polymer. *Sensors and Actuators B: Chemical*, *88*(2), 162–167.

Amao, Y. & Okura, I. (2009). Optical oxygen sensor devices using metalloporphyrins. *Journal of Porphyrins and Phthalocyanines*, *13*(11), 1111–1122.

Ann, C. & Kelly, C. A. (2017). *University of Ireland , Cork in Fulfilment of*.

Apreleva, S. V, Wilson, D. F. & Vinogradov, S. A. (2006). Tomographic imaging of oxygen by phosphorescence lifetime. *Applied Optics*, *45*(33), 8547–8559.

Babilas, P., Lamby, P., Prantl, L., Schreml, S., Jung, E. M., Liebsch, G., Wolfbeis, O. S., Landthaler, M., Szeimies, R. & Abels, C. (2008). Transcutaneous pO2 imaging during tourniquet-induced forearm ischemia using planar optical oxygen sensors. *Skin Research and Technology*, *14*(3), 304–311.

Babilas, P., Liebsch, G., Schacht, V., Klimant, I., Wolfbeis, O. S., Szeimies, R.-M. & Abels, C. (2005). In Vivo Phosphorescence Imaging of pO2 Using Planar Oxygen Sensors. *Microcirculation*, *12*(6), 477–487.

Banerjee, S., Arzhakova, O. V., Dolgova, A. A. & Papkovsky, D. B. (2016). Phosphorescent oxygen sensors produced from polyolefin fibres by solvent-crazing method. *Sensors and Actuators, B: Chemical*, *230*(March), 434–441. https://doi.org/10.1016/j.snb.2016.02.062

Banerjee, S., Kelly, C. A., Kerry, J. P. & Papkovsky, D. B. (2016). High throughput non-destructive assessment of quality and safety of packaged food products using phosphorescent oxygen sensors. *Trends in Food Science and Technology*, *50*, 85–102. https://doi.org/10.1016/j.tifs.2016.01.021

Banerjee, S., Kuznetsova, R. T. & Papkovsky, D. B. (2015). Solid-state oxygen sensors based on phosphorescent diiodo-borondipyrromethene dye. *Sensors and Actuators, B: Chemical*, *212*, 229–234. https://doi.org/10.1016/j.snb.2015.02.016

Bartlett, K., Saka, M. & Jones, M. (2008). Polarographic Electrode Measures of Cerebral Tissue Oxygenation: Implications for Functional Brain Imaging. *Sensors (Basel, Switzerland)*, *8*(12), 7649–7670. https://doi.org/10.3390/s8127649

Baudelet, C. & Gallez, B. (2002). How does blood oxygen level-dependent (BOLD) contrast correlate with oxygen partial pressure (pO2) inside tumors? *Magnetic Resonance in Medicine*, *48*(6), 980–986. https://doi.org/10.1002/mrm.10318

Beacham, R., Mac Raighne, A., Maneuski, D., O'Shea, V., McVitie, S. & McGrouther, D. (2011). Medipix2/Timepix detector for time resolved Transmission Electron Microscopy. *Journal of Instrumentation*, *6*(12). https://doi.org/10.1088/1748-0221/6/12/C12052

Becker, W. (2005). *Advanced time-correlated single photon counting techniques* (Vol. 81). Springer Science & Business Media.

Becker, W. (2012). Fluorescence lifetime imaging - techniques and applications. *Journal of Microscopy*, *247*(2), 119–136. https://doi.org/10.1111/j.1365-2818.2012.03618.x

Becker, W. (2015). *Advanced time-correlated single photon counting applications* (Vol. 111). Springer.

Becker, W. (2018). Advanced TCSPC-FLIM techniques. In *Multiphoton Microscopy and Fluorescence Lifetime Imaging: Applications in Biology and Medicine* (pp. 23–52). Walter de Gruyter GmbH. https://doi.org/10.1515/9783110429985-005

Becker, W., Shcheslavskiy, V. & Rück, A. (2017). Simultaneous phosphorescence and fluorescence lifetime imaging by multi-dimensional TCSPC and multi-pulse excitation. In *Multi-Parametric Live Cell Microscopy of 3D Tissue Models* (pp. 19–30). Springer.

Beerthuizen, G. I., Goris, R. J. & Kreuzer, F. J. (1989). Skeletal muscle Po2 during imminent shock. *Archives of Emergency Medicine*, *6*(3), 172.

Bello, D. S. S., Nauta, B. & Visschers, J. (2001). Design of analog-to-digital converters for energy-sensitive hybrid pixel detectors. *Nuclear Instruments and Methods in Physics Research Section A: Accelerators, Spectrometers, Detectors and Associated Equipment*, *466*(1), 218–225.

Berezin, M. Y. & Achilefu, S. (2010). Fluorescence lifetime measurements and biological imaging. *Chemical Reviews*, *110*(5), 2641–2684. https://doi.org/10.1021/cr900343z

Boekstegers, P., Riessen, R. & Seyde, W. (1990). Oxygen partial pressure distribution within skeletal muscle: indicator of whole body oxygen delivery in patients? In *Oxygen Transport to Tissue XII* (pp. 507–514). Springer.

Borisov, S. M. (2018). CHAPTER 1 Fundamentals of Quenched Phosphorescence O_2 Sensing and Rational Design of Sensor Materials. In *Quenched-phosphorescence Detection of Molecular Oxygen: Applications in Life Sciences* (pp. 1–18). The Royal Society of Chemistry.

https://doi.org/10.1039/9781788013451-00001

Borisov, S. M. & Klimant, I. (2009). Luminescent nanobeads for optical sensing and imaging of dissolved oxygen. *Microchimica Acta*, *164*, 7–15.

Borisov, S. M., Mayr, T., Mistlberger, G., Waich, K., Koren, K., Chojnacki, P. & Klimant, I. (2009). Precipitation as a simple and versatile method for preparation of optical nanochemosensors. *Talanta*, *79*(5), 1322–1330.

Borisov, S. M., Nuss, G., Haas, W., Saf, R., Schmuck, M. & Klimant, I. (2009). New NIR-emitting complexes of platinum (II) and palladium (II) with fluorinated benzoporphyrins. *Journal of Photochemistry and Photobiology A: Chemistry*, *201*(2–3), 128–135.

Borisov, S. M., Nuss, G. & Klimant, I. (2008). Red light-excitable oxygen sensing materials based on platinum (II) and palladium (II) benzoporphyrins. *Analytical Chemistry*, *80*(24), 9435–9442.

Borisov, S. M., Papkovsky, D. B., Ponomarev, G. V, DeToma, A. S., Saf, R. & Klimant, I. (2009). Photophysical properties of the new phosphorescent platinum (II) and palladium (II) complexes of benzoporphyrins and chlorins. *Journal of Photochemistry and Photobiology A: Chemistry*, *206*(1), 87–92.

Brand, M. D. & Nicholls, D. G. (2011). Assessing mitochondrial dysfunction in cells. *Biochemical Journal*, *435*(2), 297–312. https://doi.org/10.1042/BJ20110162

Brandrup, J., Immergut, E. H. & Grulke, E. A. (2003). *Polymer Handbook, 2 Volumes Set, 4th Edition*. JOHN WILEY & SONS INC. http://www.ebook.de/de/product/3607711/j_brandrup_edmund_h_immergut_eric_a_grulke_polymer_handbook_2_volumes_set.html

Brizel, D. M., Scully, S. P., Harrelson, J. M., Layfield, L. J., Bean, J. M., Prosnitz, L. R. & Dewhirst, M. W. (1996). Tumor oxygenation predicts for the likelihood of distant metastases in human soft tissue sarcoma. *Cancer Research*, *56*(5), 941–943.

Brooks, A. J., Eastwood, J., Beckingham, I. J. & Girling, K. J. (2004). Liver tissue partial pressure of oxygen and carbon dioxide during partial hepatectomy.

British Journal of Anaesthesia, *92*(5), 735–737.

Bruza, P., Petusseau, A., Ulku, A., Gunn, J., Streeter, S., Samkoe, K., Bruschini, C., Charbon, E. & Pogue, B. (2021). Single-photon avalanche diode imaging sensor for subsurface fluorescence LiDAR. *Optica*, *8*(8), 1126. https://doi.org/10.1364/optica.431521

Buschmann, V., Orthaus, S., Devaux, A. & Erdmann, R. (2016). Phosphorescence Lifetime Imaging Microscopy (PLIM) Measurements : Practical Aspects. *PicoQuant Technical Note*, *Ic*, 1–10.

Busse, L. J., Pratt, R. G. & Thomas, S. R. (1988). Deconvolution of chemical shift spectra in two- or three-dimensional [19F] MR imaging. *Journal of Computer Assisted Tomography*, *12*(5), 824–835. https://doi.org/10.1097/00004728-198809010-00020

Carraway, E. R., Demas, J. N., DeGraff, B. A. & Bacon, J. R. (1991). Photophysics and Photochemistry of Oxygen Sensors Based on Luminescent Transition-Metal Complexes. *Analytical Chemistry*, *63*(4), 337–342. https://doi.org/10.1021/ac00004a007

Carreau, A., Hafny-Rahbi, B. El, Matejuk, A., Grillon, C. & Kieda, C. (2011). Why is the partial oxygen pressure of human tissues a crucial parameter? Small molecules and hypoxia. *Journal of Cellular and Molecular Medicine*, *15*(6), 1239–1253.

Chelushkin, P. S. & Tunik, S. P. (2019). Phosphorescence lifetime imaging (PLIM): State of the art and perspectives. In *Springer Series in Chemical Physics* (Vol. 119, Issue January). Springer International Publishing. https://doi.org/10.1007/978-3-030-05974-3_6

Chen, W., Hill, H., Christie, A., Kim, M. S., Holloman, E., Pavia-Jimenez, A., Homayoun, F., Ma, Y., Patel, N. & Yell, P. (2016). Targeting renal cell carcinoma with a HIF-2 antagonist. *Nature*, *539*(7627), 112–117.

Chen, X., Zhong, Z., Li, Z., Jiang, Y., Wang, X. & Wong, K. (2002). Characterization of ormosil film for dissolved oxygen-sensing. *Sensors and Actuators B: Chemical*, *87*(2), 233–238.

Cheung, A., Tu, L., Macnab, A., Kwon, B. K. & Shadgan, B. (2022). Detection of hypoxia by near-infrared spectroscopy and pulse oximetry: a comparative study. *Journal of Biomedical Optics*, *27*(07), 1–10. https://doi.org/10.1117/1.jbo.27.7.077001

Chmeissani, M. & Mikulec, B. (2001). Performance limits of a single photon counting pixel system. *Nuclear Instruments and Methods in Physics Research Section A: Accelerators, Spectrometers, Detectors and Associated Equipment*, *460*(1), 81–90.

Cho, H., Du, X., Rizzi, J. P., Liberzon, E., Chakraborty, A. A., Gao, W., Carvo, I., Signoretti, S., Bruick, R. K. & Josey, J. A. (2016). On-target efficacy of a HIF-2α antagonist in preclinical kidney cancer models. *Nature*, *539*(7627), 107–111.

Chu, C.-S. & Lo, Y.-L. (2011). Highly sensitive and linear calibration optical fiber oxygen sensor based on Pt (II) complex embedded in sol–gel matrix. *Sensors and Actuators B: Chemical*, *155*(1), 53–57.

Clark Jr., L. C., Kaplan, S., Matthews, E. C., Edwards, P. K. & Helmsworth, J. A. (1958). Monitor and control of blood oxygen tension and pH during total body perfusion. *Journal of Thoracic Surgery*, *36*(4), 488–496.

Collingridge, D. R., Young, W. K., Vojnovic, B., Wardman, P., Lynch, E. M., Hill, S. A. & Chaplin, D. J. (1997). Measurement of tumor oxygenation: A comparison between polarographic needle electrodes and a time-resolved luminescence-based optical sensor. *Radiation Research*, *147*(3), 329–334. https://doi.org/10.2307/3579340

D'Amen, G., Keach, M., Nomerotski, A., Svihra, P. & Tricoli, A. (2021). Novel imaging technique for α-particles using a fast optical camera. *Journal of Instrumentation*, *16*(02), P02006.

Debrah, D. A., Stewart, G. A., Basnayake, G., Nomerotski, A., Svihra, P., Lee, S. K. & Li, W. (2020). Developing a camera-based 3D momentum imaging system capable of 1 Mhits/s. *Review of Scientific Instruments*, *91*(2), 23316.

Degraff, B. A. & Demas, J. N. (2007). *Luminescence-Based Oxygen Sensors*. *December*. https://doi.org/10.1007/0-387-23690-2

Devor, A., Sakadžić, S., Srinivasan, V. J., Yaseen, M. A., Nizar, K., Saisan, P. A., Tian, P., Dale, A. M., Vinogradov, S. A. & Franceschini, M. A. (2012). Frontiers in optical imaging of cerebral blood flow and metabolism. *Journal of Cerebral Blood Flow & Metabolism*, *32*(7), 1259–1276.

Di Marco, G., Lanza, M., Pieruccini, M. & Campagna, S. (1996). A luminescent iridium (III) cyclometallated complex immobilized in a polymeric matrix as a solid-state oxygen sensor. *Advanced Materials*, *8*(7), 576–580.

Diaspro, A., Chirico, G., Federici, F., Cannone, F., Beretta, S. & Robello, M. (2001). Two-photon microscopy and spectroscopy based on a compact confocal scanning head. *Journal of Biomedical Optics*, *6*(3), 300–310.

Dings, J., Meixensberger, J., Jäger, A. & Roosen, K. (1998). Clinical experience with 118 brain tissue oxygen partial pressure catheter probes. *Neurosurgery*, *43*(5), 1082–1094.

Dmitriev, R. I., Kondrashina, A. V, Koren, K., Klimant, I., Zhdanov, A. V, Pakan, J. M. P., McDermott, K. W. & Papkovsky, D. B. (2014). Small molecule phosphorescent probes for O 2 imaging in 3D tissue models. *Biomaterials Science*, *2*(6), 853–866.

Dmitriev, R. I. & Papkovsky, D. B. (2012). Optical probes and techniques for O_2 measurement in live cells and tissue. *Cellular and Molecular Life Sciences*, *69*(12), 2025–2039.

Dmitriev, R. I. & Papkovsky, D. B. (2018). *Quenched-phosphorescence Detection of Molecular Oxygen: Applications in Life Sciences*. Royal Society of Chemistry. https://books.google.ie/books?id=mMBZswEACAAJ

Dmitriev, R. I., Ropiak, H. M., Yashunsky, D. V, Ponomarev, G. V, Zhdanov, A. V & Papkovsky, D. B. (2010). Bactenecin 7 peptide fragment as a tool for intracellular delivery of a phosphorescent oxygen sensor. *The FEBS Journal*, *277*(22), 4651–4661.

Dmitriev, R. I., Zhdanov, A. V, Nolan, Y. M. & Papkovsky, D. B. (2013). Imaging of neurosphere oxygenation with phosphorescent probes. *Biomaterials*, *34*(37), 9307–9317. https://doi.org/10.1016/j.biomaterials.2013.08.065

Dunphy, I., Vinogradov, S. A. & Wilson, D. F. (2002). Oxyphor R2 and G2: phosphors for measuring oxygen by oxygen-dependent quenching of phosphorescence. *Analytical Biochemistry*, *310*(2), 191–198. https://doi.org/https://doi.org/10.1016/S0003-2697(02)00384-6

Dysli, C., Wolf, S., Berezin, M. Y., Sauer, L., Hammer, M. & Zinkernagel, M. S. (2017). Fluorescence lifetime imaging ophthalmoscopy. *Progress in Retinal and Eye Research*, *60*, 120–143. https://doi.org/10.1016/j.preteyeres.2017.06.005

Eastwood, D. & Gouterman, M. (1970). Porphyrins: Xviii. luminescence of (co),(ni), pd, pt complexes. *Journal of Molecular Spectroscopy*, *35*(3), 359–375.

Erzina, D. R., Zamilatskov, I. A., Stanetskaya, N. M., Tyurin, V. S., Kozhemyakin, G. L., Ponomarev, G. V, Chernyshev, V. V & Fitch, A. N. (2019). Transformations of meso-Iminofunctionalized Pd (II) and Ni (II)-Complexes of β-Alkylsubstituted Porphyrins. *European Journal of Organic Chemistry*, *2019*(7), 1508–1522.

Esipova, T. V, Barrett, M. J. P., Erlebach, E., Masunov, A. E., Weber, B. & Vinogradov, S. A. (2019). Oxyphor 2P: A High-Performance Probe for Deep-Tissue Longitudinal Oxygen Imaging. *Cell Metabolism*, *29*(3), 736-744.e7. https://doi.org/https://doi.org/10.1016/j.cmet.2018.12.022

Feng, Y., Cheng, J., Zhou, L., Zhou, X. & Xiang, H. (2012). Ratiometric optical oxygen sensing: a review in respect of material design. *Analyst*, *137*(21), 4885–4901.

Fercher, A., Borisov, S. M., Zhdanov, A. V, Klimant, I. & Papkovsky, D. B. (2011). Intracellular O_2 sensing probe based on cell-penetrating phosphorescent nanoparticles. *ACS Nano*, *5*(7), 5499–5508. https://doi.org/10.1021/nn200807g

Fercher, A., Ponomarev, G. V, Yashunski, D. & Papkovsky, D. B. (2010). Evaluation of the derivates of phosphorescent Pt-coproporphyrin as intracellular oxygen-sensitive probes. *Analytical and Bioanalytical Chemistry*, *396*, 1793–1803.

Finikova, O. S., Lebedev, A. Y., Aprelev, A., Troxler, T., Gao, F., Garnacho, C.,

Muro, S., Hochstrasser, R. M. & Vinogradov, S. A. (2008). Oxygen microscopy by two-photon-excited phosphorescence. *ChemPhysChem*, *9*(12), 1673–1679.

Fischer, F., Volkmer, B., Puschmann, S., Greinert, R., Breitbart, E., Kiefer, J. & Wepf, R. (2008). Assessing the risk of skin damage due to femtosecond laser irradiation. *Journal of Biophotonics*, *1*(6), 470–477.

Fisher-Levine, M., Boll, R., Ziaee, F., Bomme, C., Erk, B., Rompotis, D., Marchenko, T., Nomerotski, A. & Rolles, D. (2018). Time-resolved ion imaging at free-electron lasers using TimepixCam. *Journal of Synchrotron Radiation*, *25*(2), 336–345.

Fisher-Levine, M. & Nomerotski, A. (2016). TimepixCam: A fast optical imager with time-stamping. *Journal of Instrumentation*, *11*(3). https://doi.org/10.1088/1748-0221/11/03/C03016

Fleming, I. N., Manavaki, R., Blower, P. J., West, C., Williams, K. J., Harris, A. L., Domarkas, J., Lord, S., Baldry, C. & Gilbert, F. J. (2015). Imaging tumour hypoxia with positron emission tomography. *British Journal of Cancer*, *112*(2), 238–250. https://doi.org/10.1038/bjc.2014.610

Gambhir, S. S. (2002). Molecular imaging of cancer with positron emission tomography. *Nature Reviews. Cancer*, *2*(9), 683–693. https://doi.org/10.1038/nrc882

Gersbach, M., Trimananda, R., Maruyama, Y., Fishburn, M., Stoppa, D., Richardson, J., Walker, R., Henderson, R. K. & Charbon, E. (2010). High frame-rate TCSPC-FLIM using a novel SPAD-based image sensor. *Detectors and Imaging Devices: Infrared, Focal Plane, Single Photon*, *7780*(May 2014), 77801H. https://doi.org/10.1117/12.860769

Godet, I., Doctorman, S., Wu, F. & Gilkes, D. M. (2022). Detection of Hypoxia in Cancer Models: Significance, Challenges, and Advances. *Cells*, *11*(4). https://doi.org/10.3390/cells11040686

Golub, A. S. & Pittman, R. N. (2008). PO2 measurements in the microcirculation using phosphorescence quenching microscopy at high magnification. *American Journal of Physiology-Heart and Circulatory Physiology*, *294*(6), H2905–

H2916.

Göppert-Mayer, M. (1931). Über elementarakte mit zwei quantensprüngen. *Annalen Der Physik*, *401*(3), 273–294.

Gordon, Y., Partovi, S., Müller-Eschner, M., Amarteifio, E., Bäuerle, T., Weber, M.-A., Kauczor, H.-U. & Rengier, F. (2014). Dynamic contrast-enhanced magnetic resonance imaging: fundamentals and application to the evaluation of the peripheral perfusion. *Cardiovascular Diagnosis and Therapy*, *4*(2), 147–164. https://doi.org/10.3978/j.issn.2223-3652.2014.03.01

Grewer, C. & Brauer, H. D. (1993). Temperature dependence of the oxygen quenching of ππ*-singlet and ππ*-triplet states of singlet oxygen sensitizers. *Journal of Physical Chemistry*, *97*(19), 5001–5006. https://doi.org/10.1021/j100121a024

Grist, S. M., Chrostowski, L. & Cheung, K. C. (2010). Optical oxygen sensors for applications in microfluidic cell culture. *Sensors*, *10*(10), 9286–9316.

Guice, K. B., Caldorera, M. E. & McShane, M. J. (2005). Nanoscale internally referenced oxygen sensors produced from self-assembled nanofilms on fluorescent nanoparticles. *Journal of Biomedical Optics*, *10*(6), 64031.

Hamaoka, T. & McCully, K. K. (2019). Review of early development of near-infrared spectroscopy and recent advancement of studies on muscle oxygenation and oxidative metabolism. *Journal of Physiological Sciences*, *69*(6), 799–811. https://doi.org/10.1007/s12576-019-00697-2

Hartmann, P., Leiner, M. J. P. & Lippitsch, M. E. (1995). Response characteristics of luminescent oxygen sensors. *Sensors and Actuators B: Chemical*, *29*(1–3), 251–257.

Hirvonen, L. M., Festy, F. & Suhling, K. (2014). Wide-field time-correlated single-photon counting (TCSPC) lifetime microscopy with microsecond time resolution. *Optics Letters*, *39*(19), 5602. https://doi.org/10.1364/ol.39.005602

Hirvonen, L. M., Fisher-Levine, M., Suhling, K. & Nomerotski, A. (2017). Photon counting phosphorescence lifetime imaging with TimepixCam. *Review of Scientific Instruments*, *88*(1), 13104.

Hirvonen, L. M., Petrášek, Z., Beeby, A. & Suhling, K. (2015). Sub-μs time resolution in wide-field time-correlated single photon counting microscopy obtained from the photon event phosphor decay. *New Journal of Physics*, *17*. https://doi.org/10.1088/1367-2630/17/2/023032

Hirvonen, L. M. & Suhling, K. (2017). Wide-field TCSPC: Methods and applications. *Measurement Science and Technology*, *28*(1). https://doi.org/10.1088/1361-6501/28/1/012003

Hoffman, W. E., Charbel, F. T. & Edelman, G. (1996). Brain tissue oxygen, carbon dioxide, and pH in neurosurgical patients at risk for ischemia. *Anesthesia & Analgesia*, *82*(3), 582–586.

Hogan, M. C. (1999). Phosphorescence quenching method for measurement of intracellular PO2 in isolated skeletal muscle fibers. *Journal of Applied Physiology*, *86*(2), 720–724.

Holland, J. P., Lewis, J. S. & Dehdashti, F. (2009). Assessing tumor hypoxia by positron emission tomography with Cu-ATSM. *The Quarterly Journal of Nuclear Medicine and Molecular Imaging : Official Publication of the Italian Association of Nuclear Medicine (AIMN) [and] the International Association of Radiopharmacology (IAR), [and] Section of the Society Of...*, *53*(2), 193–200.

Hosny, N. A., Lee, D. A. & Knight, M. M. (2012). Single photon counting fluorescence lifetime detection of pericellular oxygen concentrations. *Journal of Biomedical Optics*, *17*(1), 016007. https://doi.org/10.1117/1.jbo.17.1.016007

Hutter, L. H., Müller, B. J., Koren, K., Borisov, S. M. & Klimant, I. (2014). Robust optical oxygen sensors based on polymer-bound NIR-emitting platinum(II)-benzoporphyrins. *Journal of Materials Chemistry C*, *2*(36), 7589–7598. https://doi.org/10.1039/c4tc00983e

Huynh, L., Wang, Z., Yang, J., Stoeva, V., Lough, A., Manners, I. & Winnik, M. A. (2005). Evaluation of phosphorescent rhenium and iridium complexes in polythionylphosphazene films for oxygen sensor applications. *Chemistry of Materials*, *17*(19), 4765–4773.

Hynes, J., Marroquin, L. D., Ogurtsov, V. I., Christiansen, K. N., Stevens, G. J.,

Papkovsky, D. B. & Will, Y. (2006). Investigation of drug-induced mitochondrial toxicity using fluorescence-based oxygen-sensitive probes. *Toxicological Sciences*, *92*(1), 186–200.

Ianzano, C., Svihra, P., Flament, M., Hardy, A., Cui, G., Nomerotski, A. & Figueroa, E. (2018). *Spatial characterization of photonic polarization entanglement using a Tpx3Cam intensified fast-camera*. 1–22. http://arxiv.org/abs/1808.06720

Itoh, T., Yaegashi, K., Kosaka, T., Kinoshita, T. & Morimoto, T. (1994). In vivo visualization of oxygen transport in microvascular network. *American Journal of Physiology-Heart and Circulatory Physiology*, *267*(5), H2068–H2078.

Jenkins, J., Dmitriev, R. I. & Papkovsky, D. B. (2015). Imaging cell and tissue O 2 by TCSPC-PLIM. In *Advanced Time-Correlated Single Photon Counting Applications* (pp. 225–247). Springer.

Jeong, W., Rapisarda, A., Park, S. R., Kinders, R. J., Chen, A., Melillo, G., Turkbey, B., Steinberg, S. M., Choyke, P. & Doroshow, J. H. (2014). Pilot trial of EZN-2968, an antisense oligonucleotide inhibitor of hypoxia-inducible factor-1 alpha (HIF-1α), in patients with refractory solid tumors. *Cancer Chemotherapy and Pharmacology*, *73*(2), 343–348.

Jöbsis, F. F. (1977). Noninvasive, infrared monitoring of cerebral and myocardial oxygen sufficiency and circulatory parameters. *Science*, *198*(4323), 1264–1267.

Jokic, T., Borisov, S. M., Saf, R., Nielsen, D. A., Kühl, M. & Klimant, I. (2012). Highly photostable near-infrared fluorescent pH indicators and sensors based on BF2-chelated tetraarylazadipyrromethene dyes. *Analytical Chemistry*, *84*(15), 6723–6730. https://doi.org/10.1021/ac3011796

Kalinina, S., Schaefer, P., Breymayer, J., Bisinger, D., Chakrabortty, S. & Rueck, A. (2018). Oxygen sensing PLIM together with FLIM of intrinsic cellular fluorophores for metabolic mapping. *Imaging, Manipulation, and Analysis of Biomolecules, Cells, and Tissues XVI*, *10497*, 104970F.

Kautsky, H. (1939). Quenching of luminescence by oxygen. *Transactions of the Faraday Society*, *35*(0), 216–219. https://doi.org/10.1039/TF9393500216

Kellner, K., Liebsch, G., Klimant, I., Wolfbeis, O. S., Blunk, T., Schulz, M. B. &

Göpferich, A. (2002). Determination of oxygen gradients in engineered tissue using a fluorescent sensor. *Biotechnology and Bioengineering*, *80*(1), 73–83.

Kelly, C. A., Cruz-Romero, M., Kerry, J. P. & Papkovsky, D. B. (2018a). Assessment of performance of the industrial process of bulk vacuum packaging of raw meat with nondestructive optical oxygen sensing systems. *Sensors (Switzerland)*, *18*(5). https://doi.org/10.3390/s18051395

Kelly, C. A., Cruz-Romero, M., Kerry, J. & Papkovsky, D. B. (2018b). Stability and Safety Assessment of Phosphorescent Oxygen Sensors for Use in Food Packaging Applications. *Chemosensors*, *6*(3), 38. https://doi.org/10.3390/chemosensors6030038

Kelly, C. A., Toncelli, C., Kerry, J. P. & Papkovsky, D. B. (2014). Discrete O_2 sensors produced by a spotting method on polyolefin fabric substrates. *Sensors and Actuators B: Chemical*, *203*, 935–940.

Kelly, C. A., Yusufu, D., Okkelman, I., Banerjee, S., Kerry, J. P., Mills, A. & Papkovsky, D. B. (2020). Extruded phosphorescence based oxygen sensors for large-scale packaging applications. *Sensors and Actuators, B: Chemical*, *304*(September 2019), 127357. https://doi.org/10.1016/j.snb.2019.127357

Klare, J. P. (2012). Biomedical applications of electron paramagnetic resonance (EPR) spectroscopy. *Biomedical Spectroscopy and Imaging*, *1*(2), 101–124. https://doi.org/10.3233/BSI-2012-0010

Kneas, K. A., Demas, J. N., DeGraff, B. A. & Periasamy, A. (2000). Fluorescence microscopy study of heterogeneity in polymer-supported luminescence-based oxygen sensors. *Microscopy and Microanalysis*, *6*(6), 551–561.

Koch, C. J. & Evans, S. M. (2003). Non-invasive pet and spect imaging of tissue hypoxia using isotopically labeled 2-nitroimidazoles. *Advances in Experimental Medicine and Biology*, *510*(215), 285–292. https://doi.org/10.1007/978-1-4615-0205-0_47

Kondrashina, A. V, Dmitriev, R. I., Borisov, S. M., Klimant, I., O'Brien, I., Nolan, Y. M., Zhdanov, A. V & Papkovsky, D. B. (2012). A Phosphorescent Nanoparticle-Based Probe for Sensing and Imaging of (Intra)Cellular Oxygen

in Multiple Detection Modalities. *Adv. Funct. Mater.*, *22*(23), 4931–4939. https://doi.org/10.1002/adfm.201201387

König, K. (2000). Multiphoton microscopy in life sciences. *Journal of Microscopy*, *200*(2), 83–104.

König, K., So, P. T. C., Mantulin, W. W., Tromberg, B. J. & Gratton, E. (1996). Two-photon excited lifetime imaging of autofluorescence in cells during UV A and NIR photostress. *Journal of Microscopy*, *183*(3), 197–204.

Koo Lee, Y.-E., Ulbrich, E. E., Kim, G., Hah, H., Strollo, C., Fan, W., Gurjar, R., Koo, S. & Kopelman, R. (2010). Near infrared luminescent oxygen nanosensors with nanoparticle matrix tailored sensitivity. *Analytical Chemistry*, *82*(20), 8446–8455.

Koo, Y.-E. L., Cao, Y., Kopelman, R., Koo, S. M., Brasuel, M. & Philbert, M. A. (2004). Real-time measurements of dissolved oxygen inside live cells by organically modified silicate fluorescent nanosensors. *Analytical Chemistry*, *76*(9), 2498–2505.

Korczyński, J. & Włodarczyk, J. (2009). Fluorescence lifetime imaging microscopy (FLIM) in biological and medical research. *Postepy Biochemii*, *55*(4), 434–440.

Koršič, M., Jugović, D. & Kremžar, B. (2006). Intracranial pressure and biochemical indicators of brain damage: follow-up study. *Croatian Medical Journal*, *47*(2), 246–252.

Kuncova, G. & Fialova, M. (1995). Optical oxygen sensor based on metallo-organic compound immobilized by sol-gel technique. *Biotechnology Techniques*, *9*, 175–178.

Lakowicz, J. R. (2006). Principles of fluorescence spectroscopy. In *Principles of Fluorescence Spectroscopy*. https://doi.org/10.1007/978-0-387-46312-4

Lakowicz, J. R., Szmacinski, H., Nowaczyk, K., Berndt, K. W. & Johnson, M. (1992). Fluorescence lifetime imaging. *Analytical Biochemistry*, *202*(2), 316–330. https://doi.org/10.1016/0003-2697(92)90112-k

Lakowicz, J. R., Szmacinski, H., Nowaczyk, K. & Johnson, M. L. (1992). Fluorescence lifetime imaging of calcium using Quin-2. *Cell Calcium*, *13*(3),

131–147.

Lakowicz, J. R., Terpetschnig, E., Murtaza, Z. & Szmacinski, H. (1997). Development of long-lifetime metal-ligand probes for biophysics and cellular imaging. *Journal of Fluorescence*, *7*, 17–25.

Le, Q.-T., Chen, E., Salim, A., Cao, H., Kong, C. S., Whyte, R., Donington, J., Cannon, W., Wakelee, H. & Tibshirani, R. (2006). An evaluation of tumor oxygenation and gene expression in patients with early stage non–small cell lung cancers. *Clinical Cancer Research*, *12*(5), 1507–1514.

Leary, T. S., Klinck, J. R., Hayman, G., Friend, P., Jamieson, N. V & Gupta, A. K. (2002). Measurement of liver tissue oxygenation after orthotopic liver transplantation using a multiparameter sensor: A pilot study. *Anaesthesia*, *57*(11), 1128–1133.

Lebedev, A. Y., Cheprakov, A. V, Sakadzic, S., Boas, D. A., Wilson, D. F. & Vinogradov, S. A. (2009). Dendritic phosphorescent probes for oxygen imaging in biological systems. *ACS Applied Materials & Interfaces*, *1*(6), 1292–1304.

Lecoq, J., Parpaleix, A., Roussakis, E., Ducros, M., Houssen, Y. G., Vinogradov, S. A. & Charpak, S. (2011). Simultaneous two-photon imaging of oxygen and blood flow in deep cerebral vessels. *Nature Medicine*, *17*(7), 893–898. https://doi.org/10.1038/nm.2394

Lee, J. W., Bae, S.-H., Jeong, J.-W., Kim, S.-H. S.-H. K. & Kim, K.-W. (2004). Hypoxia-inducible factor (HIF-1)α: its protein stability and biological functions. *Experimental and Molecular Medicine*, *36*(1), 1–12. https://www.nature.com/articles/emm20041

Lee, J. W., Ko, J., Ju, C. & Eltzschig, H. K. (2019). Hypoxia signaling in human diseases and therapeutic targets. *Experimental & Molecular Medicine*, *51*(6), 1–13.

Lee, S. K. & Okura, I. (1997). Photostable optical oxygen sensing material: platinum tetrakis (pentafluorophenyl) porphyrin immobilized in polystyrene. *Analytical Communications*, *34*(6), 185–188.

Lesher-Pérez, S. C., Kim, G. A., Kuo, C. H., Leung, B. M., Mong, S., Kojima, T.,

Moraes, C., Thouless, M. D., Luker, G. D. & Takayama, S. (2017). Dispersible oxygen microsensors map oxygen gradients in three-dimensional cell cultures. *Biomaterials Science*, *5*(10), 2106–2113. https://doi.org/10.1039/c7bm00119c

Li, L.-P., Halter, S. & Prasad, P. V. (2008). Blood oxygen level-dependent MR imaging of the kidneys. *Magnetic Resonance Imaging Clinics of North America*, *16*(4), 613–625, viii. https://doi.org/10.1016/j.mric.2008.07.008

Liakath-Ali, K., Vancollie, V. E., Heath, E., Smedley, D. P., Estabel, J., Sunter, D., DiTommaso, T., White, J. K., Ramirez-Solis, R. & Smyth, I. (2014). Novel skin phenotypes revealed by a genome-wide mouse reverse genetic screen. *Nature Communications*, *5*(1), 1–13.

Liao, C. & Zhang, Q. (2020). Understanding the oxygen-sensing pathway and its therapeutic implications in diseases. *The American Journal of Pathology*, *190*(8), 1584–1595.

Liebsch, G., Klimant, I., Frank, B., Holst, G. & Wolfbeis, O. S. (2000). Luminescence lifetime imaging of oxygen, pH, and carbon dioxide distribution using optical sensors. *Applied Spectroscopy*, *54*(4), 548–559.

Liebsch, G., Klimant, I. & Wolfbeis, O. S. (1999). Luminescence Lifetime Temperature Sensing Based on Sol-Gels and Poly (acrylonitrile) s Dyed with Ruthenium Metal–Ligand Complexes. *Advanced Materials*, *11*(15), 1296–1299.

Lin, F. K., Suggs, S., Lin, C.-H., Browne, J. K., Smalling, R., Egrie, J. C., Chen, K. K., Fox, G. M., Martin, F. & Stabinsky, Z. (1985). Cloning and expression of the human erythropoietin gene. *Proceedings of the National Academy of Sciences*, *82*(22), 7580–7584.

Lin, H. J., Herman, P. & Lakowicz, J. R. (2003). Fluorescence lifetime-resolved pH imaging of living cells. *Cytometry*, *52A*(2), 77–89. https://doi.org/10.1002/cyto.a.10028

Lin, Z., Cherng-Wen, T., Roy, P. & Trau, D. (2009). In-situ measurement of cellular microenvironments in a microfluidic device. *Lab on a Chip*, *9*(2), 257–262.

Llopart, X., Alozy, J., Ballabriga, R., Campbell, M., Casanova, R., Gromov, V., Heijne, E. H. M., Poikela, T., Santin, E. & Sriskaran, V. (2022). Timepix4, a

large area pixel detector readout chip which can be tiled on 4 sides providing sub-200 ps timestamp binning. *Journal of Instrumentation*, *17*(01), C01044.

Llopart, X., Ballabriga, R., Campbell, M., Tlustos, L. & Wong, W. (2008). Erratum to “Timepix, a 65 k programmable pixel readout chip for arrival time, energy and/or photon counting measurements” [Nucl. Instr. and Meth. A. 581 (2007) 485-494] (DOI:10.1016/j.nima.2007.08.079). *Nuclear Instruments and Methods in Physics Research, Section A: Accelerators, Spectrometers, Detectors and Associated Equipment*, *585*(1–2), 106–108. https://doi.org/10.1016/j.nima.2007.11.003

Longhi, E. & De Cola, L. (2017). Iridium (III) complexes for OLED application. *Iridium (III) in Optoelectronic and Photonics Applications*, 205–274.

Losko, A. S., Han, Y., Schillinger, B., Tartaglione, A., Morgano, M., Strobl, M., Long, J., Tremsin, A. S. & Schulz, M. (2021). New perspectives for neutron imaging through advanced event-mode data acquisition. *Scientific Reports*, *11*(1), 1–11.

Lu, H., MacK, J., Yang, Y. & Shen, Z. (2014). Structural modification strategies for the rational design of red/NIR region BODIPYs. *Chemical Society Reviews*, *43*(13), 4778–4823. https://doi.org/10.1039/c4cs00030g

Mallard, J. R. & Kent, M. (1969). Electron spin resonance in biological tissues. *Physics in Medicine and Biology*, *14*(3), 373–396. https://doi.org/10.1088/0031-9155/14/3/201

Marcu, L. (2012). Fluorescence lifetime techniques in medical applications. *Annals of Biomedical Engineering*, *40*(2), 304–331.

Mason, R. P., Antich, P. P., Babcock, E. E., Constantinescu, A., Peschke, P. & Hahn, E. W. (1994). Non-invasive determination of tumor oxygen tension and local variation with growth. *International Journal of Radiation Oncology, Biology, Physics*, *29*(1), 95–103. https://doi.org/10.1016/0360-3016(94)90231-3

Maxwell, P. H., Pugh, C. W. & Ratcliffe, P. J. (1993). Inducible operation of the erythropoietin 3’enhancer in multiple cell lines: evidence for a widespread oxygen-sensing mechanism. *Proceedings of the National Academy of Sciences*,

90(6), 2423–2427.

McEvoy, A. K., McDonagh, C. & MacCraith, B. D. (1997). Optimisation of sol-gel-derived silica films for optical oxygen sensing. *Journal of Sol-Gel Science and Technology*, *8*, 1121–1125.

Meixensberger, J., Dings, J., Kuhnigk, H. & Roosen, K. (1993). Studies of tissue PO 2 in normal and pathological human brain cortex. In *Monitoring of cerebral blood flow and metabolism in intensive care* (pp. 58–63). Springer.

Mikulec, B. (2000). *Single photon detection with semiconductor pixel arrays for medical imaging applications (Doctoral dissertation)*. Vienna U.

Mikulec, B., Campbell, M., Dipasquale, G., Schwarz, C. & Watt, J. (2001). Characterisation of a single photon counting pixel system for imaging of low-contrast objects. *Nuclear Instruments and Methods in Physics Research Section A: Accelerators, Spectrometers, Detectors and Associated Equipment*, *458*(1–2), 352–359.

Miyake, T., Kung, C. K. & Goldwasser, E. (1977). Purification of human erythropoietin. *Journal of Biological Chemistry*, *252*(15), 5558–5564.

Mizukami, K., Katano, A., Shiozaki, S., Yoshihara, T., Goda, N. & Tobita, S. (2020). In vivo O_2 imaging in hepatic tissues by phosphorescence lifetime imaging microscopy using Ir (III) complexes as intracellular probes. *Scientific Reports*, *10*(1), 1–14.

Mizukoshi, K., Hamanaka, Y. & Niwayama, M. (2022). Investigation of oxygen saturation in regions of skin by near infrared spectroscopy. *Skin Research and Technology*, *28*(5), 695–702.

MOCON. (n.d.). Available Online. https://www.mocon.com/instruments/optech-o2-model-p.html

Molter, T. W., McQuaide, S. C., Suchorolski, M. T., Strovas, T. J., Burgess, L. W., Meldrum, D. R. & Lidstrom, M. E. (2009). A microwell array device capable of measuring single-cell oxygen consumption rates. *Sensors and Actuators B: Chemical*, *135*(2), 678–686.

Muller, M., Padberg, W., Schindler, E., Sticher, J., Osmer, C., Friemann, S. &

Hempelmann, G. (1998). Renocortical tissue oxygen pressure measurements in patients undergoing living donor kidney transplantation. *Anesthesia & Analgesia*, *87*(2), 474–476.

Müller, M., Schindler, E., Roth, S., Schürholz, A., Vollerthun, M. & Hempelmann, G. (2002). Effects of desflurane and isoflurane on intestinal tissue oxygen pressure during colorectal surgery. *Anaesthesia*, *57*(2), 110–115.

Müller, M., Schück, R., Erkens, U., Sticher, J., Haase, C. & Hempelmann, G. (1995). Effects of lumbar peridural anesthesia on tissue pO2 of the large intestine in man. *Anasthesiologie, Intensivmedizin, Notfallmedizin, Schmerztherapie: AINS*, *30*(2), 108–110.

Murkin, J. M. & Arango, M. (2009). Near-infrared spectroscopy as an index of brain and tissue oxygenation. *British Journal of Anaesthesia*, *103*(suppl_1), i3–i13.

Neugebauer, U., Pellegrin, Y., Devocelle, M., Forster, R. J., Signac, W., Moran, N. & Keyes, T. E. (2008). Ruthenium polypyridyl peptide conjugates: membrane permeable probes for cellular imaging. *Chemical Communications*, *42*, 5307–5309.

Nielsen, T., Wittenborn, T. & Horsman, M. R. (2012). Dynamic Contrast-Enhanced Magnetic Resonance Imaging (DCE-MRI) in Preclinical Studies of Antivascular Treatments. *Pharmaceutics*, *4*(4), 563–589. https://doi.org/10.3390/pharmaceutics4040563

Nomerotski, A. (2019). Imaging and time stamping of photons with nanosecond resolution in Timepix based optical cameras. *Nuclear Instruments and Methods in Physics Research, Section A: Accelerators, Spectrometers, Detectors and Associated Equipment*, *937*(May), 26–30. https://doi.org/10.1016/j.nima.2019.05.034

Nomerotski, A., Chakaberia, I., Fisher-Levine, M., Janoska, Z., Takacs, P. & Tsang, T. (2017). Characterization of TimepixCam, a fast imager for the time-stamping of optical photons. *Journal of Instrumentation*, *12*(1). https://doi.org/10.1088/1748-0221/12/01/C01017

Nomerotski, A., Chekhlov, M., Dolzhenko, D., Glazenborg, R., Farella, B., Keach,

M., Mahon, R., Orlov, D. & Svihra, P. (2023). Intensified Tpx3Cam, a fast data-driven optical camera with nanosecond timing resolution for single photon detection in quantum applications. *Journal of Instrumentation*, *18*(01), C01023. https://doi.org/10.1088/1748-0221/18/01/c01023

O. Stern and M. Volmer. (1919). über die Abklingzeit der Fluoreszenz. *Zeitschrift Für Physik, 20*, 183–188.

O'Donovan, C., Hynes, J., Yashunski, D. & Papkovsky, D. B. (2005). Phosphorescent oxygen-sensitive materials for biological applications. *Journal of Materials Chemistry*, *15*(27–28), 2946–2951. https://doi.org/10.1039/b501748c

O'Hara, J. A., Khan, N., Hou, H., Wilmot, C. M., Demidenko, E., Dunn, J. F. & Swartz, H. M. (2004). Comparison of EPR oximetry and Eppendorf polarographic electrode assessments of rat brain PtO_2. *Physiological Measurement*, *25*(6), 1413.

O'Riordan, T. C., Zhdanov, A. V, Ponomarev, G. V & Papkovsky, D. B. (2007). Analysis of intracellular oxygen and metabolic responses of mammalian cells by time-resolved fluorometry. *Analytical Chemistry*, *79*(24), 9414–9419.

Ogawa, S., Lee, T.-M., Kay, A. R. & Tank, D. W. (1990). Brain magnetic resonance imaging with contrast dependent on blood oxygenation. *Proceedings of the National Academy of Sciences*, *87*(24), 9868–9872.

Okkelman, I. A., Dmitriev, R. I., Foley, T. & Papkovsky, D. B. (2016). Use of fluorescence lifetime imaging microscopy (FLIM) as a timer of cell cycle S phase. *PLoS ONE*, *11*(12), 1–18. https://doi.org/10.1371/journal.pone.0167385

Orte, A., Alvarez-Pez, J. M. & Ruedas-Rama, M. J. (2013). Fluorescence lifetime imaging microscopy for the detection of intracellular pH with quantum dot nanosensors. *ACS Nano*, *7*(7), 6387–6395. https://doi.org/10.1021/nn402581q

Papkovsky, D. B. (1995). New oxygen sensors and their application to biosensing. *Sensors and Actuators B: Chemical*, *29*(1–3), 213–218.

Papkovsky, D. B. (2004). Methods in optical oxygen sensing: protocols and critical analyses. In *Methods in enzymology* (Vol. 381, pp. 715–735). Elsevier.

Papkovsky, D. B. & Dmitriev, R. I. (2013). Biological detection by optical oxygen sensing. *Chem. Soc. Rev.*, *42*(22), 8700–8732. https://doi.org/10.1039/C3CS60131E

Papkovsky, D. B. & Dmitriev, R. I. (2018). Imaging of oxygen and hypoxia in cell and tissue samples. *Cellular and Molecular Life Sciences*, *75*(16), 2963–2980.

Papkovsky, D. B. & O'Riordan, T. C. (2005). Emerging applications of phosphorescent metalloporphyrins. *Journal of Fluorescence*, *15*, 569–584.

Papkovsky, D. B., Ponomarev, G. V., Trettnak, W. & O'Leary, P. (1995). Phosphorescent Complexes of Porphyrin Ketones: Optical Properties and Application to Oxygen Sensing. *Analytical Chemistry*, *67*(22), 4112–4117. https://doi.org/10.1021/ac00118a013

Papkovsky, D. B., Smiddy, M. A., Papkovskaia, N. Y. & Kerry, J. P. (2002). Nondestructive measurement of oxygen in modified atmosphere packaged hams using a phase-fluorimetric sensor system. *Journal of Food Science*, *67*(8), 3164–3169. https://doi.org/10.1111/j.1365-2621.2002.tb08877.x

Papkovsky, D. B., Zhdanov, A. V, Fercher, A., Dmitriev, R. I. & Hynes, J. (2012). *Phosphorescent oxygen-sensitive probes*. Springer Science & Business Media.

Park, E. J., Reid, K. R., Tang, W., Kennedy, R. T. & Kopelman, R. (2005). Ratiometric fiber optic sensors for the detection of inter-and intra-cellular dissolved oxygen. *Journal of Materials Chemistry*, *15*(27–28), 2913–2919.

Petrášek, Z. & Suhling, K. (2010). Photon arrival timing with sub-camera exposure time resolution in wide-field time-resolved photon counting imaging. *Optics Express*, *18*(24), 24888. https://doi.org/10.1364/oe.18.024888

Phillips, D. & Christensen, R. L. (1985). Time Correlated Single-Photon Counting (Tcspc) Using Laser Excitation. *Instrumentation Science & Technology*, *14*(3–4), 267–292. https://doi.org/10.1080/10739148508543581

Photonis Cricket: (n.d.). https://www.photonis.com/products/cricket

Pircalabioru, G., Aviello, G., Kubica, M., Zhdanov, A. V, Paclet, M.-H., Brennan, L., Hertzberger, R., Papkovsky, D. B., Bourke, B. & Knaus, U. G. (2016). Defensive mutualism rescues NADPH oxidase inactivation in gut infection.

Cell Host & Microbe, *19*(5), 651–663.

Poikela, T., Plosila, J., Westerlund, T., Campbell, M., Gaspari, M. De, Llopart, X., Gromov, V., Kluit, R., Beuzekom, M. Van, Zappon, F., Zivkovic, V., Brezina, C., Desch, K., Fu, Y. & Kruth, A. (2014). Timepix3: A 65K channel hybrid pixel readout chip with simultaneous ToA/ToT and sparse readout. *Journal of Instrumentation*, *9*(5). https://doi.org/10.1088/1748-0221/9/05/C05013

Prabhakar, N. R. (2020). 2019 nobel prize in physiology or medicine. *Physiology*, *35*(2), 81–83.

Press, E., Alaga, K. C., Barr, K., Shao, Q., Bosen, F., Willecke, K. & Laird, D. W. (2017). Disease-linked connexin26 S17F promotes volar skin abnormalities and mild wound healing defects in mice. *Cell Death & Disease*, *8*(6), e2845–e2845.

Procz, S., Avila, C. A., Fey, J., Roque, G. A., Schuetz, M. & Hamann, E. (2019). X-ray and gamma imaging with Medipix and Timepix detectors in medical research. *Radiation Measurements*. https://doi.org/10.1016/j.radmeas.2019.04.007

Pyroscience. (n.d.). https://www.pyroscience.com/contactless-fiber-optic-oxygen-sensor-spots.html

Quaranta, M., Borisov, S. M. & Klimant, I. (2012). Indicators for optical oxygen sensors. *Bioanalytical Reviews*, *4*, 115–157.

Ratcliffe, P. J. (2013). Oxygen sensing and hypoxia signalling pathways in animals: the implications of physiology for cancer. *The Journal of Physiology*, *591*(8), 2027–2042.

Richardson, R. S., Duteil, S., Wary, C., Wray, D. W., Hoff, J. & Carlier, P. G. (2006). Human skeletal muscle intracellular oxygenation: the impact of ambient oxygen availability. *The Journal of Physiology*, *571*(2), 415–424.

Roberts, A., Svihra, P., Al-Refaie, A., Graafsma, H., Küpper, J., Majumdar, K., Mavrokoridis, K., Nomerotski, A., Pennicard, D. & Philippou, B. (2019). First demonstration of 3D optical readout of a TPC using a single photon sensitive Timepix3 based camera. *Journal of Instrumentation*, *14*(06), P06001.

Rumsey, W. L., Pawlowski, M., Lejavardi, N. & Wilson, D. F. (1994). Oxygen

pressure distribution in the heart in vivo and evaluation of the ischemic “border zone”. *The American Journal of Physiology*, *266*(4 Pt 2), H1676-80. https://doi.org/10.1152/ajpheart.1994.266.4.H1676

Rumsey, W. L., Vanderkooi, J. M. & Wilson, D. F. (1988). Imaging of phosphorescence: a novel method for measuring oxygen distribution in perfused tissue. *Science*, *241*(4873), 1649–1651.

Sakadzić, S., Roussakis, E., Yaseen, M. A., Mandeville, E. T., Srinivasan, V. J., Arai, K., Ruvinskaya, S., Devor, A., Lo, E. H., Vinogradov, S. A. & Boas, D. A. (2010). Two-photon high-resolution measurement of partial pressure of oxygen in cerebral vasculature and tissue. *Nature Methods*, *7*(9), 755–759. https://doi.org/10.1038/nmeth.1490

Sakadžić, S., Yuan, S., Dilekoz, E., Ruvinskaya, S., Shalinsky, M. H., Vinogradov, S. A., Ayata, C. & Boas, D. A. (2008). Simultaneous imaging of cerebral blood flow and partial pressure of oxygen during cortical spreading depression. *Biomedical Optics, BIOMED 2008*, *48*(10). https://doi.org/10.1364/biomed.2008.bwc4

Salikhov, K. M. & Zavoiskaya, N. E. (2015). Zavoisky and the discovery of EPR. *Resonance*, *20*(11), 963–968. https://doi.org/10.1007/s12045-015-0264-6

Sanklecha, M. (1993). The pulse oximeter. *The Indian Journal of Pediatrics*, *60*(3), 469–470. https://doi.org/10.1007/BF02751220

Schäferling, M. (2012). The art of fluorescence imaging with chemical sensors. *Angewandte Chemie International Edition*, *51*(15), 3532–3554.

Scheuermann, T. H., Li, Q., Ma, H.-W., Key, J., Zhang, L., Chen, R., Garcia, J. A., Naidoo, J., Longgood, J. & Frantz, D. E. (2013). Allosteric inhibition of hypoxia inducible factor-2 with small molecules. *Nature Chemical Biology*, *9*(4), 271–276.

Schneider, C. A., Rasband, W. S. & Eliceiri, K. W. (2012). NIH Image to ImageJ: 25 years of image analysis. *Nature Methods*, *9*(7), 671–675.

Seidenari, S., Arginelli, F., Bassoli, S., Cautela, J., French, P. M. W., Guanti, M., Guardoli, D., König, K., Talbot, C. & Dunsby, C. (2012). Multiphoton laser

microscopy and fluorescence lifetime imaging for the evaluation of the skin. *Dermatology Research and Practice*, *2012*, 1–9. https://doi.org/10.1155/2012/810749

Semenza, G. L. (2007). Life with oxygen. *Science*, *318*(5847), 62–64.

Semenza, G. L. (2010). Oxygen homeostasis. *Wiley Interdisciplinary Reviews: Systems Biology and Medicine*, *2*(3), 336–361. https://doi.org/10.1002/wsbm.69

Semenza, G. L. (2011). Hypoxia. Cross talk between oxygen sensing and the cell cycle machinery. *American Journal of Physiology-Cell Physiology*, *301*(3), C550–C552.

Semenza, G. L. (2012). Hypoxia-inducible factors in physiology and medicine. *Cell*, *148*(3), 399–408.

Semenza, G. L., Nejfelt, M. K., Chi, S. M. & Antonarakis, S. E. (1991). Hypoxia-inducible nuclear factors bind to an enhancer element located 3'to the human erythropoietin gene. *Proceedings of the National Academy of Sciences*, *88*(13), 5680–5684.

Sen, R., Hirvonen, L. M., Zhdanov, A. V, Svihra, P., Andersson-Engels, S., Nomerotski, A. & Papkovsky, D. B. (2020). New luminescence lifetime macro-imager based on a Tpx3Cam optical camera. *Biomed Opt Express*, *11*(1), 77–88. https://doi.org/10.1364/BOE.11.000077

Sen, R., Li, L., Zhdanov, A. V, Gaspar, R. D. L. & Papkovsky, D. B. (2022). Phosphorescence lifetime measurements with sensor materials: Comparison of the four different detection platforms. *Sensors and Actuators B: Chemical*, *371*(June), 132496. https://doi.org/10.1016/j.snb.2022.132496

Sen, R., Zhdanov, A. V, Bastiaanssen, T. F. S., Hirvonen, L. M., Svihra, P., Fitzgerald, P., Cryan, J. F., Andersson-Engels, S., Nomerotski, A. & Papkovsky, D. B. (2020). Mapping O_2 concentration in ex-vivo tissue samples on a fast PLIM macro-imager. *Scientific Reports*, *10*(1). https://doi.org/10.1038/s41598-020-75928-3

Sen, R., Zhdanov, A. V, Hirvonen, L. M., Svihra, P., Andersson-Engels, S., Nomerotski, A. & Papkovsky, D. B. (2020a). A new macro-imager based on

Tpx3Cam optical camera for PLIM applications. *Biomedical Spectroscopy, Microscopy, and Imaging (SPIE)*, *11359*(April), 60. https://doi.org/10.1117/12.2555387

Sen, R., Zhdanov, A. V, Hirvonen, L. M., Svihra, P., Andersson-Engels, S., Nomerotski, A. & Papkovsky, D. B. (2020b). Characterization of planar phosphorescence based oxygen sensors on a TCSPC-PLIM macro-imager. *Sensors and Actuators, B: Chemical*, *321*, 128459. https://doi.org/10.1016/j.snb.2020.128459

Sharick, J. T., Jeffery, J. J., Karim, M. R., Walsh, C. M., Esbona, K., Cook, R. S. & Skala, M. C. (2019). Cellular Metabolic Heterogeneity In Vivo Is Recapitulated in Tumor Organoids. *Neoplasia (United States)*, *21*(6), 615–626. https://doi.org/10.1016/j.neo.2019.04.004

Sharman, K. K., Periasamy, A., Ashworth, H. & Demas, J. N. (1999). Error analysis of the rapid lifetime determination method for double-exponential decays and new windowing schemes. *Analytical Chemistry*, *71*(5), 947–952.

Shonat, R. D. & Kight, A. C. (2003). Oxygen tension imaging in the mouse retina. *Annals of Biomedical Engineering*, *31*, 1084–1096.

Shonat, R. D., Wilson, D. F., Riva, C. E. & Pawlowski, M. (1992). Oxygen distribution in the retinal and choroidal vessels of the cat as measured by a new phosphorescence imaging method. *Applied Optics*, *31*(19), 3711–3718.

Smiddy, M., Fitzgerald, M., Kerry, J. P., Papkovsky, D. B., O' Sullivan, C. K. & Guilbault, G. G. (2002). Use of oxygen sensors to non-destructively measure the oxygen content in modified atmosphere and vacuum packed beef: Impact of oxygen content on lipid oxidation. *Meat Science*, *61*(3), 285–290. https://doi.org/10.1016/S0309-1740(01)00194-2

Smith, M. L., Counelis, G. J., Maloney-Wilensky, E., Stiefel, M. F., Donley, K. & LeRoux, P. D. (2007). Brain tissue oxygen tension in clinical brain death: a case series. *Neurological Research*, *29*(7), 755–759.

Sparks, H., Görlitz, F., Kelly, D. J., Warren, S. C., Kellett, P. A., Garcia, E., Dymoke-Bradshaw, A. K. L., Hares, J. D., Neil, M. A. A., Dunsby, C. &

French, P. M. W. (2017). Characterisation of new gated optical image intensifiers for fluorescence lifetime imaging. *Review of Scientific Instruments*, *88*(1). https://doi.org/10.1063/1.4973917

Stacy, M. R., Qiu, M., Papademetris, X., Caracciolo, C. M., Constable, R. T. & Sinusas, A. J. (2016). Application of BOLD Magnetic Resonance Imaging for Evaluating Regional Volumetric Foot Tissue Oxygenation: A Feasibility Study in Healthy Volunteers. *European Journal of Vascular and Endovascular Surgery*, *51*(5), 743–749. https://doi.org/https://doi.org/10.1016/j.ejvs.2016.02.008

Stone, H. B., Brown, J. M., Phillips, T. L. & Sutherland, R. M. (1993). Oxygen in human tumors: correlations between methods of measurement and response to therapy. Summary of a workshop held November 19-20, 1992, at the National Cancer Institute, Bethesda, Maryland. *Radiation Research*, *136*(3), 422–434.

Subczynski, W. K., Lukiewicz, S. & Hyde, J. S. (1986). Murine in vivo L-band ESR spin-label oximetry with a loop-gap resonator. *Magnetic Resonance in Medicine*, *3*(5), 747–754.

Suhling, K., Hirvonen, L. M., Levitt, J. A., Chung, P.-H., Tregidgo, C., Le Marois, A., Rusakov, D. A., Zheng, K., Ameer-Beg, S. & Poland, S. (2015). Fluorescence lifetime imaging (FLIM): Basic concepts and some recent developments. *Medical Photonics*, *27*, 3–40.

Swartz, H. M. (2004). Using EPR to measure a critical but often unmeasured component of oxidative damage: oxygen. *Antioxidants & Redox Signaling*, *6*(3), 677–686. https://doi.org/10.1089/152308604773934440

Taylor, J. S., Tofts, P. S., Port, R., Evelhoch, J. L., Knopp, M., Reddick, W. E., Runge, V. M. & Mayr, N. (1999). MR imaging of tumor microcirculation: promise for the new millennium. *Journal of Magnetic Resonance Imaging : JMRI*, *10*(6), 903–907. https://doi.org/10.1002/(sici)1522-2586(199912)10:6<903::aid-jmri1>3.0.co;2-a

Thermann, M., Jostarndt, L., Eberhard, F., Richter, H. & Sass, W. (1985). Oxygen supply of the human small intestine in mechanical ileus. *Langenbecks Archiv Fur Chirurgie*, *363*(3), 179–184.

Thomas, P. C., Halter, M., Tona, A., Raghavan, S. R., Plant, A. L. & Forry, S. P. (2009). A noninvasive thin film sensor for monitoring oxygen tension during in vitro cell culture. *Analytical Chemistry*, *81*(22), 9239–9246.

Tirotta, I., Dichiarante, V., Pigliacelli, C., Cavallo, G., Terraneo, G., Bombelli, F. B., Metrangolo, P. & Resnati, G. (2015). 19F magnetic resonance imaging (MRI): From design of materials to clinical applications. *Chemical Reviews*, *115*(2), 1106–1129. https://doi.org/10.1021/cr500286d

Toncelli, C., Arzhakova, O. V., Dolgova, A., Volynskii, A. L., Kerry, J. P. & Papkovsky, D. B. (2014). Phosphorescent oxygen sensors produced by spot-crazing of polyphenylenesulfide films. *Journal of Materials Chemistry C*, *2*(38), 8035–8041. https://doi.org/10.1039/c4tc01390e

Tsigaridas, S., Beuzekom, M. V., Graaf, H. V.D., Hartjes, F., Heijhoff, K., Hessey, N. P., de Jong, P. J. & Prodanovic, V. (2019). Timewalk correction for the Timepix3 chip obtained with real particle data. *Nuclear Instruments and Methods in Physics Research, Section A: Accelerators, Spectrometers, Detectors and Associated Equipment*, *930*(April), 185–190. https://doi.org/10.1016/j.nima.2019.03.077

Tsytsarev, V., Akkenti, F., Pumbo, E., Tang, Q., Chen, Y., Erzurumlu, R. S. & Papkovsky, D. B. (2017). Planar implantable sensor for in vivo measurement of cellular oxygen metabolism in brain tissue. *Journal of Neuroscience Methods*, *281*, 1–6. https://doi.org/10.1016/j.jneumeth.2017.02.005

Tsytsarev, V., Arakawa, H., Borisov, S. M., Pumbo, E., Erzurumlu, R. S. & Papkovsky, D. B. (2013). In vivo imaging of brain metabolism activity using a phosphorescent oxygen-sensitive probe. *Journal of Neuroscience Methods*, *216*(2), 146–151. https://doi.org/10.1016/j.jneumeth.2013.04.005

Valledor, M., Campo, J. C., Sánchez-Barragán, I., Costa-Fernández, J. M., Alvarez, J. C. & Sanz-Medel, A. (2006). Determination of phosphorescence lifetimes in the presence of high background signals using phase-shift measurements. *Sensors and Actuators B: Chemical*, *113*(1), 249–258.

Vanderkooi, J. M., Maniara, G., Green, T. J. & Wilson, D. F. (1987). An optical method for measurement of dioxygen concentration based upon quenching of

phosphorescence. *Journal of Biological Chemistry*, *262*(12), 5476–5482.

Vaupel, P., Schlenger, K., Knoop, C. & Höckel, M. (1991). Oxygenation of human tumors: evaluation of tissue oxygen distribution in breast cancers by computerized O_2 tension measurements. *Cancer Research*, *51*(12), 3316–3322.

Veetil, J. V, Jin, S. & Ye, K. (2012). Fluorescence lifetime imaging microscopy of intracellular glucose dynamics. *Journal of Diabetes Science and Technology*, *6*(6), 1276–1285.

Vinogradov, S. A., Lo, L.-W., Jenkins, W. T., Evans, S. M., Koch, C. & Wilson, D. F. (1996). Noninvasive imaging of the distribution in oxygen in tissue in vivo using near-infrared phosphors. *Biophysical Journal*, *70*(4), 1609–1617.

Vinogradov, S. A. & Wilson, D. F. (1995). Metallotetrabenzoporphyrins. New phosphorescent probes for oxygen measurements. *Journal of the Chemical Society, Perkin Transactions 2*, *1*, 103–111.

Visser, J., Beuzekom, M. Van, Boterenbrood, H., Heijden, B. Van Der, Muñoz, J. I., Kulis, S., Munneke, B. & Schreuder, F. (2015). SPIDR: A read-out system for Medipix3 & Timepix3. *Journal of Instrumentation*, *10*(12). https://doi.org/10.1088/1748-0221/10/12/C12028

Wahl, M. (2014). Time-correlated single-photon counting. *PicoQuant GmbH*, 1–14.

Wang, G. L., Jiang, B.-H., Rue, E. A. & Semenza, G. L. (1995). Hypoxia-inducible factor 1 is a basic-helix-loop-helix-PAS heterodimer regulated by cellular O_2 tension. *Proceedings of the National Academy of Sciences*, *92*(12), 5510–5514.

Wang, G. L. & Semenza, G. L. (1993). General involvement of hypoxia-inducible factor 1 in transcriptional response to hypoxia. *Proceedings of the National Academy of Sciences*, *90*(9), 4304–4308.

Wang, X. D., Chen, H., Zhao, Y., Chen, X. & Wang, X. (2010). Optical oxygen sensors move towards colorimetric determination. *TrAC Trends in Analytical Chemistry*, *29*(4), 319–338.

Wang, X. D., Gorris, H. H., Stolwijk, J. A., Meier, R. J., Groegel, D. B. M., Wegener, J. & Wolfbeis, O. S. (2011). Self-referenced RGB colour imaging of intracellular oxygen. *Chemical Science*, *2*(5), 901–906.

Wang, X. D. & Wolfbeis, O. S. (2014). Optical methods for sensing and imaging oxygen: materials, spectroscopies and applications. *Chemical Society Reviews*, *43*(10), 3666–3761. https://doi.org/10.1039/C4CS00039K

Wang, Z., Zheng, Y., Zhao, D., Zhao, Z., Liu, L., Pliss, A., Zhu, F., Liu, J., Qu, J. & Luan, P. (2018). Applications of fluorescence lifetime imaging in clinical medicine. *Journal of Innovative Optical Health Sciences*, *11*(01), 1830001. https://doi.org/10.1142/s179354581830001x

Warburg, O. (1931). The oxygen-transferring ferment of respiration. *Nobel Lecture*, 254–268.

Wei, L., Yan, W. & Ho, D. (2017). Recent advances in fluorescence lifetime analytical microsystems: Contact optics and CMOS time-resolved electronics. *Sensors (Switzerland)*, *17*(12). https://doi.org/10.3390/s17122800

Weiss, G. J., Chao, J., Neidhart, J. D., Ramanathan, R. K., Bassett, D., Neidhart, J. A., Choi, C. H. J., Chow, W., Chung, V. & Forman, S. J. (2013). First-in-human phase 1/2a trial of CRLX101, a cyclodextrin-containing polymer-camptothecin nanopharmaceutical in patients with advanced solid tumor malignancies. *Investigational New Drugs*, *31*(4), 986–1000.

Wilson, D. F. (2008). Quantifying the role of oxygen pressure in tissue function. *American Journal of Physiology - Heart and Circulatory Physiology*, *294*(1), 2007–2009. https://doi.org/10.1152/ajpheart.01293.2007

Wilson, D. F. & Cerniglia, G. J. (1992). Localization of tumors and evaluation of their state of oxygenation by phosphorescence imaging. *Cancer Research*, *52*(14), 3988–3993.

Wilson, D. F., Gomi, S., Pastuszko, A. & Greenberg, J. H. (1993). Microvascular damage in the cortex of cat brain from middle cerebral artery occlusion and reperfusion. *Journal of Applied Physiology*, *74*(2), 580–589.

Wilson, D. F., Pastuszko, A., DiGiacomo, J. E., Pawlowski, M., Schneiderman, R. & Delivoria-Papadopoulos, M. (1991). Effect of hyperventilation on oxygenation of the brain cortex of newborn piglets. *Journal of Applied Physiology*, *70*(6), 2691–2696.

Wilson, D. F., Vanderkooi, J. M., Green, T. J., Maniara, G., DeFeo, S. P. & Bloomgarden, D. C. (1987). A versatile and sensitive method for measuring oxygen. *Oxygen Transport to Tissue IX*, 71–77.

Wilson, D. F., Vinogradov, S. A., Grosul, P., Kuroki, A. & Bennett, J. (2005). Imaging oxygen pressure in the retina of the mouse eye. *Advances in Experimental Medicine and Biology*, *566*, 159–165. https://doi.org/10.1007/0-387-26206-7_22

Wilson, D. F., Vinogradov, S. A., Grosul, P., Vaccarezza, M. N., Kuroki, A. & Bennett, J. (2005). Oxygen distribution and vascular injury in the mouse eye measured by phosphorescence-lifetime imaging. *Applied Optics*, *44*(25), 5239–5248.

Wolfbeis, O. S., Leiner, M. J. P. & Posch, H. E. (1986). A new sensing material for optical oxygen measurement, with the indicator embedded in an aqueous phase. *Microchimica Acta*, *90*, 359–366.

Wu, C., Bull, B., Christensen, K. & McNeill, J. (2009). Ratiometric single-nanoparticle oxygen sensors for biological imaging. *Angewandte Chemie*, *121*(15), 2779–2783.

Zarychta-Wiśniewska, W., Burdzinska, A., Zagozdzon, R., Dybowski, B., Butrym, M., Gajewski, Z. & Paczek, L. (2017). In vivo imaging system for explants analysis—A new approach for assessment of cell transplantation effects in large animal models. *PLoS ONE*, *12*(9), 1–21. https://doi.org/10.1371/journal.pone.0184588

Zhao, A., van Beuzekom, M., Bouwens, B., Byelov, D., Chakaberia, I., Cheng, C., Maddox, E., Nomerotski, A., Svihra, P. & Visser, J. (2017). Coincidence velocity map imaging using Tpx3Cam, a time stamping optical camera with 1.5 ns timing resolution. *Review of Scientific Instruments*, *88*(11), 113104.

Zhdanov, A. V, Dmitriev, R. I. & Papkovsky, D. B. (2012). Bafilomycin A1 activates HIF-dependent signalling in human colon cancer cells via mitochondrial uncoupling. *Biosci Rep*, *32*(6), 587–595. https://doi.org/10.1042/BSR20120085

Zhdanov, A. V, Li, L., Yang, P., Shkirdova, A. O., Tang, S., Yashunsky, D. V, Ponomarev, G. V, Zamilatskov, I. A. & Papkovsky, D. B. (2022). Advanced multi-modal, multi-analyte optochemical sensing platform for cell analysis. *Sensors and Actuators B: Chemical*, *355*, 131116.

Zhdanov, A. V, Okkelman, I. A., Golubeva, A. V., Doerr, B., Hyland, N. P., Melgar, S., Shanahan, F., Cryan, J. F. & Papkovsky, D. B. (2017). Quantitative analysis of mucosal oxygenation using ex vivo imaging of healthy and inflamed mammalian colon tissue. *Cellular and Molecular Life Sciences*, *74*(1), 141–151. https://doi.org/10.1007/s00018-016-2323-x

Zheng, K., Jensen, T. P. & Rusakov, D. A. (2018). Monitoring intracellular nanomolar calcium using fluorescence lifetime imaging. *Nature Protocols*, *13*(3), 581–597. https://doi.org/10.1038/nprot.2017.154

Zhukas, L. A., Millican, M. J., Svihra, P., Nomerotski, A. & Blinov, B. B. (2021). Direct observation of ion micromotion in a linear Paul trap. *Physical Review A*, *103*(2), 23105.

Zhukas, L. A., Svihra, P., Nomerotski, A. & Blinov, B. B. (2021). High-fidelity simultaneous detection of a trapped-ion qubit register. *Physical Review A*, *103*(6), 62614.